

1 **Summertime productivity and carbon export potential in the** 2 **Weddell Sea, with a focus on the waters adjacent to Larsen C** 3 **Ice Shelf**

4
5 Raquel F. Flynn^{1*}, Thomas G. Bornman^{2,3}, Jessica M. Burger¹, Shantelle Smith¹, Kurt A.M.
6 Spence¹ and Sarah E. Fawcett^{1,4}

7
8 ¹Department of Oceanography, University of Cape Town, Cape Town, South Africa

9 ²South African Environmental Observation Network, Elwandle Coastal Node, Port Elizabeth, South Africa

10 ³Institute for Coastal and Marine Research, Nelson Mandela University, Port Elizabeth, South Africa

11 ⁴Marine and Antarctic Research centre for Innovation and Sustainability (MARIS), University of Cape Town,
12 Cape Town, South Africa

13
14 *Correspondence to: Raquel F. Flynn (flyraq001@myuct.ac.za)

15 16 **Abstract**

17 The Weddell Sea represents a point of origin in the Southern Ocean where globally-important water masses form.
18 Biological activities in Weddell Sea surface waters thus affect large-scale ocean biogeochemistry. During
19 January/February 2019, we measured net primary production (NPP), nitrogen (nitrate, ammonium, urea) uptake,
20 and nitrification in the western Weddell Sea at the Antarctic Peninsula (AP) and Larsen C Ice Shelf (LCIS), in the
21 southwestern Weddell Gyre (WG), and at Fimbul Ice Shelf (FIS) in the south-eastern Weddell Sea. The highest
22 average rates of NPP and greatest nutrient drawdown occurred at LCIS. Here, the phytoplankton community was
23 dominated by colonial *Phaeocystis antarctica*, with diatoms increasing in abundance later in the season as sea-ice
24 melted. At the other stations, NPP was variable, and diatoms known to enhance carbon export (e.g., *Thalassiosira*
25 spp.) were dominant. Euphotic zone nitrification was always below detection, such that nitrate uptake could be
26 used as a proxy for carbon export potential, which was highest in absolute terms at LCIS and the AP. Surprisingly,
27 the highest f-ratios occurred near FIS rather than LCIS (average of 0.73 ± 0.09 versus 0.47 ± 0.08). We attribute
28 this unexpected result to partial ammonium inhibition of nitrate uptake at LCIS (where ammonium concentrations
29 were $0.6 \pm 0.4 \mu\text{M}$, versus $0.05 \pm 0.1 \mu\text{M}$ at FIS), with elevated ammonium resulting from increased heterotrophy
30 following the accumulation of nitrate-fuelled phytoplankton biomass in early summer. Across the Weddell Sea,
31 carbon export appears to be controlled by a combination of physical, chemical, and biological factors, with the
32 highest [potential](#) export flux occurring at the ice shelves and lowest in the central WG.

33
34 **Keywords:** Nitrogen uptake, primary production, phytoplankton taxonomy, nutrient depletion, ammonium
35 inhibition, Antarctic ice shelves

39 1. Introduction

40 The Southern Ocean is an important driver of Earth's climate as it transports large quantities of heat and dissolved
41 gases, and supplies 65-85% of the global ocean's nutrients (Keffer and Holloway, 1988; Sarmiento et al., 2004;
42 Frölicher et al., 2015; Keller et al., 2016; Fripiat et al., 2021). Despite the Southern Ocean's central role in
43 atmospheric CO₂ removal (DeVries, 2014; Frölicher et al., 2015; Gruber et al., 2019), the incomplete drawdown
44 of surface-water nutrients (i.e., nitrate, phosphate, and silicic acid) due to iron and light limitation of phytoplankton
45 (Martin et al., 1991; Sunda and Huntsman, 1997) represents a missed opportunity for CO₂ removal (Sarmiento
46 and Toggweiler, 1984). The Weddell Sea constitutes a point of origin in the Southern Ocean where water masses
47 form and communicate with the atmosphere before subducting (Muench and Gordon, 1995; Talley et al., 2011),
48 thereby setting the initial physical and chemical conditions of the deep global ocean. Biogeochemical cycling in
49 the surface Weddell Sea thus has implications for carbon transfer to and storage in the ocean interior (Hoppema
50 et al., 2004; Kerr et al., 2018). The southern and western Weddell Sea are bounded by ice shelves, which promote
51 high rates of summertime phytoplankton productivity, nutrient drawdown and carbon export (El-Sayed and
52 Taguchi, 1981; Hoppema and Goeyens, 1999; Hoppema et al., 2000), largely because the surface ecosystem is
53 less iron- and light-limited in the ice shelf-adjacent waters than in the open Weddell Sea (Klunder et al., 2014).

54
55 The Weddell Sea is separated from the Antarctic Circumpolar Current (ACC) and open Southern Ocean by the
56 Weddell Sea fronts (Orsi et al. 1995). The general large-scale circulation takes the form of the cyclonic, wind-
57 driven and topographically-steered Weddell Gyre (WG) (Fahrbach et al., 1994, 1995; Orsi et al., 1995). ~~that~~
58 ~~transports the relatively warm, saline waters of the ACC into the polar region where they are cooled and become~~
59 ~~more saline.~~ The production of bottom water is thought to occur at two sites in the Weddell Sea: at Filchner-Ronne
60 Ice Shelf (FRIS) and Larsen C Ice Shelf (LCIS) (Gordon et al., 1993; Schröder et al., 2002; Schodlok et al., 2002).
61 Here, Modified Warm Deep Water (MWDW) intrudes onto the continental shelf and mixes with Antarctic Surface
62 Water (ASW), ~~which alters its physical and chemical properties, ultimately resulting in the formation of dense~~
63 ~~bottom waters. ASW is cooled to freezing point through heat loss to the atmosphere, as well as being supercooled~~
64 ~~under the ice shelves, and increases in salinity due to brine rejection during sea ice formation, which further~~
65 ~~increases its density (Brennecke 1921; Mosby 1934; Gill 1973). As MWDW flows throughout the gyre, its~~
66 ~~physical and chemical properties are altered due to mixing with ASW, ultimately resulting in the formation of~~
67 ~~dense bottom waters.~~ Upon reaching the Antarctic Peninsula (AP), the transformed bottom waters either spill out
68 over the shelf and re-enter the ACC or are entrained into the eastward flowing limb of the WG (Orsi et al., 1993;
69 Locarnini et al., 1993).

70
71 ~~The surface waters of the open Weddell Sea~~ Weddell Sea-surface waters are warm and saline while those over the
72 continental shelf are relatively cool and fresh (Nicholls et al., 2004). These different waters are separated by the
73 Antarctic Slope Front (ASF; Jacobs, 1986; 1991), a fast-flowing jet situated between the 500 m and 1000 m
74 isobath that separates the Open Ocean Zone (OOZ) from the Coastal and Continental Shelf Zone (CCSZ; Jacobs,
75 1986; 1991; Muench and Gordon, 1995). The Antarctic CCSZ has been observed to host high rates of productivity
76 in the summer (e.g., Smith and Nelson, 1990; Arrigo et al., 2008) as melting sea-ice supplies dissolved iron and
77 increases water column stratification, yielding favourable conditions for phytoplankton growth (Lannuzel et al.,
78 2008). Inputs of dissolved iron from continental shelf sediments and coastal runoff further elevate the ambient

79 iron concentrations, such that the CCSZ seldom experiences iron-depletion (Klunder et al., 2014; Dinniman et al.,
80 2020). As a result, the large phytoplankton blooms of the CCSZ can at times almost completely deplete the surface
81 nitrate concentrations (Jennings et al. 1984; Hoppema et al. 2000; Henley et al. 2017), supporting high rates of
82 carbon export [that fuel the benthic community on the underlying continental shelf](#) (Isla et al., 2006, 2011; Pineda-
83 Metz et al., 2019) [and/or eventually lead to long-term storage of atmospheric CO₂ in newly-formed AABW](#)
84 (Arrigo et al., 2008). In contrast, the Ooz is far less productive due to persistent iron-deplete conditions, [along](#)
85 [with incidences of light limitation associated with high sea-ice concentrations \(particularly in the central WG\)](#)
86 and/or deep mixed layers (MLD) (Klunder et al., 2011; De Jong et al., 2012). Here, [the co-limitation of](#)
87 [productivity by iron and light typically yields low rates of biological carbon export](#) [surface nutrients are never](#)
88 [fully consumed and carbon export rates are low](#) (Boyd et al., 2008; Boyd and Ellwood, 2010; Klunder et al., 2011;
89 De Jong et al., 2012).

90
91 On an annual basis, phytoplankton growth in the euphotic zone that is fuelled by nitrate supplied from below (i.e.,
92 “new production”) must be balanced by the export of sinking organic matter into the ocean interior (i.e., “export
93 production”), thus driving CO₂ removal (Dugdale and Goering, 1967; Eppley and Peterson, 1979). By contrast,
94 phytoplankton growth supported by nitrogen (N) sources that are recycled within the euphotic zone, such as
95 ammonium and urea (i.e., “regenerated production”), results in no net removal of CO₂ to the deep ocean. The
96 biologically-driven flux of carbon from surface waters, termed the “biological [carbon pump](#)”, transfers CO₂ to the
97 isolated waters of the deep ocean, [regulating maintaining](#) the atmospheric concentration of this greenhouse gas
98 (Volk and Hoffert, 1985). The high nutrient-low chlorophyll state of much of the Southern Ocean represents a
99 “leak” in the ocean’s biological [carbon pump](#) since by consuming mixed-layer nutrients more completely,
100 phytoplankton could theoretically lower atmospheric CO₂ (Sarmiento and Toggweiler, 1984). Indeed, one
101 hypothesis for the [80–100 ppm](#) decrease in atmospheric CO₂ that characterized the ice ages is more complete
102 consumption of surface nutrients (i.e., a more efficient biological [carbon pump](#)) in the open Southern Ocean
103 (Sigman and Boyle, 2000; Sigman et al., 2010; Martínez-García et al., 2014).

104
105 Since phytoplankton in the CCSZ of the Weddell Sea consume much of the nitrate supplied to the surface
106 (Jennings et al. 1984; Hoppema et al. 2000), they should, by mass balance, drive the export of a significant amount
107 of atmospheric CO₂ (“fixed” as biomass) to depth, a significant portion of which will be subducted in newly-
108 formed bottom waters to be sequestered for >1000 years (Ito et al. 2010). Understanding the controls on biological
109 nutrient utilization in the Weddell Sea, particularly in the CCSZ, is thus central to our understanding of its
110 contribution to the Southern Ocean’s role in setting atmospheric CO₂. In general, phytoplankton growth in the
111 Weddell Sea is regulated by the seasonal cycle of sea-ice, with the associated availability of light and iron
112 imposing the main constraints (El-Sayed and Taguchi 1981). In winter, sea-ice formation and wind-driven mixing
113 supply high concentrations of nutrients to ASW (Hoppema et al. 2007; 2015) that remain largely unconsumed due
114 to the deep mixed layers and short days (Cota et al., 1992; Scharek et al., 1994; Spiridonov et al., 1996). Relief
115 from light limitation in spring and early summer following increased water-column stratification due to sea-ice
116 melt combined with enhanced solar radiation leads to the development of phytoplankton blooms. The size and
117 duration of these blooms is ultimately dependent on macro- (e.g., nitrate and silicate) and micronutrient (e.g., iron)

118 availability (Martin et al. 1991; Boyd 2004; Boyd and Ellwood 2010; Llort et al. 2015), [as well as zooplankton](#)
119 [grazing](#) (Smetacek et al., 2004 and references therein; Arteaga et al., 2020).

120
121 Observations suggest that Weddell Sea phytoplankton blooms are initially dominated by smaller species (e.g.,
122 *Phaeocystis antarctica*; 2-6 μm) that are well-adapted to the low-light conditions associated with deep springtime
123 mixed layers (Moisan and Mitchell, 1999; Arrigo et al., 1999). ~~The ability of these smaller cells to rapidly grow~~
124 ~~and consume the available nutrients results in bloom initiation. However, their small size also means that *P.*~~
125 ~~*antarctica* experience high rates of predation by microzooplankton and sink fairly slowly, which decreases their~~
126 ~~carbon export potential and enhances their contribution to the microbial loop (Hansen et al. 1994; 1997).~~ As the
127 season progresses, intensifying upper water-column stratification provides suitable growth conditions for larger
128 phytoplankton such as diatoms (Goffart et al., 2000; Nissen and Vogt, 2021). Diatoms tend to rely heavily on
129 nitrate as their dominant N source [under high light and nutrient conditions, and are generally outcompeted by](#)
130 [smaller phytoplankton for ammonium](#) (Probyn and Painting, 1985; Koike et al., 1986; Lomas and Glibert, 1999;
131 Karsh et al., 2003). Diatoms are also a major vector for carbon export due to their rapid sinking rates facilitated
132 by their generally larger size and biogenic silica ballasting (Tréguer et al., 2017). The seasonal shift in the Weddell
133 Sea community from small, non-silicified phytoplankton to larger, more heavily-silicified species is thus
134 associated with a significant increase in carbon export (Assmy et al. 2013). Concomitantly, sea-ice melt supplies
135 high concentrations of dissolved iron to surface waters (up to 7 nM in the western Weddell Sea; Lannuzel et al.,
136 2008; Klunder et al., 2014), which helps to support nitrate drawdown (Klunder et al., 2011, 2014). Eventually, as
137 surface iron (and occasionally, nitrate; Hoppema, et al. 2000) concentrations again become limiting,
138 phytoplankton rely proportionally more on ammonium and other regenerated N sources that have become
139 increasingly available due to heterotrophic processing of the accumulated (i.e., bloom) biomass (Goeyens et al.,
140 1995; Semeneh et al., 1998). The phytoplankton community consequently shifts once more towards smaller
141 species that are better adapted to low iron conditions and specialize in the consumption of regenerated N,
142 ultimately leading to a decrease in carbon export (Goeyens et al., 1995).

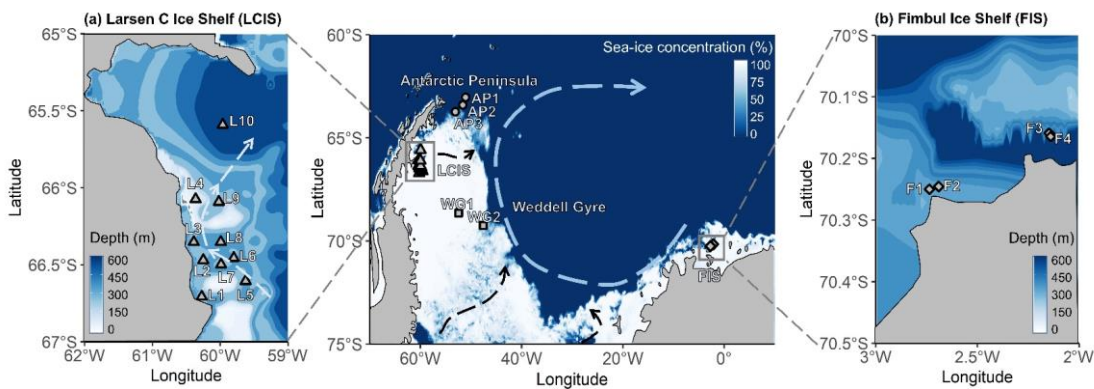
143
144 The Weddell Sea is particularly understudied near LCIS where thick sea-ice conditions persist year-round. To our
145 knowledge, the only biogeochemical study conducted in the vicinity of LCIS was undertaken in the austral
146 summer of 1992/3. Using measurements of nutrient depletion, Hoppema et al. (2000) estimated primary
147 production in the vicinity of LCIS to be 47.5-95 $\text{mmol C m}^{-2} \text{d}^{-1}$, while in the central Weddell Sea it was
148 substantially lower at 8.3 $\text{mmol C m}^{-2} \text{d}^{-1}$. However, because the study did not characterize the phytoplankton
149 community, the extent to which phytoplankton diversity may have influenced primary production and nutrient
150 drawdown cannot be surmised. To evaluate the summertime fertility of the Weddell Sea and the potential
151 importance of different phytoplankton groups for carbon production and export, we directly measured the rates of
152 total, new, and regenerated production in the western Weddell Sea (predominantly at LCIS), as well as at Fimbul
153 Ice Shelf (FIS) in the south-eastern Weddell Sea. Rates of nitrification were also quantified to account for any
154 nitrate regenerated within the euphotic zone at the time of sampling as this N flux supports regenerated rather than
155 new production (e.g., Yool et al. 2007; Mduyana et al. 2020). We interpret our rate data in the context of
156 coincident measurements of regional hydrography, macronutrient concentrations and ratios, and phytoplankton
157 community composition.

158

159 2. Methods

160 2.1. Field collections

161 Sampling was conducted in the January/February 2019 during the Weddell Sea Expedition onboard the R/V *SA*
162 *Agulhas II* (Dowdeswell et al., 2019). A total of 19 stations were sampled across the Weddell Sea and are
163 categorised based on their geographic position as Antarctic Peninsula (AP), Larsen C Ice Shelf (LCIS), Weddell
164 Gyre (WG), or Fimbul Ice Shelf (FIS) stations (Table 1; Figure 1). Hydrographic data were collected using a
165 Seabird conductivity-temperature-depth (CTD) profiler equipped with a photosynthetically active radiation (PAR)
166 sensor. Density (σ_θ) was derived from CTD measurements of temperature, salinity, and pressure, and
167 was used to identify the water mass distributions. The mixed layer depth (MLD) was determined as the depth at
168 which the Brunt-Väisälä frequency squared (N^2 ; a function of σ_θ) reached a maximum (Schofield et al. 2015).



169 **Figure 1.** Maps of the Weddell Sea, Larsen C Ice Shelf (LCIS; insert a) and Fimbul Ice Shelf (FIS; insert b)
170 showing the position of the stations where rate experiments were conducted during the Weddell Sea Expedition
171 in January/February 2019. The symbols represent the different regions of the Weddell Sea sampled during the
172 expedition (circle – Antarctic Peninsula (AP); diamond – FIS; triangle – LCIS; square – Weddell Gyre (WG)).
173 The general cyclonic circulation of the Weddell Gyre (dashed blue arrow) is illustrated on the central map, with
174 the dashed black arrows indicating the input of modified water masses from Filchner-Ronne Ice shelf (FRIS) and
175 LCIS (Gordon et al. 1993; Schröder et al. 2002; Schodlok et al. 2002). The hypothesized circulation at LCIS
176 (Nicholls et al. 2004; Hutchinson et al. 2020) is shown by the dashed light-blue arrow in insert (a). The 3.125 km
177 sea-ice concentration data [from 31 January 2020](ftp://ftp-projects.cen.uni-hamburg.de/seaice/AMSR2/3.125km) shown in the central panel were taken from
178 <ftp://ftp-projects.cen.uni-hamburg.de/seaice/AMSR2/3.125km> and the bathymetry data (inserts a and b) were taken from
179 ETOPO1 (NOAA National Geophysical Data Center 2009).

180

181 Seawater was collected from discrete depths using a rosette of twenty-four 12 L Niskin bottles. At each station,
182 seawater samples for nutrient analysis were collected throughout the water column (typically at 15 discrete
183 depths), while samples for phytoplankton taxonomy and rate experiments were taken from 3-6 depths (see below)
184 that were selected based on profiles of temperature, [chlorophyll-a](#) fluorescence, and PAR measured during the
185 CTD down-casts.

186

187 Simulated *in situ* experiments were conducted to determine the rates of net primary production (NPP), N uptake
188 (as nitrate (NO_3^-), ammonium (NH_4^+), and urea-N), and nitrite (NO_2^-) oxidation (a measure of nitrification). For

189 NPP and N uptake, seawater was collected from three depths coinciding with the 55%, 10%, and 1% PAR levels,
190 then pre-screened through 200 μm mesh to remove large grazers and transferred to six 1 L and six 2 L
191 polycarbonate bottles per depth. ^{15}N -labeled NO_3^- , NH_4^+ , or urea-N was added to four of the twelve bottles (i.e.,
192 two 1 L and two 2 L bottles per N species) and $\text{NaH}^{13}\text{CO}_3$ was added to the bottles amended with ^{15}N - NH_4^+ . The
193 tracers were added at ~5-10% of the assumed ambient concentrations, yielding final concentrations in each bottle
194 of approximately 100 μM $\text{NaH}^{13}\text{CO}_3$, 1 μM ^{15}N - NO_3^- , 0.05 μM ^{15}N - NH_4^+ , and 0.1 μM ^{15}N -urea-N. Bottles were
195 incubated on the deck for 4-6 hours in a custom-built incubator that was cooled with running surface (~7 m)
196 seawater and equipped with neutral density filters to simulate the relevant light levels. Experiments were
197 terminated via filtration onto 0.3 μm combusted (450°C for 8 hours) glass fibre filters (Sterlitech GF-75) that were
198 stored frozen in combusted (500°C for 5 hours) foil envelopes at -80°C pending analysis.

199
200 Seawater samples for the NO_2^- oxidation experiments were collected from the 55%, 10%, and 1% light levels, just
201 below the MLD, and at 200 m and 500 m. From each depth, seawater was transferred into duplicate 250 mL
202 opaque high-density polyethylene (HDPE) bottles to which ^{15}N - NO_2^- was added to achieve a final tracer
203 concentration of 0.1 μM . An initial 50 mL subsample (T_{initial}) was collected from each HDPE bottle immediately
204 following tracer addition and frozen at -20°C until analysis ashore. The 55%, 10%, 1%, and MLD sample bottles
205 were incubated in the on-deck incubator for 20-30 hours while the 200 m and 500 m samples were incubated in a
206 ~2°C cold room. The experiments were terminated by collection and freezing of 50 mL T_{final} subsamples.

207

2.2. Nutrients

2.2.1. Nutrient concentration analysis

210 $\text{NO}_3^- + \text{NO}_2^-$ and silicic acid ($\text{Si}(\text{OH})_4$) concentrations were measured using a Lachat QuickChem flow injection
211 analysis platform following published auto-analysis protocols (Diamond, 1994; Grasshoff, 1976) in a
212 configuration with a detection limit of 0.5 μM . Duplicate samples were measured for $\text{NO}_3^- + \text{NO}_2^-$ and $\text{Si}(\text{OH})_4$
213 on different days, and the standard deviation for duplicates was ≤ 0.5 μM , with a lower standard deviation for lower-
214 concentration samples. NO_3^- concentrations were determined by subtraction of NO_2^- from $\text{NO}_3^- + \text{NO}_2^-$.
215 Concentrations of phosphate (PO_4^{3-}) and NO_2^- were measured shipboard by standard benchtop colourimetric
216 methods (Strickland and Parsons 1968; Bendschneider et al. 2020; Parsons et al. 1984) using a Thermo Scientific
217 Genesis 30 Visible spectrophotometer. The detection limit was 0.05 μM and the standard deviation for duplicate
218 samples was ≤ 0.05 μM . Aliquots of a certified reference material (JAMSTEC; Lot CG) were analysed during
219 autoanalyzer and manual runs to ensure measurement accuracy.

220

221 NH_4^+ concentrations were measured shipboard following the fluorometric method of Holmes et al. (1999) using
222 a Turner Designs Trilogy fluorometer equipped with a UV module. The detection limit was < 0.05 μM and the
223 standard deviation for duplicate samples was ≤ 0.05 μM . The matrix effect (ME) that results from the calibration
224 of seawater samples with Milli-Q water standards was calculated using the standard addition method (Saxberg
225 and Kowalski, 1979). All samples were corrected for the ME (Taylor et al., 2007), which was always $< 10\%$ and
226 typically $\leq 5\%$. Urea-N concentrations were measured via the colourimetric method of Revilla et al. (2005) using
227 a Thermo Scientific Genesis 30 Visible spectrophotometer equipped with either a 1 cm- or 5 cm-pathlength cell.

228 The detection limit was 0.05 μM and the standard deviation for duplicate samples was $\leq 0.05 \mu\text{M}$. Hereafter, we
 229 use “urea” when referring to urea-N.

230

231 2.2.2. Estimating nutrient depletion

232 The net decrease in euphotic zone nutrient concentrations following nutrient recharge in winter (i.e., the extent of
 233 nutrient depletion due to consumption by phytoplankton), between the start of the growing season until the time
 234 of our sampling, can be estimated for each station as:

235

$$236 \quad X_{\text{depletion}} = [X]_{\text{measured}} - [X]_{\text{source}}$$

$$237 \quad X_{\text{depletion}} = [X]_{\text{source}} - [X]_{\text{measured}} \quad (1)$$

238

239 where $[X]_{\text{source}}$ is the average $[\text{NO}_3^-]$, $[\text{Si}(\text{OH})_4]$ or $[\text{PO}_4^{3-}]$ in winter water (WW; a shallow temperature minimum
 240 layer underlying ASW that is the remnant of the winter mixed layer and considered representative of pre-bloom
 241 surface conditions) and $[X]_{\text{measured}}$ is the measured summertime nutrient concentration (Le Corre and Minas 1983;
 242 Jennings et al. 1984; Goeyens et al. 1995; Hoppema et al. 2007).

243

244 Seasonal melting of sea-ice in the Weddell Sea introduces low-salinity, low-nutrient waters that dilute the
 245 biogeochemistry of the mixed layer (Eicken, 1993), potentially leading to an overestimation of phytoplankton-
 246 driven nutrient depletion. ~~We thus correct X depletion for the effect of ice melt as:~~ We correct for the depletion
 247 in the surface $[\text{NO}_3^-]$, $[\text{Si}(\text{OH})_4]$ or $[\text{PO}_4^{3-}]$ due to sea-ice melt (i.e., the dilution effect) as:

248

$$249 \quad X_{\text{depletion}(\text{corrected})} = X_{\text{depletion}} - X_{\text{depletion}(\text{melt water})} \quad (2a)$$

250

251 where $X_{\text{depletion}(\text{melt water})}$ is the decrease in surface $[\text{NO}_3^-]$, $[\text{Si}(\text{OH})_4]$ or $[\text{PO}_4^{3-}]$ due to sea-ice melt, calculated
 252 as:

$$253 \quad X_{\text{depletion}(\text{melt water})} = [X]_{\text{source}} - [X]_{\text{melt water}} \quad (2b)$$

254 where:

$$255 \quad X_{\text{depletion}(\text{melt water})} = [X]_{\text{sea-ice}} (f_{\text{sea-ice}}) + [X]_{\text{source}} (1 - f_{\text{sea-ice}}) \quad (2b)$$

256

257 Here, the nutrient concentrations in summertime sea-ice ($[X]_{\text{sea-ice}}$) are assumed to be: $[\text{NO}_3^-]_{\text{sea-ice}} = 1 \mu\text{M}$,
 258 $[\text{Si}(\text{OH})_4]_{\text{sea-ice}} = 5 \mu\text{M}$, and $[\text{PO}_4^{3-}]_{\text{sea-ice}} = 0.3 \mu\text{M}$ (Fripiat et al., 2014, 2017), and:

259

$$260 \quad f_{\text{sea-ice}} = \frac{\text{salinity}_{\text{measured}} - \text{salinity}_{\text{source}}}{\text{salinity}_{\text{sea-ice}} - \text{salinity}_{\text{source}}} \quad (2c)$$

261

262 with $\text{salinity}_{\text{sea-ice}}$ taken to be 5 based on sea-ice salinity measurements made during the cruise (Dowdeswell et al.,
 263 2019) and $\text{salinity}_{\text{source}}$ set to 34.2 at FIS and 34.4 at the other stations (the salinity of WW; Figure 2ge-insert). On
 264 average, correcting for sea-ice melt changed the estimates of X depletion by $0.4 \pm 0.9\%$. Hereafter, all references
 265 to nutrient depletion are to the computed values of $X_{\text{depletion}(\text{corrected})}$. The approach above for calculating X
 266 $\text{depletion}(\text{corrected})$ assumes, following correction for sea-ice melt, that nutrient drawdown is due to phytoplankton
 267 assimilation only, a reasonable assumption in the Weddell Sea in summer.

Formatted: Justified

268

269 2.3. Uptake rates

270 Incubation filters were oven-dried for 24 hours at 40°C, then folded into tin cups. Samples were analysed using a
271 Flash Elemental Analyser 1112 Series coupled to a Delta V Plus isotope ratio mass spectrometer (IRMS) in a
272 configuration with a detection limit of 2 µg C and 1 µg N. Blanks (combusted unused filters + tin cups) and
273 laboratory running standards, calibrated to certified IAEA reference materials, were run after every five samples.
274

275 The specific rates of carbon fixation (V_C) and NO_3^- , NH_4^+ and urea uptake ($V_{\text{NO}_3^-}$, $V_{\text{NH}_4^+}$, V_{urea} ; d^{-1}) were calculated
276 according to equation 2 in Dugdale and Wilkerson (1986). NPP and the absolute rates of NO_3^- , NH_4^+ and urea
277 uptake (ρNO_3^- , ρNH_4^+ and ρurea ; $\mu\text{M d}^{-1}$) were then determined by multiplying V_C by the concentration of
278 particulate organic carbon ([POC]) and $V_{\text{NO}_3^-}$, $V_{\text{NH}_4^+}$ and V_{urea} by the concentration of particulate organic nitrogen
279 ([PON]) (Dugdale and Wilkerson 1986; equation 3).

280

281 2.4. NO_2^- oxidation rates

282 The T_{initial} and T_{final} samples from the NO_2^- oxidation incubations were measured for the $\delta^{15}\text{N}$ of NO_3^- ($\delta^{15}\text{N}_{\text{NO}_3^-}$;
283 where $\delta^{15}\text{N} = ((^{15}\text{N}_{\text{sample}}/^{14}\text{N}_{\text{sample}})/(^{15}\text{N}_{\text{standard}}/^{14}\text{N}_{\text{standard}}) - 1) \times 1000$) using the denitrifier method (Sigman et al.
284 2001; McIlvin and Casciotti 2011). Prior to isotopic analysis, all samples were treated with sulfamic acid to
285 remove NO_2^- as the denitrifier method converts both NO_2^- and NO_3^- to N_2O gas (Granger and Sigman, 2009); the
286 difference in $\delta^{15}\text{N}_{\text{NO}_3^-}$ between the T_{final} and T_{initial} samples was then taken as the $^{15}\text{NO}_3^-$ enrichment due to $^{15}\text{NO}_2^-$
287 oxidation (Peng et al. 2015). Results were referenced to atmospheric N_2 using certified reference materials (IAEA-
288 NO-3, USGS-34, and USGS-32; Gonfiantini 1984; Böhlke and Coplen 1995; Böhlke et al. 2003). The rate of
289 NO_2^- oxidation ($V_{\text{NO}_2^-}$; nM d^{-1}) was calculated following Peng et al. (2015) as:

290

$$291 V_{\text{NO}_2^-} = \frac{\Delta[^{15}\text{NO}_3^-]}{f_{\text{NO}_2^-}^{15} \times t} \quad (3)$$

292

293 where $\Delta[^{15}\text{NO}_3^-]$ is the difference in the concentration of $^{15}\text{NO}_3^-$ between the end and the start of the experiment
294 (i.e., $T_{\text{final}} - T_{\text{initial}}$) due to NO_2^- oxidation, $f_{\text{NO}_2^-}^{15}$ is the fraction of $^{15}\text{NO}_2^-$ at the start of the incubation, and t is the
295 length of the incubation (days). The detection limit for $V_{\text{NO}_2^-}$ ranged from 0.06-0.46 nM d^{-1} (calculated following
296 Santoro et al. 2013). We take $V_{\text{NO}_2^-}$ as a measure of the nitrification rate given that NO_2^- oxidation is the step in
297 the nitrification pathway that produces NO_3^- .

298

299 To determine relative carbon export potential at each station, we calculated the f-ratio (a measure of
300 new production relative to total (i.e., new+regenerated) production) using the absolute N uptake and
301 NO_2^- oxidation rates and a modified version of the Eppley and Peterson (1979) equation:

302

$$303 \text{f-ratio}_{(\text{excluding urea})} = \frac{\rho\text{NO}_3^- - V_{\text{NO}_2^-}}{\rho\text{NO}_3^- + \rho\text{NH}_4^+} \quad (4a)$$

304

305
$$f\text{-ratio}_{(\text{including urea})} = \frac{\rho\text{NO}_3^- - V_{\text{NO}_2^-}}{\rho\text{NO}_3^- + \rho\text{NH}_4^+ + \rho_{\text{urea}}} \quad (4b)$$

306
 307 Equation 4a and b account for euphotic zone nitrification (Mdotyana et al. 2020), which yields regenerated rather
 308 than new NO_3^- that is then available for phytoplankton to consume. Not accounting for $V_{\text{NO}_2^-}$ could result in the f-
 309 ratio being overestimated (Yool et al. 2007). Equation 4b accounts for urea uptake, that was either measured (at
 310 the LCIS stations and WG1) or calculated (at the AP, FIS and WG2) (see section 3.3.4 below).

311

312 **2.5. Phytoplankton taxonomy and carbon biomass**

313 At all stations, microphytoplankton samples were collected between the surface and 30 m using a HYDROBIOS
 314 conical plankton net ($r = 12.5$ cm; $h = 50$ cm) with a mesh size of $55 \mu\text{m}$. Samples were transferred to 50 mL
 315 centrifuge tubes, fixed with 10 μL of 25% glutaraldehyde, and stored at room temperature in the dark until later
 316 analysis via light and scanning electron microscopy. Additionally, samples for flow cytometry were collected in
 317 50 mL centrifuge tubes from Niskin bottles fired at the 55%, 10%, and 1% PAR depths. These samples were fixed
 318 with 10 μL of 25% glutaraldehyde and stored in the dark at 4°C until analysis.

319

320 Onshore, each preserved net-sample was homogenized, and one drop (40 μL) was wet mounted on a slide. All the
 321 cells on the slide with intact chloroplasts (i.e., alive at the time of sampling) were counted at 400x or 630x
 322 magnification using a Zeiss AxioScope A1 light microscope (LM). The number of cells/mL was calculated as:

323

324
$$\text{cells per mL} = \left[A \left(\frac{1}{\text{mL}} \right) \left(\frac{n}{V} \right) \right] \quad (5)$$

325

326 where A is the number of cells per drop, mL is the volume of water sampled (1470000 mL; computed using the
 327 volume of a cylinder, $\pi r^2 h$, where $r = 125$ mm and $h = 30000$ mm depth), n is the total volume of concentrated
 328 sample, and V is the volume of 1 drop of concentration sample.

329

330 An aliquot of 5 mL from each preserved sample was cleaned by removing carbonate particles and organic matter
 331 using 10% hydrochloric acid and 37% hydrogen peroxide, respectively. After thorough rinsing with distilled
 332 water, permanent slides were prepared by pipetting the cleaned material onto acid-washed coverslips, air drying
 333 them overnight, and mounting the cover slips onto glass slides using Naphrax® mountant (refractive index = 1.7).
 334 The permanent slides were examined using a Zeiss AxioScope A1 LM equipped with differential interference
 335 contrast at 1000x magnification (under oil immersion) for identification of the diatom cells to the lowest
 336 taxonomic classification possible. Stubs were also prepared from the cleaned material for Scanning Electron
 337 Microscopy (SEM), with a JEOL JSM 7001F field emission SEM used to visualize the morphological features
 338 not evident under LM.

339

340 The average size (μm) and carbon content (pg C cell^{-1}) of each identified diatom species was taken from Leblanc
 341 et al. (2012) for high latitude locations ($50 - 70^\circ\text{S}$) (Table S1), and the carbon content of colonial *P. antarctica* was
 342 estimated as $13.6 \text{ pg C cell}^{-1}$ (Mathot et al., 2000) for single cells within a colony. Since the majority of *P.*
 343 *antarctica* were in spherical colony form, the total colony carbon biomass (C_{COL}) was calculated as:

344
345
$$C_{COL} = [13.60 \times N_C] + C_M \quad (6)$$

346

347 where N_C is the number of cells counted per litre, C_M is the mucus-related carbon calculated as $C_M = 0.213 \times$
348 $V_{COL} + 4.58$, and V_{COL} is the volume of the spherical colony, calculated as $V_{COL} = 417 \times N_C^{1.67}$ (Mathot et al.,
349 2000).

350
351 Flow cytometry samples were analyzed using a BD LSR II SORP flow cytometer with blue/red/green laser
352 configuration. The size-class to which each cell belonged was defined based on its forward scatter area (FSC-A)
353 relative to the FSC-A of 2.8 μm and 20 μm beads (Figure S1a). Once categorized as either picoplankton (<2.8
354 μm), nanoplankton (2.8-20 μm), or microplankton (>20 μm), the cells were grouped into six populations based
355 on their orange fluorescence (indicative of phycoerythrin; PE) relative to their red fluorescence (indicative of
356 chlorophyll-a; chl-a): two *Synechococcus* populations (Syn 1 and Syn 2), one picoeukaryote population (PicoEuk),
357 two nanoeukaryote populations (NanoEuk 1 and NanoEuk 2), and one microeukaryote population (MicroEuk; see
358 section S2 in the Supplemental Information for details of population identification). The biovolumes of the
359 eukaryotic populations were estimated based on their FSC-A relative to that of six beads of known size and volume
360 (Figure S1c; Table S2). *Synechococcus* had an unrealistically high measured FSC-A, which is an artefact of the
361 high ratio of photosystem I to photosystem II of the group compared to the other phytoplankton populations. This
362 elevates electron chain activity, leading to an increase in the emission spectrum and low excitation of the
363 *Synechococcus* populations (Kaprelyants and Kell 1993; Sunda and Huntsman 2015). The biovolume of
364 *Synechococcus* was thus assumed to be 1 μm^3 (Kana and Glibert, 1987; Paulsen et al., 2015). Biovolume is used
365 here as a proxy for biomass.

366 367 **3. Results**

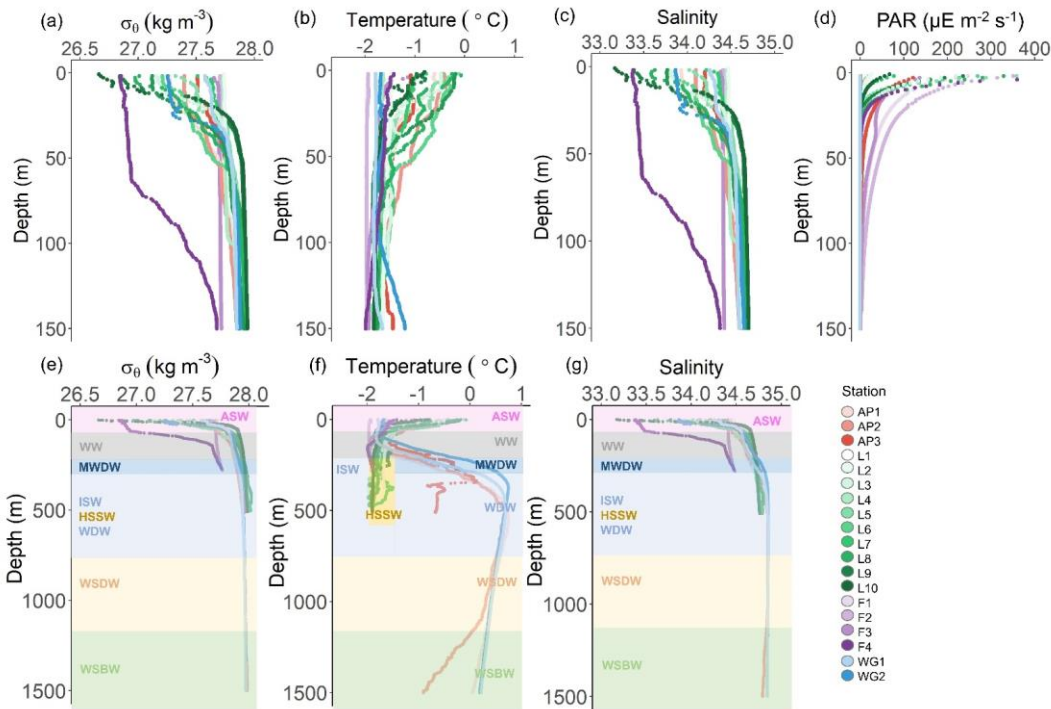
368 **3.1. Water column hydrography**

369 Throughout the study region, relatively cool and fresh (-2 to 0°C and 33.0 to 34.5) ASW occurred between the
370 surface and 135 m (Figure 2). Through this layer and down to 200 m, salinity increased with depth while
371 temperature decreased, reaching a local minimum (-1.6°C) at ~100 m. These hydrographic changes are
372 characteristic of WW, which is considered a summertime record of winter conditions and a reflection of the initial
373 state from which the mixed layer evolves over the spring/summer growing season (Altabet and Francois, 2001).
374 Below WW at the AP and WG stations, salinity remained constant while temperature increased with depth,
375 reaching a local maximum (0.5°C) at 500 m and 300 m for the AP and WG, respectively. This feature is
376 characteristic of Warm Deep Water (WDW), a temperature maximum layer that is a modified form of Circumpolar
377 Deep Water (CDW) (Muench and Gordon, 1995; Fahrbach et al., 1995). Below WW at the LCIS and FIS stations,
378 salinity increased, and temperature decreased with depth, reaching a local salinity maximum (34.6 at LCIS and
379 34.3 at FIS) and temperature minimum ($\leq -1.8^\circ\text{C}$). The increase in salinity is characteristic of High Salinity Shelf
380 Water (HSSW) produced by brine rejection during sea-ice formation, while the decrease in temperature is
381 indicative of Ice Shelf Water (ISW) produced by the supercooling of ASW under the ice shelves (Fahrbach et al.
382 1995; Nicholls et al. 2009; Hutchinson et al. 2020). The densities of WW, WDW, HSSW, and ISW are contiguous,
383 with the mixed product of these waters termed Modified Warm Deep Water (MWDW) (Fahrbach et al., 1995).

384 Below WDW at the AP and WG stations, temperature decreased due to the presence of Weddell Sea Deep Water
 385 (WSDW; temperature range of -0.7 to 0°C) and Weddell Sea Bottom Water (WSBW; temperature $\leq -0.7^{\circ}\text{C}$)
 386 (Fahrbach et al., 1995; Muench and Gordon, 1995).

387
 388 Variability in the density of ASW was observed among the stations (Figure 2a). The surface density profiles at
 389 the AP, WG, and early-summer FIS stations were very similar, while the late-summer density profile at FIS
 390 revealed lower-density waters in the upper 100 m. At LCIS, the surface density profiles were highly variable, and
 391 no consistent pattern was observed, although the most northern stations (L9 and L10; Figure 1) were characterised
 392 by the lowest densities. Stations L1 and L3, situated closest to the ice shelf, were characterised by the highest
 393 densities, contiguous with the underlying WW layer.

394
 395 The MLD appeared most strongly controlled by salinity at all stations and was always shallower than the depth
 396 of the euphotic zone (Z_{eu} ; Table 1; Figure 2a-d), the latter defined as the depth to which 1% of surface PAR
 397 penetrated (Kirk 1994). The deepest MLD and Z_{eu} were observed at FIS in early summer (average MLD of 103.0
 398 ± 36.6 m and Z_{eu} of 91.7 ± 14.4 m; $n = 3$), while the shallowest MLD and Z_{eu} were observed at LCIS (average
 399 MLD of 13.9 ± 5.9 m and Z_{eu} of 28.5 ± 9.1 m; $n = 10$) (Figure 2d; Table 1). The rates of NPP, N uptake and
 400 nitrification were therefore trapezoidally-integrated to Z_{eu} rather than to the MLD since we assume that
 401 phytoplankton were active at least to the depth of 1% PAR.

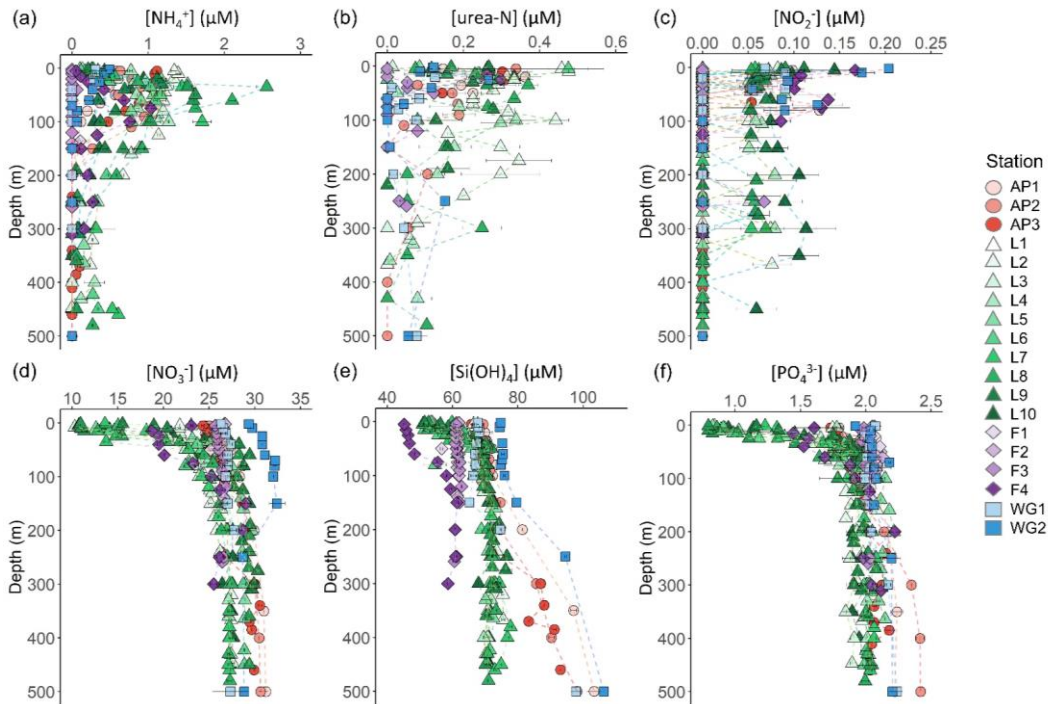


402 **Figure 2.** Depth profiles of (a) potential density (σ_{θ}), (b) potential temperature, (c) absolute salinity, and (d)
 403 photosynthetically active radiation (PAR) in the upper 150 m and (e) σ_{θ} , (f) potential temperature, and (g) absolute

404 salinity in the upper 1500 m at all stations. The water masses present at each station, identified by their temperature
 405 and salinity characteristics, are denoted in panels (e-g) as follows: WSBW – Weddell Sea Bottom Water, WSDW
 406 – Weddell Sea Deep Water, WDW – Warm Deep Water, MWDW – Modified Warm Deep Water, ISW – Ice
 407 Shelf Water, HSSW – High Salinity Shelf Water, WW – Winter Water, ASW – Antarctic Surface Water. In panel
 408 (f), the dark yellow rectangle indicates HSSW. The general station locations are indicated by the different marker
 409 colours: red shades – Antarctic Peninsula, green shades – Larsen C Ice Shelf, blue shade – Weddell Gyre, light
 410 purple shades – early summer Fimbul Ice Shelf, and dark purple – late summer Fimbul Ice Shelf.
 411

412 3.2. Nutrient concentrations

413 The concentrations of the regenerated N forms (i.e., NH_4^+ and urea) were generally low in the surface and
 414 increased with depth to reach a maximum in the shallow subsurface (Figure 3a and b), below Z_{eup} , before decreasing
 415 again to below detection by 200–300 m (Figure 3a and b; Table 1). A sharp maximum in the NH_4^+ concentration
 416 was observed near Z_{eup} at all stations, indicative of the depth of maximum net remineralisation. Urea
 417 concentrations were more variable, likely due to variability in the processes that produce this N form (e.g.,
 418 bacterial excretion; Berges and Mulholland 2008). The highest average concentrations of regenerated N in the
 419 euphotic zone were observed at LCIS and FIS in late summer ($0.62 \pm 0.30 \mu\text{M}$ for NH_4^+ and $0.21 \pm 0.07 \mu\text{M}$ for
 420 urea), while the lowest concentrations were observed at FIS in early summer (below detection for both NH_4^+ and
 421 urea). Elevated regenerated N concentrations were also observed at the AP stations (euphotic zone average of 0.8
 422 $\pm 0.3 \mu\text{M}$ for NH_4^+ and $0.2 \pm 0.06 \mu\text{M}$ for urea), while low concentrations were observed at the WG stations
 423 (euphotic zone average of $0.3 \pm 0.1 \mu\text{M}$ for NH_4^+ and $0.1 \pm 0.0 \mu\text{M}$ for urea).



424 **Figure 3.** Depth profiles (0–500 m) of (a) NH_4^+ , (b) urea-N, (c) NO_2^- , (d) NO_3^- , (e) Si(OH)_4 , and (f) PO_4^{3-}
 425 concentrations. For all panels, the error bars represent ± 1 SD of replicate samples ($n = 2-3$). For NO_3^- , which was

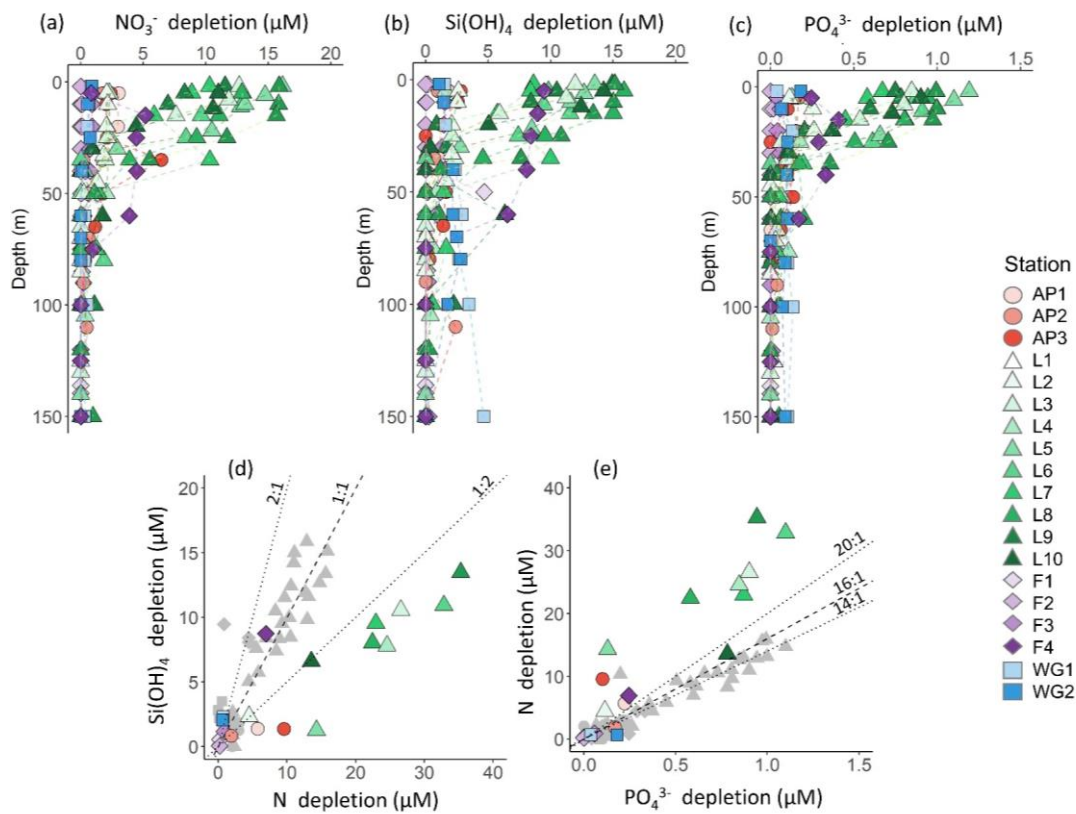
426 calculated as $\text{NO}_3^- + \text{NO}_2^- - \text{NO}_2^-$, error has been propagated according to standard statistical practices. [Note that](#)
427 [the x-axis scales in panels \(d-f\) do not start at zero.](#)
428

429 The concentrations of NO_2^- were generally low throughout the euphotic zone, and decreased to below detection
430 by 120 m at the FIS, AP, and WG stations (with the exception of a single sample from the early-summer FIS),
431 and by 500 m at LCIS (Figure 3c). A high degree of variability was observed, with the highest surface-layer NO_2^-
432 concentrations occurring in the WG and at FIS in late summer (average euphotic zone NO_2^- concentrations of 0.08
433 $\pm 0.06 \mu\text{M}$ and $0.12 \pm 0.03 \mu\text{M}$, respectively).
434

435 The euphotic zone concentrations of NO_3^- , Si(OH)_4 and PO_4^{3-} decreased towards the surface due to assimilation
436 by phytoplankton (Figure 3d-f). The lowest surface concentrations of NO_3^- and PO_4^{3-} were observed at LCIS (16.6
437 $\pm 3.8 \mu\text{M}$ and $1.3 \pm 0.4 \mu\text{M}$, respectively) and of Si(OH)_4 was observed at FIS in late summer ($46.1 \pm 0.8 \mu\text{M}$).
438 The highest surface concentrations of NO_3^- , PO_4^{3-} and Si(OH)_4 occurred in [the WG \(\$28.8 \pm 2.4 \mu\text{M}\$, \$2.0 \pm 0.54\$
439 \[μM, and \\$70.1 \pm 3.8 \mu\text{M}\\$, respectively\\)\]\(#\), \[early-summer at FIS \\(\\$26.5 \pm 0.32 \mu\text{M}\\$, \\$2.0 \pm 0.04 \mu\text{M}\\$ and \\$61.6 \pm 0.5 \mu\text{M}\\$,\]\(#\)
440 \[respectively\\)\]\(#\). Elevated \$\text{Si\(OH\)}_4\$ and \$\text{PO}_4^{3-}\$ concentrations were observed between 200 and 500 m at the AP and
441 WG stations due to the presence of WDW at these stations versus shelf waters \(i.e., ISW and HSSW\) at LCIS and
442 FIS. The depth of maximum remineralisation in the open Weddell Sea is 300-500 m, the depth range occupied by
443 WDW \(Vernet et al. 2019, and references therein\). \[WDW has the longest residence time of all water masses in\]\(#\)
444 \[the Weddell Sea, and has therefore undergone the greatest modification by physical and biogeochemical processes\]\(#\)
445 \[\\(Whitworth and Nowlin 1987; Hoppema et al. 2015\\). The depth of maximum remineralisation in the open Weddell\]\(#\)
446 \[Sea is 300-500 m, the depth range occupied by WDW \\(Vernet et al. 2019, and references therein\\).\]\(#\) The high rates
447 of remineralisation, and therefore nutrient accumulation, in WDW account for the elevated nutrient concentrations
448 observed in WDW relative to the shelf water masses \(Whitworth and Nowlin, 1987\). Estimates of \$\text{NO}_3^-\$, \$\text{Si\(OH\)}_4\$,
449 and \$\text{PO}_4^{3-}\$ depletion \(i.e., X depletion_{\(corrected\)}; equation 2\) were highest at LCIS \(average \$\text{NO}_3^-\$ depletion of \$8.3 \pm\$
450 \$3.9 \mu\text{M}\$, \$\text{Si\(OH\)}_4\$ depletion of \$8.3 \pm 4.0 \mu\text{M}\$, and \$\text{PO}_4^{3-}\$ depletion of \$0.6 \pm 0.3 \mu\text{M}\$ \), while the lowest nutrient
451 depletions occurred in early summer at FIS \(average \$\text{NO}_3^-\$ depletion of \$0.3 \pm 0.3 \mu\text{M}\$, \$\text{Si\(OH\)}_4\$ depletion of \$0.6 \pm\$
452 \$0.6 \mu\text{M}\$, and \$\text{PO}_4^{3-}\$ depletion of \$0.00 \pm 0.02 \mu\text{M}\$ \) \(Figure 4a-c; Table 1\).
453](#)

454 Variations in the depletion ratios of $\text{Si(OH)}_4:\text{NO}_3^-$ and $\text{NO}_3^-:\text{PO}_4^{3-}$ can be used as indicators of the nutrient status
455 of the phytoplankton community, particularly diatoms. Under iron-replete conditions, diatoms have been observed
456 to consume Si(OH)_4 and NO_3^- in a ratio of $\sim 1:1$, and NO_3^- and PO_4^{3-} in a ratio of $\sim 14:1$ (Hutchins and Bruland,
457 1998; Takeda, 1998; Ragueneau et al., 2000; Mosseri et al., 2008), while under conditions of limitation, the ratio
458 of $\text{Si(OH)}_4:\text{NO}_3^-$ uptake rises (to $>2:1$) and $\text{NO}_3^-:\text{PO}_4^{3-}$ uptake decreases (to as low as $10:1$) (Arrigo et al., 1999;
459 Franck et al., 2000; Brzezinski et al., 2003; Green and Sambrotto, 2006; Mosseri et al., 2008; Weber and Deutsch,
460 2010a; Martiny et al., 2013). Additionally, the dominance of one phytoplankton species over another may cause
461 deviations in the $\text{NO}_3^-:\text{PO}_4^{3-}$ depletion ratio. For example, in regions dominated by *P. antarctica*, Arrigo et al.
462 (1999) observed a $\text{NO}_3^-:\text{PO}_4^{3-}$ depletion ratio of $\sim 20:1$, while in areas dominated by iron-deplete diatoms, this
463 ratio was $\sim 10:1$. The $\text{NO}_3^-:\text{PO}_4^{3-}$ depletion ratios can thus also yield insights into the dominant phytoplankton
464 species active in the upper water column. In our study, the average euphotic zone $\text{Si(OH)}_4:\text{NO}_3^-$ depletion ratios
465 ranged from 0.5 to 6.1 (Table 1), with the highest ratios estimated for the WG stations (average of 5.4 ± 5.5) and
466 at FIS in late summer (average of 2.3 ± 0.5). The euphotic zone average $\text{NO}_3^-:\text{PO}_4^{3-}$ depletion ratios were more

467 variable, ranging from 3.7 ± 1.5 to 48.6 ± 11.5 , with the lowest ratios computed for the WG stations (average of
 468 4.1 ± 1.5) and the highest for FIS in early summer (average of 33.7 ± 3.6). FIS stations F3 and F4 (average of 2.7
 469 ± 2.8 ; the same station occupied in early (F3) and late summer (F4)) In the latter case, the degree of Si(OH)_4 and
 470 PO_4^{3-} depletion was extremely low (Table 1), which likely accounts for the variable and anomalous $\text{Si(OH)}_4:\text{NO}_3^-$
 471 and $\text{NO}_3^-:\text{PO}_4^{3-}$ depletion ratios computed for stations F1-F3.

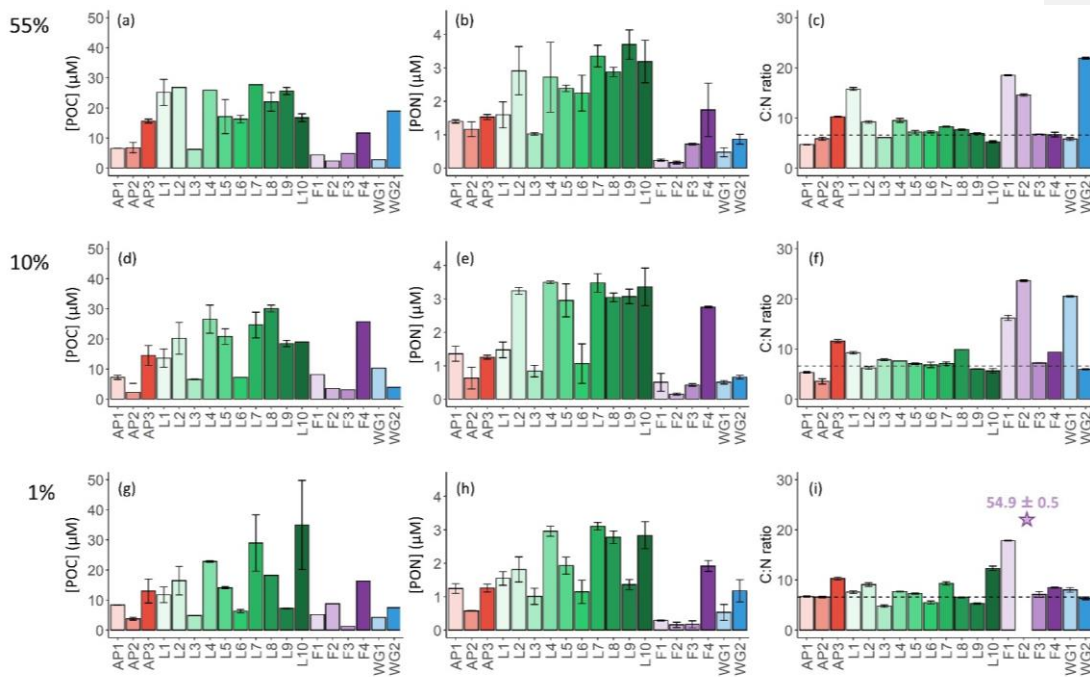


472 **Figure 4.** Depth profiles (0-150 m) of (a) NO_3^- depletion, (b) Si(OH)_4 depletion, and (c) PO_4^{3-} depletion at each
 473 station. Also shown are scatterplots of (d) Si(OH)_4 depletion versus total N depletion (coloured symbols; see text
 474 for details) and Si(OH)_4 depletion versus NO_3^- depletion (grey symbols) and (e) PO_4^{3-} depletion versus total N
 475 depletion (coloured symbols) and PO_4^{3-} depletion versus NO_3^- depletion (grey symbols) at each station. The
 476 dashed line in panel (d) represents the 1:1 Si:N depletion ratio, expected for iron-replete diatoms (Ragueneau et
 477 al. 2000; Hutchins and Bruland 1998; Takeda 1998; Mosseri et al. 2008), while the dotted lines represent the 2:1
 478 Si:N ratio, expected for iron-limited diatoms (Arrigo et al., 1999; Franck et al., 2000; Brzezinski et al., 2003;
 479 Green and Sambrotto, 2006; Mosseri et al., 2008; Weber and Deutsch, 2010a; Martiny et al., 2013), and the 1:2
 480 Si:N ratio, indicative of enhanced activity of non-siliceous phytoplankton. The dashed line in panel (e) represents
 481 the 16:1 N:P depletion ratio (the Redfield ratio), while the dotted lines represent the 20:1 N:P ratio, expected for
 482 *P. antarctica*, and the 14:1 N:P ratio, expected for iron-replete diatoms (Hutchins and Bruland 1998; Takeda 1998;
 483 Arrigo et al. 1999; Ragueneau et al. 2000; Mosseri et al. 2008).
 484

485 3.3. Upper ocean biomass, NPP and N uptake rates

486 3.3.1. Particulate organic carbon and nitrogen

487 The highest concentrations of POC and PON were observed in the surface at all stations (Figure 5a and b),
 488 decreasing towards Z_{eu} (Figure 5g and h). Averaged over the euphotic zone, the lowest POC and PON
 489 concentrations occurred in early summer at FIS ($4.6 \pm 1.5 \mu\text{M}$ and $0.3 \pm 0.1 \mu\text{M}$, respectively) and the highest at
 490 LCIS ($17.9 \pm 7.3 \mu\text{M}$ and $2.5 \pm 0.8 \mu\text{M}$; Table 2). Across the region, the biomass C:N ratio was fairly uniform
 491 throughout the euphotic zone, except at stations F1, F2, WG1, and WG2 (Figure 5c, f and i). In general, the FIS
 492 and WG stations were characterized by significantly higher C:N ratios than those expected from Redfield
 493 stoichiometry (C:N = 6.63:1), averaging 16.5 ± 8.8 and 12.3 ± 1.8 , respectively. By contrast, at the LCIS stations,
 494 the biomass C:N ratios were close to the Redfield ratio (7.4 ± 1.9), while the AP stations were characterized by
 495 slightly higher C:N ratios (8.3 ± 2.5).



496 **Figure 5.** Bar plots of (a, d, g) POC concentrations, (b, e, h) PON concentrations, and (c, f, i) biomass C:N ratios
 497 measured at the 55% (a-c), 10% (d-f), and 1% light levels (g-i). The stations are labelled on the x-axis, and the
 498 general stations locations are indicated by the different colours: red shades – Antarctic Peninsula, green shades –
 499 Larsen C Ice Shelf, blue shade –Weddell Gyre, light purple shades – early summer Fimbul Ice Shelf, and dark
 500 purple – late summer Fimbul Ice Shelf. The dotted black horizontal line in panels (c), (f), and (i) shows the
 501 Redfield C:N ratio of 6.63. The purple star in panel (i) indicates the anomalously high C:N ratio estimated for the
 502 1% PAR depth at station F2. The purple star in panel (i) indicates the anomalously high C:N ratio estimated for the
 503 1% PAR depth at station F2. The error bars represent ± 1 SD of replicate samples ($n = 2-6$). Where applicable,
 504 the error has been propagated according to standard statistical practices.

505 3.3.2. Rates of NPP and N uptake

506 At all stations, NPP was generally highest at the surface (Figure 6a) and decreased towards Z_{eu} (Figure 6i). The
 507 highest depth-specific (as opposed to integrated) rates were observed at LCIS (except at station L10 where the
 508 rates were very low), while the lowest rates occurred in early summer at FIS (with particularly low rates measured
 509 at station F1; Figure 6a, e and i). At the WG stations and at FIS in late summer, the rates of NPP were comparable

510 to the lower end of the rates observed at LCIS, while NPP along the AP increased shoreward (i.e., the lowest rates
511 were observed at AP1 and the highest at AP3) to values similar to those observed at LCIS. The highest euphotic
512 zone-integrated rates of NPP were observed at AP3 ($65.0 \pm 0.1 \text{ mmol m}^{-2} \text{ d}^{-1}$) and L5 ($61.0 \pm 0.7 \text{ mmol m}^{-2} \text{ d}^{-1}$),
513 while the lowest occurred at L10 ($1.8 \pm 0.04 \text{ mmol m}^{-2} \text{ d}^{-1}$) (Table 2).

514

515 As per NPP, the rates of ρNO_3^- decreased towards Z_{eu} at all stations (Figure 6b, f and j), as did the extent of NO_3^-
516 depletion (Figure 4a). The depth-specific rates of ρNO_3^- were highest at LCIS and lowest in early summer at FIS.
517 However, because the euphotic zone was generally shallower at LCIS than at the other stations, the euphotic zone-
518 integrated rates of ρNO_3^- were fairly similar across the study region, with the largest variability observed at LCIS
519 (Table 2). In late summer at FIS, integrated ρNO_3^- was on average higher than at LCIS ($3.9 \pm 0.03 \text{ mmol m}^{-2} \text{ d}^{-1}$
520 at F4 versus an average of $2.2 \pm 1.1 \text{ mmol m}^{-2} \text{ d}^{-1}$ at LCIS), with depth-specific rates that were double those
521 measured at FIS in early summer. The sea-ice at FIS had completely melted by late summer, which likely
522 contributed to the increase in ρNO_3^- later in the season. The highest euphotic zone-integrated rates of ρNO_3^- were
523 observed at stations F3 and L5 ($4.8 \pm 0.07 \text{ mmol m}^{-2} \text{ d}^{-1}$ and $4.7 \pm 0.04 \text{ mmol m}^{-2} \text{ d}^{-1}$, respectively). At L5, this
524 elevated rate coincided with low euphotic zone NO_3^- concentrations ($12.0 \pm 1.9 \text{ }\mu\text{M}$; Figure 3d) and a high degree
525 of NO_3^- depletion ($10.9 \pm 2.3 \text{ }\mu\text{M}$; Figure 4a). The lowest euphotic zone-integrated rates of ρNO_3^- occurred at
526 station L10 ($0.5 \pm 0.0 \text{ mmol m}^{-2} \text{ d}^{-1}$).

527

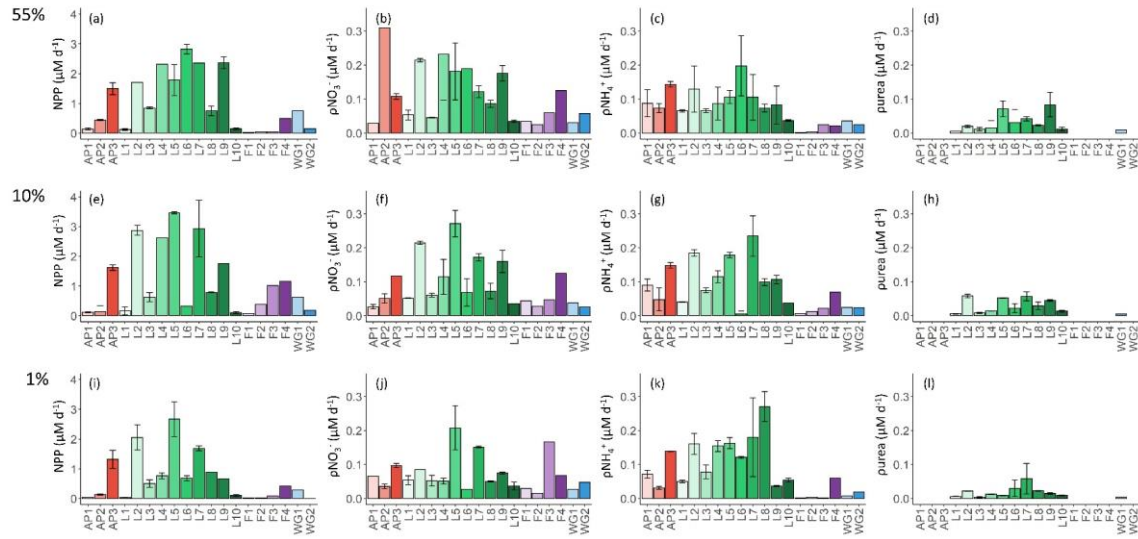
528 At all stations, rates of ρNH_4^+ increased with depth, reaching a maximum at Z_{eu} (Figure 6c, g and k). The highest
529 depth-specific rates of ρNH_4^+ were observed at LCIS and the lowest at FIS in early summer. Euphotic zone-
530 integrated rates of ρNH_4^+ at the AP stations were comparable to those observed at LCIS (regional average of 3.3
531 $\pm 2.2 \text{ mmol m}^{-2} \text{ d}^{-1}$ and $2.5 \pm 1.3 \text{ mmol m}^{-2} \text{ d}^{-1}$, respectively), while the rates at the WG stations and at FIS in late
532 summer were comparable to the lower end of the LCIS rates (average of $2.0 \pm 0.2 \text{ mmol m}^{-2} \text{ d}^{-1}$ at WG and $1.9 \pm$
533 $0.0 \text{ mmol m}^{-2} \text{ d}^{-1}$ at FIS). The early- to late-summer rise in the euphotic zone-integrated rates of ρNH_4^+ at FIS
534 coincided with an increase in the average euphotic zone NH_4^+ concentration from below detection to 0.2 ± 0.1
535 μM (Figure 3a). At the AP, LCIS, and WG stations, the rates of ρNH_4^+ were similar to the coincident rates of
536 ρNO_3^- , while at FIS, ρNH_4^+ was less than half of ρNO_3^- (Table 2). The highest euphotic zone-integrated rates of
537 ρNH_4^+ were observed at station AP3 ($5.8 \pm 0.0 \text{ mmol m}^{-2} \text{ d}^{-1}$), coincident with a high average euphotic zone NH_4^+
538 concentration ($1.1 \pm 0 \text{ }\mu\text{M}$). The lowest integrated ρNH_4^+ occurred at station F1 ($0.4 \pm 0.0 \text{ mmol m}^{-2} \text{ d}^{-1}$) where
539 the concentration of NH_4^+ in the euphotic zone was below detection.

540

541 Rates of purea were only measured at the LCIS stations and WG1 (Figure 6d, h and i; Table 2). A high degree of
542 variability in purea was observed at LCIS, with euphotic zone-integrated rates ranging from 0.2 to 1.1 mmol m^{-2}
543 d^{-1} (average of $0.6 \pm 0.3 \text{ mmol m}^{-2} \text{ d}^{-1}$). This variability appears to be related to the urea concentrations, with the
544 highest rates of purea coinciding with the highest ambient urea concentrations (e.g., station L5), and vice versa
545 (e.g., station L4) (Figure 3b). On average, the rates of purea in the WG were half the rates of ρNH_4^+ , and urea
546 concentrations were low (Figure 3b; Table 2).

547

548



549 **Figure 6.** Daily rates of (a, e, i) NPP, (b, f, j) ρNO_3^- , (c, g, k) ρNH_4^+ , and (d, h, l) purea for the 55% (a-d), 10%
550 (e-h), and 1% light levels (i-l). Where there are no bars in panels (d), (h) and (l), no data are available. The stations
551 are labelled on the x-axis, and the general station locations are indicated by the different colours: red shades –
552 Antarctic Peninsula, green shades – Larsen C Ice Shelf, blue shade – Weddell Gyre, light purple shades – early
553 summer Fimbul Ice Shelf, and dark purple – late summer Fimbul Ice Shelf. The error bars represent ± 1 SE of
554 replicate experiments ($n = 2$).

555

556 3.3.3. Rates of nitrite oxidation

557 Rates of $V_{\text{NO}_2^-}$ were low throughout the euphotic zone across the study region (average euphotic zone-integrated
558 rates of $20.8 \pm 31.3 \mu\text{mol m}^{-2} \text{d}^{-1}$), equivalent to 0 to 3.6% (average of $0.7 \pm 1.1\%$) of ρNO_3^- , and increased rapidly
559 below Z_{eu} (Figure 7). The highest euphotic zone rates were observed at WG1 (depth-specific average of 6.3 ± 5.0
560 nM d^{-1} , integrated average of $113.6 \pm 4.3 \mu\text{mol m}^{-2} \text{d}^{-1}$), while the lowest rates occurred at the AP (depth-specific
561 average of $0.0 \pm 0.04 \text{ nM d}^{-1}$, integrated average of $0.8 \pm 0.7 \mu\text{mol m}^{-2} \text{d}^{-1}$).

562

563 3.3.4. f-ratio estimates

564 At the stations where urea uptake was measured (LCIS stations and WG1; 11 out of 19 stations; Figure 6; Table
565 2), purea accounted for $8 \pm 6\%$ of total N uptake (i.e., $\rho\text{NO}_3^- + \rho\text{NH}_4^+ + \text{purea}$). Excluding urea uptake when
566 calculating the f-ratio would therefore overestimate the fraction of potentially exportable carbon by $\sim 8\%$. We thus
567 estimated urea uptake at the stations where it was not measured as:

568

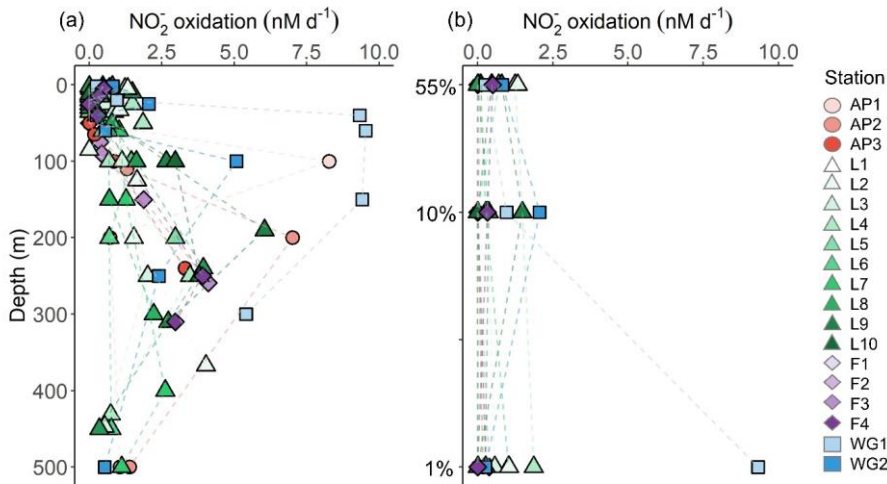
$$569 \text{ purea} = (\rho\text{NO}_3^- + \rho\text{NH}_4^+) \times 0.08 \quad (7)$$

570

571 Equation 7 may overestimate urea uptake at some of the stations, particularly where low urea concentrations were
572 measured. Theoretically, purea can also be estimated by assuming that total N uptake should equal $\text{NPP}/6.63$,
573 such that any difference between $\rho\text{NO}_3^- + \rho\text{NH}_4^+$ and $\text{NPP}/6.63$ is due to urea uptake. However, this approach

574 underestimated urea uptake at all the stations where purea was directly measured, probably because the use of a
 575 C:N ratio of 6.63:1 assumes balanced phytoplankton growth. We therefore chose to use equation 7 to estimate
 576 urea uptake for the stations lacking purea measurements as this approach will yield a more conservative (i.e.,
 577 lower) estimate of the fraction of potentially exportable carbon (section S3 in the Supplemental Information for
 578 more details). Figure 8 shows how including urea uptake affects the f-ratio throughout the sample region, with the
 579 white (no urea uptake measured) and hashed bars (urea uptake measured) indicating the amount by which the f-
 580 ratio decreased when urea uptake was included (i.e., equation 4b versus equation 4a).

581
 582 The euphotic zone-integrated f-ratios were highest at FIS in early summer (average $f\text{-ratio}_{(\text{excluding urea})}$ of $0.79 \pm$
 583 0.1 and $f\text{-ratio}_{(\text{including urea})}$ of 0.73 ± 0.09) and lowest at LCIS (average $f\text{-ratio}_{(\text{excluding urea})}$ of 0.50 ± 0.09 and $f\text{-ratio}_{(\text{including urea})}$
 584 of 0.47 ± 0.08) (Figure 8; Table 2). The variability in the f-ratios among stations appears to be
 585 largely related to the availability of NH_4^+ . For example, at FIS in early summer there was no detectable NH_4^+
 586 available to the phytoplankton and the highest f-ratios were observed (average $f\text{-ratio}_{(\text{excluding urea})}$ of 0.82 ± 0.08
 587 and $f\text{-ratio}_{(\text{including urea})}$ of 0.76 ± 0.07), while in late summer, NH_4^+ concentrations were elevated ($0.2 \pm 0.1 \mu\text{M}$)
 588 and the f-ratio declined ($f\text{-ratio}_{(\text{excluding urea})}$ of 0.68 ± 0.16 and $f\text{-ratio}_{(\text{including urea})}$ of 0.63 ± 0.15).



589
 590 **Figure 7.** Depth profiles of NO_2^- oxidation rates measured at each station (a) between the surface and 500 m, and
 591 (b) within the euphotic zone.
 592
 593
 594
 595
 596

597
598
599
600
601
602
603
604
605
606
607
608
609
610
611
612
613
614
615
616
617
618

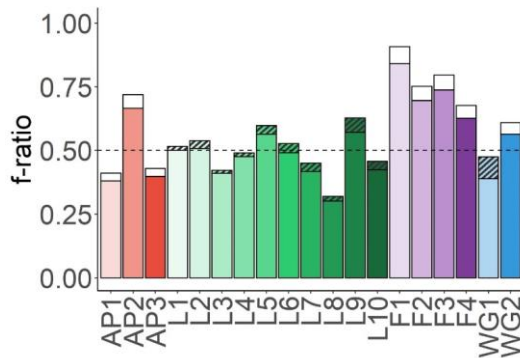


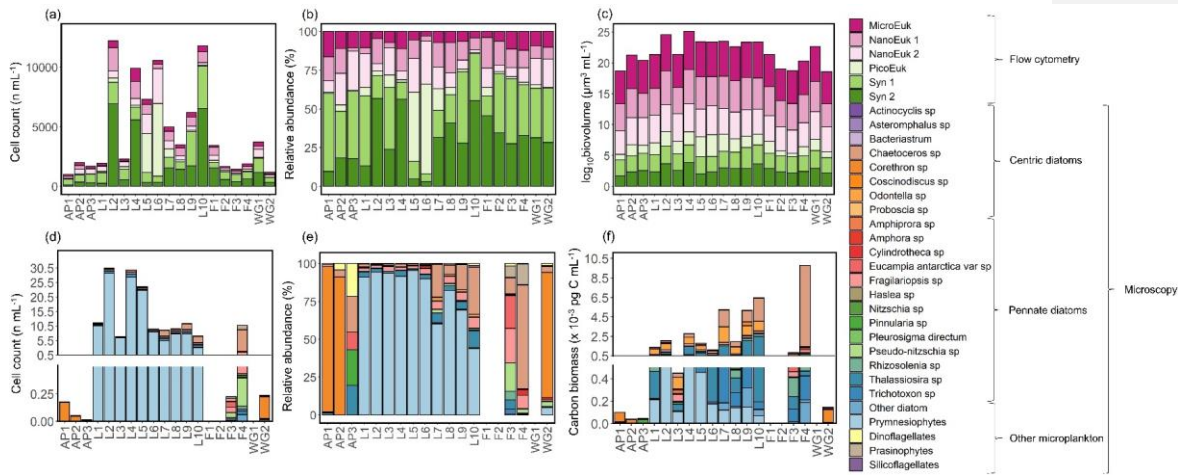
Figure 8. Euphotic zone-integrated f-ratios estimated for each station. The black-hashed and white bars show the difference between the $f\text{-ratio}_{(\text{excluding urea})}$ (higher value; equation 4a) and the $f\text{-ratio}_{(\text{including urea})}$ (lower value; equation 4b), with the black-hashed bars indicating the stations where urea uptake was measured and the white bars where it was estimated (see text for details).

619 3.3.5. Phytoplankton community composition

620 The flow cytometry data show that the phytoplankton community was numerically dominated by picoplankton at
621 all stations, with *Synechococcus* emerging as the most abundant group ($59 \pm 19\%$ of the total phytoplankton cells
622 counted), except at stations L5 and L6 where picoeukaryotes were dominant ($51 \pm 1\%$; Figure 9a-b). The
623 microeukaryotes were the least abundant group at all stations (average abundance across the sampling region of
624 $8 \pm 3\%$); however, due to their large biovolume, they contributed most to the biomass ($80 \pm 7\%$; Figure 9c). In
625 the configuration used here, flow cytometry is best suited for enumerating small cells ($<15 \mu\text{m}$; Dubelaar and
626 Jonker 2000), such that the larger microplankton present at the time of sampling were likely underestimated via
627 this technique. We thus take the phytoplankton net collections as more representative of the microplankton
628 community and colonial nanoplankton groups.

629
630 From the samples collected using the phytoplankton net (i.e., single cells or colonies $>55 \mu\text{m}$), the dominant
631 phytoplankton species at LCIS was the prymnesiophyte, *P. antarctica* ($83 \pm 17\%$ of the total phytoplankton cells
632 counted), while the phytoplankton community at the other stations was dominated by diatoms (mainly *Corethron*
633 *pennatum*, *Chaetoceros* spp. (six species), *Cylindrotheca closterium*, *Fragilariopsis ritscheri*, *Fragilariopsis*
634 *curta*, *Fragilariopsis kerguelensis*, *Fragilariopsis rhombica*, *Leptocylindrus mediterraneus*, *Odontella weisflogii*,
635 *Pseudo-nitzschia alanata* and several *Thalassiosira* spp., constituting $92 \pm 6\%$ of the phytoplankton cells counted;
636 Figure 9d-e). At LCIS, the stations sampled earlier in the season tended to be dominated by *P. antarctica* (e.g.,
637 station L3) while those sampled later hosted a more diatom-dominated community (e.g., station L8). In addition,
638 the resident diatoms at LCIS (mainly *F. ritscheri*, *O. weisflogii*, and *Thalassiosira* spp.) were much larger than
639 the numerically dominant *P. antarctica*. For example, at station L8, the 32 diatom species present ($1.6 \text{ cells mL}^{-1}$
640 1) contributed $1.80 \times 10^{-3} \text{ pg C mL}^{-1}$ (Leblanc et al., 2012) compared to $0.14 \times 10^{-3} \text{ pg C mL}^{-1}$ resulting from the
641 $7.8 \text{ cells mL}^{-1}$ of *P. antarctica* (Mathot et al. 2000). The LCIS stations with the highest relative abundance of
642 diatoms (e.g., station L8) were characterized by some of the highest rates of ρNO_3^- and greatest extent of NO_3^-
643 depletion. More broadly, the LCIS stations with the lowest sea surface temperatures (SSTs) and nutrient uptake

644 rates (i.e., stations L1 and L3) had the lowest phytoplankton counts, while those with the highest SSTs and nutrient
 645 uptake rates (i.e., station L5 and L7) had the highest phytoplankton counts (Figure 9a and d; Table 1).
 646



647 **Figure 9.** The (a, d) cell counts, (b, e) relative cell abundances, (c) log-transformed biovolume, and (f) carbon
 648 biomass of all phytoplankton groups identified from (a-c) surface flow cytometry samples and (d-f) plankton net-
 649 tow samples. The stations are labelled on the x-axis. Where there are no bars in panels (d), (e), and (f), no data are
 650 available. Carbon biomass estimates in panel (f) are shown only for the prymnesiophyte, *P. antarctica*, and the
 651 diatom species.
 652

653

Table 1. Euphotic zone-averaged N nutrient concentrations, nutrient depletions, and nutrient depletion ratios at each station occupied in the Weddell Sea in January/February 2019. Values shown are averages \pm 1 SD ($n \geq 2$), with error propagated according to standard statistical practices where appropriate. “-” indicates no available data.

Station position	Station	Sampling date	Bottom depth (m)	MLD (m)	Z_{eq} (m)	NH_4^+ (μ M)	Urea-N (μ M)	NO_3^- (μ M)	NO_3^- depletion (μ M)	$Si(OH)_4$ depletion (μ M)	PO_4^{3-} depletion (μ M)	$Si(OH)_4:NO_3^-$ depletion (μ M: μ M)	$NO_3^-:PO_4^{3-}$ depletion (μ M: μ M)
FIS Average	FIS		206 \pm 83	82 \pm 51	79 \pm 28	0.1 \pm 0.1	0.1 \pm 0.1	25.0 \pm 2.8	0.7 \pm 1.4	1.6 \pm 3.0	0.1 \pm 0.1	2.0 \pm 1.1	26.4 \pm 19.8
Fimbul	F1	01/01/19	130	135	100	0.0 \pm 0.0	-	26.4 \pm 0.5	0.2 \pm 0.5	0.5 \pm 1.6	0.0 \pm 0.0	3.2 \pm 3.9	-
Fimbul	F2	02/01/19	140	110	100	0.0 \pm 0.0	-	26.5 \pm 0.1	0.1 \pm 0.1	0.0 \pm 0.1	0.0 \pm 0.0	0.5 \pm 2.1	48.6 \pm 11.5
Fimbul	F3	03/01/19	281	63	75	0.0 \pm 0.0	0.0 \pm 0.0	26.0 \pm 0.3	0.7 \pm 0.3	1.2 \pm 0.5	0.0 \pm 0.0	1.8 \pm 0.6	18.8 \pm 1.1
Fimbul	F4	20/02/19	274	20	40	0.2 \pm 0.2	0.2 \pm 0.1	20.2 \pm 1.9	3.7 \pm 2.0	8.7 \pm 0.6	0.3 \pm 0.1	2.3 \pm 0.5	11.7 \pm 0.6
AP Average	AP		1451 \pm 847	23 \pm 8	45 \pm 9	0.8 \pm 0.2	0.3 \pm 0.1	24.9 \pm 0.6	2.5 \pm 1.7	1.1 \pm 0.8	0.1 \pm 0.1	0.6 \pm 0.2	19.8 \pm 16.5
Antarctic Peninsula	AP1	09/01/19	2155	23	35	0.6 \pm 0.1	0.2 \pm 0.1	25.6 \pm 1.4	2.6 \pm 0.7	1.4 \pm 0.4	0.2 \pm 0.1	0.5 \pm 0.4	14.1 \pm 0.4
Antarctic Peninsula	AP2	09/01/19	1686	30	50	0.7 \pm 0.1	0.2 \pm 0.1	25.9 \pm 1.0	1.0 \pm 1.1	0.8 \pm 0.2	0.1 \pm 0.0	0.8 \pm 1.1	6.8 \pm 1.1
Antarctic Peninsula	AP3	09/01/19	511	15	50	1.1 \pm 0.0	0.3 \pm 0.1	24.7 \pm 0.3	3.2 \pm 2.5	1.4 \pm 1.5	0.1 \pm 0.1	0.4 \pm 1.4	38.4 \pm 1.2
LCIS Average	LCIS		434 \pm 62	14 \pm 6	29 \pm 9	0.7 \pm 0.4	0.2 \pm 0.1	16.4 \pm 4.7	8.2 \pm 4.9	8.1 \pm 4.9	0.6 \pm 0.3	1.0 \pm 0.2	14.7 \pm 2.9
Larsen C	L1	22/01/19	376	8.5	33	1.3 \pm 0.1	0.4 \pm 0.1	21.8 \pm 0.1	2.0 \pm 0.1	2.3 \pm 0.3	0.2 \pm 0.1	1.2 \pm 0.1	11.2 \pm 0.3
Larsen C	L2	20/01/19	451	14	25	0.4 \pm 0.3	0.2 \pm 0.2	13.7 \pm 5.0	8.6 \pm 4.8	7.8 \pm 4.7	0.6 \pm 0.4	0.9 \pm 0.8	15.2 \pm 1.0
Larsen C	L3	11/01/19	431	7	50	0.9 \pm 0.1	0.2 \pm 0.1	23.1 \pm 0.2	2.2 \pm 0.1	1.3 \pm 0.8	0.1 \pm 0.1	0.6 \pm 0.6	17.7 \pm 0.3
Larsen C	L4	14/01/19	368	24	22	0.5 \pm 0.5	0.1 \pm 0.1	12.1 \pm 2.5	12.8 \pm 2.1	10.9 \pm 2.2	0.9 \pm 0.2	0.9 \pm 0.3	13.9 \pm 0.2
Larsen C	L5	15/01/19	451	10	25	0.1 \pm 0.0	0.4 \pm 0.2	12.0 \pm 1.9	10.9 \pm 2.3	9.6 \pm 1.7	0.8 \pm 0.1	0.9 \pm 0.3	13.7 \pm 0.2
Larsen C	L6	13/01/19	475	17.5	30	0.7 \pm 0.5	0.2 \pm 0.1	15.1 \pm 2.1	8.4 \pm 2.1	8.0 \pm 1.9	0.4 \pm 0.1	1.0 \pm 0.3	20.4 \pm 0.3
Larsen C	L7	22/01/19	506	8.5	25	1.0 \pm 1.1	0.2 \pm 0.1	14.7 \pm 4.1	11.1 \pm 1.8	13.5 \pm 3.4	0.8 \pm 0.2	1.2 \pm 0.3	14.8 \pm 0.3
Larsen C	L8	23/01/19	450	22.5	35	0.3 \pm 0.0	0.2 \pm 0.0	12.2 \pm 2.2	12.9 \pm 4.5	12.4 \pm 3.2	0.8 \pm 0.3	1.0 \pm 0.4	16.0 \pm 0.5
Larsen C	L9	19/01/19	318	12.5	20	0.5 \pm 0.4	0.2 \pm 0.1	20.2 \pm 4.3	5.8 \pm 3.3	6.6 \pm 5.1	0.5 \pm 0.3	1.1 \pm 1.0	11.0 \pm 0.9
Larsen C	L10	24/01/19	510	14	20	0.7 \pm 0.3	0.2 \pm 0.1	18.2 \pm 5.4	8.7 \pm 3.7	10.6 \pm 4.9	0.7 \pm 0.3	1.2 \pm 0.6	13.0 \pm 0.6
WG Average	WG		3565 \pm 379	20 \pm 0	90 \pm 14	0.2 \pm 0.2	0.1 \pm 0.1	28.8 \pm 2.4	0.4 \pm 0.3	2.0 \pm 0.9	0.1 \pm 0.0	5.6 \pm 0.7	4.1 \pm 0.6
Weddell Gyre	WG1	14/02/19	3297	20	100	0.2 \pm 0.2	0.1 \pm 0.1	26.7 \pm 0.5	0.4 \pm 0.3	2.3 \pm 0.8	0.1 \pm 0.0	5.1 \pm 0.7	4.5 \pm 0.7
Weddell Gyre	WG2	15/02/19	3833	20	80	0.4 \pm 0.1	0.1 \pm 0.1	30.2 \pm 0.8	0.3 \pm 0.4	2.0 \pm 1.0	0.1 \pm 0.1	6.1 \pm 1.3	3.7 \pm 1.5

Table 2. Euphotic zone-integrated and averaged rates at each station occupied in the Weddell Sea in January/February 2019. Values shown are averages \pm 1 SD ($n \geq 2$), with error propagated according to standard statistical practices where appropriate. “-” indicates no available data. The values shown in italics (i.e., purea) were estimated rather than measured (see text for details).

Station position	Station	[POC] (μM)	[PON] (μM)	C:N ratio	NPP ($\text{mmol m}^{-2} \text{d}^{-1}$)	ρNO_3^- ($\text{mmol m}^{-2} \text{d}^{-1}$)	ρNH_4^+ ($\text{mmol m}^{-2} \text{d}^{-1}$)	purea ($\text{mmol m}^{-2} \text{d}^{-1}$)	$V\text{NO}_3^-$ ($\mu\text{mol m}^{-2} \text{d}^{-1}$)	f-ratio _(excluding area)	f-ratio _(including area)
<i>FIS Average</i>	FIS	8.0 \pm 8.4	0.8 \pm 0.9	16.5 \pm 8.8	27.5 \pm 26.6	3.7 \pm 1.0	0.8 \pm 0.4	0.5 \pm 0.4	5.2 \pm 0.7	0.80 \pm 0.10	0.73 \pm 0.09
Fimbul	F1	5.9 \pm 2.0	0.3 \pm 0.2	21.6 \pm 3.7	4.9 \pm 0.0	3.8 \pm 0.0	0.4 \pm 0.0	<i>0.3 \pm 0.0</i>	-	0.91	0.84
Fimbul	F2	4.9 \pm 3.4	0.2 \pm 0.0	26.3 \pm 12.6	20.8 \pm 0.2	2.4 \pm 0.0	0.8 \pm 0.0	<i>0.07 \pm 0.0</i>	-	0.75	0.70
Fimbul	F3	3.1 \pm 1.8	0.4 \pm 0.2	8.8 \pm 3.0	56.9 \pm 0.6	4.8 \pm 0.1	1.2 \pm 0.0	<i>0.5 \pm 0.0</i>	4.7 \pm 1.6	0.80	0.74
Fimbul	F4	17.9 \pm 7.2	2.1 \pm 0.6	9.4 \pm 0.5	28.3 \pm 0.4	3.9 \pm 0.0	1.9 \pm 0.0	<i>0.9 \pm 0.0</i>	5.7 \pm 1.7	0.68	0.63
AP Average	AP	8.7 \pm 6.3	1.1 \pm 0.3	8.3 \pm 2.5	26.6 \pm 33.5	3.4 \pm 1.4	3.8 \pm 2.0	0.5 \pm 0.2	0.8 \pm 0.7	0.52 \pm 0.17	0.48 \pm 0.16
Antarctic Peninsula	AP1	7.4 \pm 0.7	1.3 \pm 0.1	6.1 \pm 1.4	3.1 \pm 0.1	1.8 \pm 0.1	2.6 \pm 0.0	<i>0.4 \pm 0.0</i>	0.0 \pm 3.3	0.41	0.38
Antarctic Peninsula	AP2	4.3 \pm 3.5	0.8 \pm 0.3	7.8 \pm 2.7	11.8 \pm 0.2	4.0 \pm 0.2	2.1 \pm 0.0	<i>0.4 \pm 0.0</i>	1.0 \pm 2.7	0.72	0.67
Antarctic Peninsula	AP3	14.4 \pm 5.2	1.3 \pm 0.2	11.0 \pm 2.1	65.0 \pm 0.1	4.4 \pm 0.0	5.8 \pm 0.0	<i>0.8 \pm 0.0</i>	1.3 \pm 1.3	0.43	0.40
LCIS Average	LCIS	18.8 \pm 22.1	2.4 \pm 0.8	7.4 \pm 1.9	28.6 \pm 21.3	2.2 \pm 1.1	2.6 \pm 1.3	0.6 \pm 0.3	17.3 \pm 20.6	0.50 \pm 0.09	0.47 \pm 0.08
Larsen C	L1	16.9 \pm 5.9	1.5 \pm 0.3	10.0 \pm 3.4	2.2 \pm 0.1	1.5 \pm 0.0	1.4 \pm 0.0	<i>0.2 \pm 0.0</i>	16.7 \pm 0.7	0.52	0.50
Larsen C	L2	21.2 \pm 7.1	3.1 \pm 0.5	6.3 \pm 1.7	47.8 \pm 0.5	1.5 \pm 0.1	3.3 \pm 0.0	<i>0.8 \pm 0.0</i>	9.4 \pm 0.6	0.54	0.51
Larsen C	L3	5.9 \pm 0.1	2.6 \pm 0.8	5.8 \pm 1.4	32.0 \pm 0.1	2.5 \pm 0.0	3.3 \pm 0.0	<i>0.3 \pm 0.0</i>	-	0.42	0.41
Larsen C	L4	25.1 \pm 4.7	1.0 \pm 0.2	8.0 \pm 0.5	32.2 \pm 1.0	1.9 \pm 0.1	2.1 \pm 0.0	<i>0.2 \pm 0.0</i>	69.0 \pm 1.0	0.49	0.48
Larsen C	L5	17.3 \pm 6.3	3.1 \pm 0.6	7.4 \pm 1.9	61.0 \pm 0.7	4.7 \pm 0.0	3.1 \pm 0.0	<i>0.9 \pm 0.0</i>	7.0 \pm 0.5	0.60	0.56
Larsen C	L6	10.0 \pm 1.3	2.4 \pm 0.5	9.2 \pm 5.3	25.9 \pm 1.5	2.4 \pm 0.1	2.2 \pm 0.1	<i>0.7 \pm 0.0</i>	23.0 \pm 0.9	0.53	0.49
Larsen C	L7	27.1 \pm 10.3	1.5 \pm 0.7	8.2 \pm 1.1	55.9 \pm 1.0	3.1 \pm 0.0	3.8 \pm 0.1	<i>1.1 \pm 0.0</i>	0.2 \pm 0.9	0.45	0.42
Larsen C	L8	23.5 \pm 3.3	3.3 \pm 0.3	8.2 \pm 1.3	17.3 \pm 0.4	2.3 \pm 0.0	4.8 \pm 0.1	<i>0.9 \pm 0.0</i>	8.7 \pm 1.5	0.32	0.30
Larsen C	L9	17.1 \pm 1.6	2.9 \pm 0.2	3.4 \pm 4.1	9.7 \pm 1.3	2.0 \pm 0.1	1.2 \pm 0.0	<i>0.6 \pm 0.0</i>	16.5 \pm 2.3	0.63	0.57
Larsen C	L10	23.6 \pm 14.9	2.7 \pm 1.1	7.1 \pm 0.4	1.8 \pm 0.0	0.5 \pm 0.0	0.6 \pm 0.0	<i>0.2 \pm 0.0</i>	5.2 \pm 1.6	0.46	0.42
WG Average	WG	8.0 \pm 8.9	0.7 \pm 0.3	12.3 \pm 1.8	31.6 \pm 31.3	3.2 \pm 0.1	2.0 \pm 0.2	0.5 \pm 0.1	81.9 \pm 44.7	0.54 \pm 0.10	0.48 \pm 0.12
Weddell Gyre	WG1	5.8 \pm 4.0	0.5 \pm 0.2	13.6 \pm 7.7	53.7 \pm 0.2	3.3 \pm 0.0	2.1 \pm 0.0	<i>0.6 \pm 0.0</i>	113.6 \pm 4.3	0.47	0.39
Weddell Gyre	WG2	10.1 \pm 7.9	0.9 \pm 0.3	11.0 \pm 7.5	9.5 \pm 0.4	3.1 \pm 0.0	1.8 \pm 0.0	<i>0.4 \pm 0.0</i>	50.3 \pm 1.8	0.61	0.56

656 **4. Discussion**

657 For the regions of the Weddell Sea that we sampled in summer 2019, the euphotic zone-integrated rates of NPP
658 and N uptake were generally lower at the OOOZ stations than the CCSZ stations, with the highest depth-specific
659 uptake rates observed in surface waters at LCIS (Figure 6a-d; Table 2). The few studies that have previously
660 measured summertime rates of NPP and N uptake in the Weddell Sea report similar results, with rates in the
661 marginal ice zone (MIZ) and CCSZ that were up to five-times higher than in the OOOZ (El-Sayed and Taguchi,
662 1981; Smith and Nelson, 1990; Park et al., 1999). The summertime CCSZ of the Weddell Sea can thus be broadly
663 characterised as a highly productive region with elevated biomass accumulation driven by increased water-column
664 stratification and iron-replete conditions, both the result of sea-ice melt (Semeneh et al., 1998; Lannuzel et al.,
665 2008; Klunder et al., 2011). That said, we observed considerable variability in the biogeochemical rates measured
666 in each region of the Weddell Sea, particularly at LCIS; we examine the possible drivers of and controls on the
667 inter- and intra-regional differences below.

668

669 **4.1. Drivers of NPP and N uptake in the Weddell Sea**

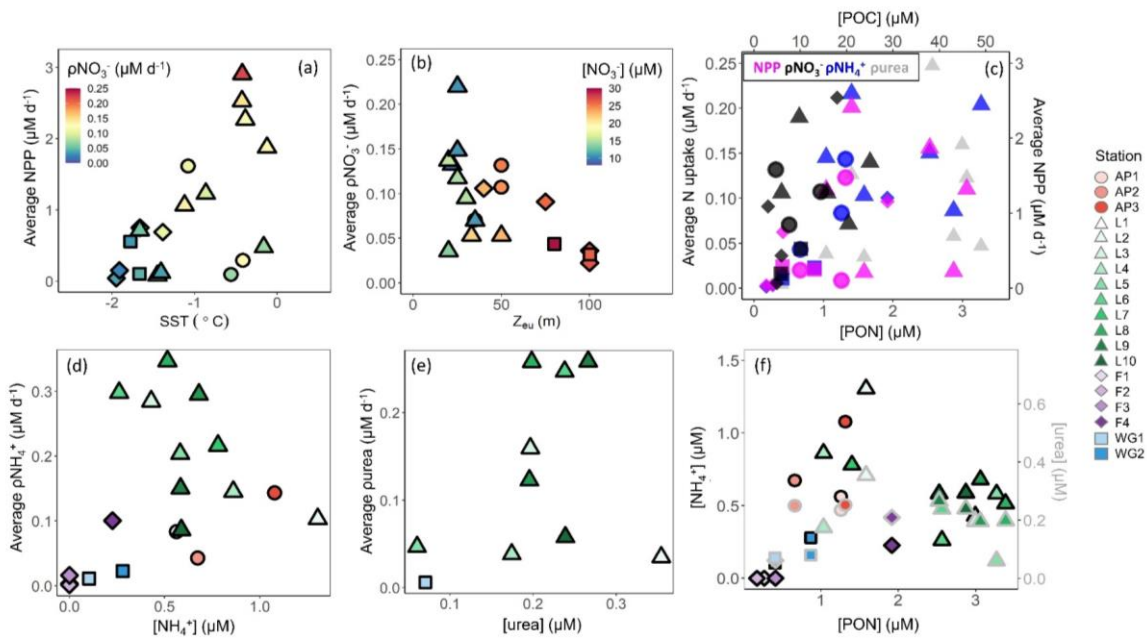
670 *Light and water column stability:* Surface waters throughout the study region were generally well stratified, with
671 MLDs ranging from 7 to 30 m, except at the early-summer FIS stations where the MLD ranged from 63 to 135 m
672 (Table 1). These deep MLDs coincided with elevated sea-ice concentrations, while the shallowest MLDs at LCIS
673 occurred in relatively ice-free waters (Table 1). Average euphotic zone rates of [NPP typically increased with](#)
674 [increasing SST and POC concentration \(Figure 10a and c\), implicating water column stratification and biomass](#)
675 [\(which affects light penetration in addition to carbon production rate\) as controls on NPP. By contrast, average](#)
676 [euphotic zone rates of \$\rho\text{NO}_3^-\$ generally varied with MLD and \$Z_{\text{eu}}\$. NPP and \$\rho\text{NO}_3^-\$ generally varied with the depth](#)
677 [of the mixed layer and \$Z_{\text{eu}}\$ at all stations—](#) they were highest (lowest) at the stations where Z_{eu} was shallowest
678 (deepest) (Figure 10a-b)—implicating light as a major control on NPP and ρNO_3^- . At LCIS, however, the euphotic
679 zone was shallow at all stations (<50 m, with an average Z_{eu} of 28.5 ± 9 m), yet NPP and ρNO_3^- varied by over an
680 order of magnitude (Table 2). Here, we observed a positive relationship between the LCIS rates and SST, with
681 NPP and ρNO_3^- increasing at higher SSTs, the latter likely due to indicative of increased water column stratification
682 (Figures 10a and S4bd; see below).

683

684 Throughout the sampling region, the average euphotic zone rates of ρNH_4^+ and p_{urea} also varied with Z_{eu} (Figure
685 10c), suggesting that these processes were light dependent too, which could be taken to indicate that these
686 processes were also light dependent. However, such a finding would be unexpected, as the energy requirement
687 associated with NH_4^+ and urea assimilation is low (El-Sayed and Taguchi 1981; Dortch 1990; Priddle et al. 1998).
688 The observed relationship is more likely due to the *in situ* biomass, which i) attenuates light and ii) provides a
689 source of organic matter for the production of NH_4^+ and dissolved organic N, including urea. Indeed, the stations
690 with the deepest Z_{eu} were characterized by low concentrations of particulate organic matter and regenerated N
691 (Figures 3a-b and 5), leading us to conclude that ρNH_4^+ and p_{urea} were predominantly controlled by the
692 availability of regenerated N (Figures 10d-e and S3b; section S4 in the Supplemental Information). This
693 conclusion is supported by the positive relationship observed between ρNH_4^+ or p_{urea} and the coincident NH_4^+ or
694 urea concentrations (Figure 10d-e). Increase in ρNH_4^+ and p_{urea} towards the base of the euphotic zone at stations
695 with elevated regenerated N concentrations (e.g., station L8; Figures 6c-d, g-h, and k-l, and 10e).

696

697 The lowest regenerated N concentrations occurred at the stations with the lowest rates of NPP and ρNO_3^- , and the
 698 highest NO_3^- concentrations (e.g., station F1). This is probably because NH_4^+ and urea tend to accumulate only
 699 when biomass (and productivity) is sufficiently high to support elevated rates of heterotrophic activity (Semeneh
 700 et al., 1998). At the stations with low POC and PON concentrations, remineralisation rates were likely also low,
 701 limiting the flux of NH_4^+ and urea (Figure 10f) and driving low rates of ρNH_4^+ and purea (Figure 10d-e). At the
 702 stations where NH_4^+ and urea concentrations were elevated, rates of ρNH_4^+ and purea increased with depth, along
 703 with a decrease in NPP and ρNO_3^- (e.g., station L8). These observations further demonstrate the control of biomass
 704 on NPP, light on NPP and ρNO_3^- , and substrate availability on ρNH_4^+ and purea. That said, it is unlikely that the
 705 variability in NPP and N uptake among the stations was driven by biomass, light, and nutrient availability alone,
 706 and we hypothesize that hydrography, iron availability, and phytoplankton community composition also played a
 707 role.



708 **Figure 10.** Euphotic zone-averaged rates of (a) NPP versus SST, (b) ρNO_3^- versus euphotic zone depth (Z_{eu}), (c)
 709 N uptake (left y-axis) versus PON (bottom x-axis) and NPP (right y-axis) versus POC (top x-axis), (d) ρNH_4^+
 710 versus NH_4^+ concentration, and (e) purea versus urea concentration, as well as (f) the concentrations of NH_4^+
 711 (black outlined symbols; left y-axis) and urea (grey outlined symbols; right y-axis) versus PON at each station.
 712 The symbols in panel (a) are coloured by ρNO_3^- , in panel (b) by NO_3^- , in panel (c) by NPP
 713 (pink), ρNO_3^- (black), ρNH_4^+ (blue), and purea (grey).
 714

715 At LCIS, the stations closest to the ice shelf were characterised by low SSTs and low rates of NPP and N uptake
 716 (stations L1 and L3; Figures 1, S4 and S5a and 11a; Table 2). The low SSTs can be attributed either to the
 717 formation of sea-ice or to the upwelling of WW along the ice shelf. Sea-ice formation, in addition to decreasing

718 SST, also increases the salinity of ASW due to brine rejection (Gill 1973). While the salinity of ASW at the low-
719 SST stations was indeed elevated, the oxygen concentrations were relatively low ($\leq 300 \mu\text{M}$, which is below
720 saturation; Figure [S5b-d4e and d](#)). In surface waters and sea-ice, oxygen is typically saturated as it rapidly
721 equilibrates with the atmosphere (Gleitz et al., 1995) [and is produced by photosynthesizing phytoplankton and](#)
722 [sea-ice algae](#). Sea-ice formation should not, therefore, drive a ~~notable change~~decrease in the oxygen content of
723 ASW. The low oxygen concentrations at stations L1 and L3 were contiguous with those in the underlying WW
724 (Figure [S5d4d](#)), leading us to conclude that the cool, saline waters along the ice-shelf ~~front~~ indicate recent
725 upwelling of WW. Such upwelling could temporarily inhibit productivity by decreasing the stability of the water
726 column and mixing phytoplankton below the euphotic zone. This mechanism can explain the low uptake rates and
727 weak nutrient depletions observed at the low-SST stations.

728
729 Relatively cold, saline surface waters have previously been observed at the ice-edge off Larsen A and B Ice
730 Shelves and shown to hinder NPP (Cape et al., 2014). In that case, the dense surface waters were surmised to
731 result either from offshore wind stress at the inshore region that induced localised mixing, or from the advection
732 of surface waters offshore by coastal upwelling. Both mechanisms would decrease water column stability, and by
733 extension, productivity. Cape et al. (2014) observed an increase in NPP with distance from the coast at Larsen A
734 and B, a trend that we did not observe, likely because of the proximity of our LCIS stations to the ice shelf (within
735 75 km for all stations). Instead, our rates of NPP and N uptake were positively coupled with SST at the ice-edge
736 (Figures [S4 and S5-40d](#)). We propose that surface SST at LCIS can be used as an indicator of water-mass age,
737 with cooler SSTs indicating newly-upwelled WW and warmer SSTs designating older surface waters that have
738 had time to absorb heat from the atmosphere. The higher rates of NPP and N uptake in the warmer surface waters
739 occur because phytoplankton experience favourable growing conditions for an extended period, resulting in
740 biomass accumulation. By contrast, persistent localised upwelling along LCIS inhibits productivity in the adjacent
741 surface waters, with implications for the spatial distribution of biomass and [the potential for](#) organic carbon export.

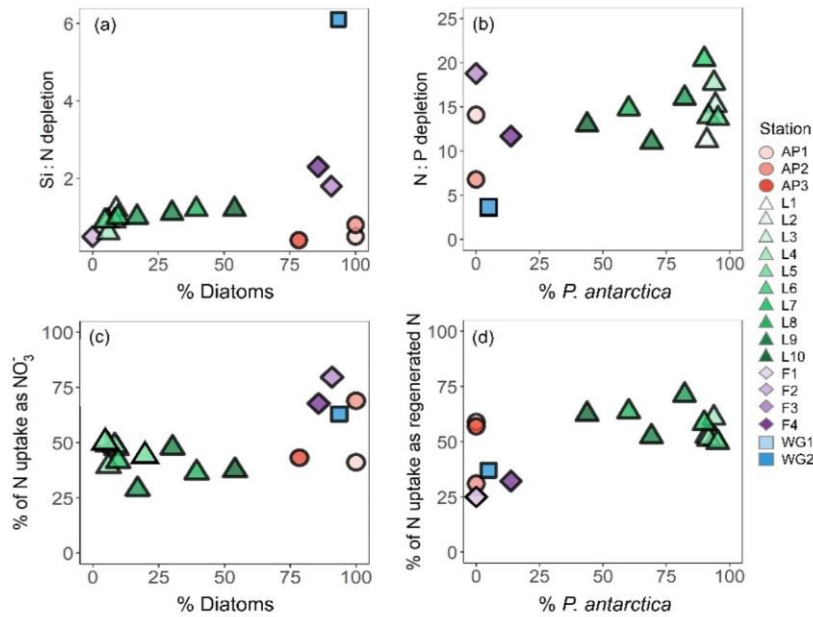
742
743 *Nutrient and [inferred iron conditions in Weddell Sea surface waters](#)*: Across our sampling region, ASW was
744 depleted in NO_3^- , Si(OH)_4 , and PO_4^{3-} relative to the underlying WW, with the greatest nutrient depletion occurring
745 at LCIS and at FIS in late summer (Figure 4a-c). [Because diatoms and/or *P. antarctica* were the dominant](#)
746 [phytoplankton at all stations \(Figure 9d-f\), we can use the Si:N:P depletion ratios \(here used as shorthand for the](#)
747 [Si\(OH\)₄:NO₃⁻:PO₄³⁻ depletion ratios\) to assess the iron conditions and N nutrition of these two phytoplankton](#)
748 [groups](#). Under iron-replete conditions, diatoms consume Si:N:P in an approximate ratio of 1:1:0.07 (Ragueneau
749 et al. 2000; Hutchins and Bruland 1998; Takeda 1998; Mosseri et al. 2008), while under iron-limitation, they
750 increase their uptake of Si and decrease that of P relative to N, consuming nutrients in a ratio of ≥ 2 :1:0.09 (Arrigo
751 et al., 1999; Finkel et al., 2006; Green and Sambrotto, 2006; Mosseri et al., 2008; Weber and Deutsch, 2010;
752 Martiny et al., 2013), with Si:N uptake ratios as high as 8:1 observed under conditions of extreme iron depletion
753 (Franck et al., 2000; Brzezinski et al., 2003). [At a first approximation](#), the Si:N:P depletion ratios estimated in our
754 study suggest that the AP and LCIS stations were characterised by iron-replete conditions (ratio of 0.9:1:0.06)
755 while phytoplankton community at the FIS and WG stations experienced iron limitation (ratios of 3.6:1:0.15;
756 Figure 4d-e; Table 1).

757

758 High iron concentrations have previously been measured in surface waters in the CCSZ and northern Weddell Sea
759 (as high as 7 nM; Lannuzel et al. 2008; De Jong et al. 2012). Iron is supplied to the mixed layer in these regions
760 via sea-ice melt, ice shelf melt, continental runoff, vertical and lateral advection, and resuspension of continental
761 shelf sediments (Lannuzel et al., 2008; De Jong et al., 2012; Klunder et al., 2014). In contrast, the central WG is
762 iron-limited as iron is supplied to surface waters mainly by wind-induced vertical mixing (Hoppema et al. 2015).
763 During our sampling, sea-ice concentrations were high at the WG stations, which would have dampened the effect
764 of wind stress on surface waters and thus hindered vertical mixing. At FIS in early summer, iron should have been
765 replete as phytoplankton would not have had sufficient time to exhaust the surface reservoir. Here, the sea-ice
766 concentrations were elevated, and the mixed layers were deep such that light, rather than iron, likely limited
767 phytoplankton growth. Indeed, light-limited diatoms have been observed to consume Si:N:P in a ratio similar to
768 that reported for conditions of iron depletion (Brzezinski, 1985). By late summer at FIS, the sea-ice had completely
769 melted, which should have further alleviated iron limitation, yet the Si:N depletion ratios were high (average of
770 2.3 ± 0.5). [These apparently high Si:N depletion ratios may be due to our not accounting for regenerated N uptake.](#)
771 [These elevated ratios may be the result of only considering \$\text{NO}_3^-\$ uptake and not accounting for regenerated N](#)
772 [consumption.](#) At FIS in late summer, NH_4^+ supported 32% of N uptake; accounting for this N source decreases
773 the Si:N depletion ratio to 1.4:1, which is closer to expectations for iron-replete diatoms. Some diatom growth
774 was likely also supported by urea, which would further decrease the Si:N depletion ratio. Additionally, it is
775 plausible that the diatoms at station F4 were beginning to experience iron-limitation as sampling occurred late in
776 the season.

777
778 Accounting for regenerated N uptake greatly alters the Si:N depletion ratios, particularly at LCIS, and provides
779 insights into the behaviour of the dominant phytoplankton groups that were active in the mixed layer, both prior
780 to and at the time of sampling. [From the Si: \$\text{NO}_3^-\$ depletion ratio at LCIS, we infer that *P. antarctica* predominantly](#)
781 [consumed regenerated sources of N. Our reasoning relies on that fact that under favourable nutrient and light](#)
782 [conditions, diatoms will rely near exclusively on \$\text{NO}_3^-\$ \(Lomas and Glibert 1999\), such that the average Si: \$\text{NO}_3^-\$](#)
783 [depletion ratio at LCIS of \$1.0 \pm 0.2\$ can be attributed entirely to this phytoplankton group. At the stations where](#)
784 [diatoms dominated the phytoplankton biomass, the Si: \$\text{NO}_3^-\$ depletion ratios were elevated and \$\rho\text{NO}_3^-\$ was high](#)
785 [\(Figure 11a and c\). In contrast, at the stations where *P. antarctica* was dominant, the Si: \$\text{NO}_3^-\$ depletion ratios were](#)
786 [low \(generally \$<1\$ \) and regenerated N uptake was high relative to the other stations \(Figure 11a and d\). Under](#)
787 [favourable nutrient and light conditions, diatoms will typically consume \$\text{NO}_3^-\$ over \$\text{NH}_4^+\$ as i\) \$\text{NO}_3^-\$ is usually](#)
788 [present in substantially higher concentrations than \$\text{NH}_4^+\$ and ii\) the lower surface area-to-volume ratio of \(larger\)](#)
789 [diatoms makes it harder for them to compete with smaller cells for a less abundant resource \(i.e., \$\text{NH}_4^+\$ \) \(Probyn](#)
790 [and Painting, 1985; Koike et al., 1986; Lomas and Glibert, 1999; Karsh et al., 2003\). The average Si: \$\text{NO}_3^-\$](#)
791 [depletion ratio of \$1.0 \pm 0.2\$ at LCIS can therefore be attributed almost entirely to diatoms.](#) When total N uptake is
792 considered, the Si:N depletion ratios decrease to 0.3 ± 0.1 , indicating the consumption of three-times more N than
793 $\text{Si}(\text{OH})_4$. We attribute this decline to regenerated N uptake by *P. antarctica*, a phytoplankton group that is known
794 to preferentially consume NH_4^+ when it is available due to the lower energy and iron requirements of NH_4^+
795 assimilation (El-Sayed and Taguchi, 1981; Dortch, 1990; Jacques, 1991; Goeyens et al., 1995; Priddle et al., 1998;
796 Stefels and Van Leeuwe, 1998). [By contrast, diatoms are \$\text{NO}_3^-\$ specialists that can outcompete other phytoplankton](#)
797 [for this N source \(Malone 1980\). They have even been observed to consume \$\text{NO}_3^-\$ under iron deplete conditions,](#)

798 which is possible due to their low iron requirement relative to that of other phytoplankton groups (Marchetti and
 799 Maldonado 2016; Marchetti and Cassar 2009).



800
 801 **Figure 11.** Scatterplots of (a) the Si:N depletion ratio (i.e., (i.e., Si(OH)₃-to-total N depletion) versus the % diatom
 802 abundance, (b) N:P depletion ratio (i.e., total N-to-PO₄³⁻ depletion) versus the % *P. antarctica* abundance, (c) %
 803 of total N (i.e., NO₃⁻ + NH₄⁺ + urea) assimilated as NO₃⁻ versus the % diatom abundance, and (d) % of total N
 804 assimilated as regenerated N (i.e., NH₄⁺ + urea) versus the % *P. antarctica* abundance at each station.
 805

806 We can also use the NO₃⁻:PO₄³⁻ depletion ratios to better understand the iron conditions and relative importance
 807 of *P. antarctica* versus diatoms in generating the observed nutrient depletion ratios. *P. antarctica* are known to
 808 consume NO₃⁻ and PO₄³⁻ in a ratio of ~20:1, while for iron-replete diatoms, this ratio is <14:1 (Arrigo et al. 1999;
 809 Smith and Asper 2001; Garcia et al. 2018). At LCIS, the NO₃⁻:PO₄³⁻ depletion ratio averaged 14.7 ± 2.9, consistent
 810 with a dominant role for iron-replete diatoms. However, variability in the NO₃⁻:PO₄³⁻ depletion ratios was
 811 observed among the LCIS stations (with ratios ranging from 11 to 20), which can be explained by local variations
 812 in phytoplankton community composition. At stations where large diatoms were dominant (e.g., L10, where
 813 diatoms contributed 6.47 x 10⁻³ pg C mL⁻¹ to biomass while *P. antarctica* only contributed 0.07 x 10⁻³ pg C mL⁻¹),
 814 the NO₃⁻:PO₄³⁻ depletion ratios were low (13.0 ± 0.6; Figure 11b). In contrast, at the stations where *P. antarctica*
 815 were numerically dominant (e.g., L6; where *P. antarctica* constituted 90% of the microphytoplankton) and
 816 contributed more to biomass (0.17 x 10⁻³ pg C mL⁻¹), elevated NO₃⁻:PO₄³⁻ depletion ratios were measured (20.4 ±
 817 0.3; Figure 11b; Table 1). Furthermore, high rates of NH₄⁺ uptake were measured at LCIS, equivalent to and at
 818 times greater than the coincident NO₃⁻ uptake rates (Figure 6; Table 2), particularly at the stations with the highest
 819 relative abundance of *P. antarctica*. *P. antarctica* has been observed to preferentially consume NH₄⁺, while
 820 diatoms will consume NO₃⁻ if iron is available (Probyn and Painting 1985; Lomas and Glibert 1999; Glibert et al.

821 ~~2016~~. In general, the relative contribution of diatoms versus *P. antarctica* therefore appears to control the nutrient
822 depletion ratios on a variety of scales in the Weddell Sea.

823

824 *Drivers of phytoplankton community composition:* Phytoplankton community composition and the variations
825 therein have implications for the biological [carbon](#) pump, both directly (diatoms sink more rapidly than smaller
826 and/or non-ballasted phytoplankton; Treguer and Jacques 1992; De Baar et al. 2005; Boyd et al. 2007) and
827 indirectly (NO_3^- consumption is quantitatively related to carbon export; Dugdale and Goering 1967; Eppley and
828 Peterson 1979). Above, we have discussed the role of phytoplankton community composition in controlling
829 productivity and upper ocean nutrient cycling. Below, we discuss the processes that may have caused *P. antarctica*
830 to dominate over diatoms at LCIS, and vice versa at the other Weddell Sea stations.

831

832 At LCIS, a coastal sensible heat polynya persisted throughout the sampling period. The opening of such polynyas
833 along the eastern AP is linked to the occurrence of warm, föhn winds that originate over the continent and blow
834 over the AP, influencing the coastal north-western Weddell Sea (Cape et al., 2014). Föhn winds drive the offshore
835 movement of sea-ice, which initiates the opening of polynyas that persist because the winds are warm, thus
836 hindering the formation of new sea-ice (Cape et al., 2014). The development of coastal sensible heat polynyas
837 results in relatively deep mixed layers and a weakly stratified water column. The polynya at LCIS opened in late
838 November, approximately two months prior to our sampling. At this time (i.e., the beginning of the growing
839 season), motile *P. antarctica* cells likely dominated the phytoplankton community as *P. antarctica* are low-light
840 specialists compared to other Antarctic phytoplankton (Goffart et al., 2000; Alderkamp et al., 2012; Delmont et
841 al., 2014). This notion is supported by the generally low phytoplankton cell counts (for both flow cytometry and
842 net-tow samples) and high relative abundance of *P. antarctica* compared to diatoms at the stations along the ice
843 shelf where WW had recently upwelled (e.g., L3; Figures 9a, d, e and S5). As the mixed layer shoaled into the
844 summer and light limitation was alleviated, a diatom bloom would have been initiated and *P. antarctica* would
845 have formed colonies (Schoemann et al., 2005) – indeed, the presence of *P. antarctica* colonies and diatom chains
846 at the time of our sampling in January is evidence that the water column was well stratified (Goffart et al. 2000).
847 As the season progressed, diatoms would have outcompeted *P. antarctica* and come to dominate the
848 phytoplankton community. At the stations sampled later in the season (e.g., L10; Figure 9e), the relative
849 abundance of diatoms versus *P. antarctica* was higher than at the stations occupied two weeks earlier (e.g., L5;
850 Figure 9e). Diatoms have a lower iron and higher light requirement than *P. antarctica* and thus tend to thrive once
851 the *P. antarctica* bloom declines, when the water column has stratified and they can access the lower
852 concentrations of residual iron (Strzepek et al., 2011). That said, iron is likely perennially high at LCIS in summer
853 as it is near-continuously supplied to surface waters by sea-ice melt and upwelling of WW along the ice shelf
854 (Klunder et al., 2014). The elevated iron concentrations would allow the diatoms to grow rapidly on the available
855 NO_3^- once the mixed layer had shoaled enough to alleviate light limitation, contributing to their capacity to
856 outcompete other phytoplankton.

857

858 At the other (non-LCIS) sampling sites, diatoms dominated the phytoplankton community. We hypothesize that
859 at the beginning of the growing season, melting sea-ice alleviated light- and, to a lesser extent, iron limitation,
860 providing favourable conditions for diatom growth. At the same time, the generally lower iron concentrations

861 characteristic of open Weddell Sea surface waters may have selected against *P. antarctica* (Strzepek et al., 2011).
862 Previous studies conducted in the Ross Sea observed large diatom blooms associated with the receding ice-edge
863 and concluded that bloom formation was favoured by the rapid stabilization of the water column from meltwater
864 inputs (Goffart et al. 2000; Sedwick et al. 2000). Regions of the Weddell Sea that undergo rapid stratification due
865 to sea-ice melt will likely also experience large diatom blooms. We thus conclude that the dominance of diatoms
866 over *P. antarctica* at the non-LCIS stations was influenced by local hydrodynamic processes that rapidly induce
867 water column stability, and increase light availability (e.g., in areas of recent sea-ice melt). By contrast, *P.*
868 *antarctica* dominates under low-light, such as in the deep mixed layers that initially characterize coastal polynyas.
869 Eventually, diatoms will succeed *P. antarctica* in these polynyas as conditions become favourable for their
870 growth.

871

872 4.2. Carbon export potential across the Weddell Sea

873 Previous *f*-ratio estimates for the summertime Weddell Sea range from 0.18 to 0.83 (Koike et al. 1986; Rönner et
874 al. 1983; Nelson et al. 1987; Smith and Nelson 1990; Goeyens 1991; Goeyens et al. 1995). Using equations 4a
875 and 4b, we calculate euphotic zone-integrated *f*-ratios that range from 0.32 to 0.91 (excluding urea uptake) and
876 0.30 to 0.84 (including urea uptake). The lowest *f*-ratios occurred at LCIS ($f\text{-ratio}_{(\text{excluding urea})} = 0.50 \pm 0.09$ and $f\text{-ratio}_{(\text{including urea})} = 0.47 \pm 0.08$) and the highest at FIS ($f\text{-ratio}_{(\text{excluding urea})} = 0.78 \pm 0.1$ and $f\text{-ratio}_{(\text{including urea})} = 0.73$
877 ± 0.09) (Figure 8; Table 2). We note that urea uptake may have been stimulated at the stations where it was
878 measured given the quantity of ^{15}N -urea added (0.1 μM) relative to the ambient urea concentrations (average of
879 $0.2 \pm 0.1 \mu\text{M}$; Figure S2; section S3 in the Supplemental Information); if so, regenerated production could be
880 overestimated at all stations since we extrapolated the average measured contribution of urea-to-total-N uptake (8
881 $\pm 6\%$) to the stations at which purea was not measured (equation 7). The *f*-ratio estimates excluding and including
882 urea uptake thus represent an upper and lower bound, respectively, on the fraction of potentially exportable carbon.
883 That said, accounting for urea uptake decreased the average *f*-ratio by very little, from 0.57 ± 0.15 to 0.52 ± 0.14 .
884
885

886 Estimates of the *f*-ratio and carbon export potential can be complicated by euphotic zone nitrification, which
887 supplies regenerated rather than new NO_3^- to phytoplankton. Failing to account for this regenerated N flux can
888 lead to an overestimation of carbon export potential (Yool et al. 2007; Mdutyana et al. 2020). At all stations, the
889 euphotic zone rates of $V_{\text{NO}_2^-}$ were low (undetectable to 9.5 nM d^{-1} , average of $0.6 \pm 1.4 \text{ nM d}^{-1}$; Figure 7b) and
890 correcting the *f*-ratio for these rates (equation 4) had a minimal effect (average decrease of $2 \pm 6\%$). The largest
891 decrease was observed at WG1 where the highest euphotic zone-integrated rates of $V_{\text{NO}_2^-}$ were measured ($f\text{-ratio}_{(\text{excluding urea})}$ decreased from 0.60 to 0.47 and $f\text{-ratio}_{(\text{including urea})}$ decreased from 0.49 to 0.39; Table 2).
892
893

894 The low rates of euphotic zone nitrification are consistent with the previous (limited) data available for the
895 summertime OOZ and CCSZ of the Southern Ocean. For example, Mdutyana et al. (2020) measured euphotic
896 zone rates of NO_2^- and NH_4^+ oxidation in summer at FIS and in the OOZ just north of the WG (56°S 0°E) that
897 were below detection. Summertime studies of euphotic zone NH_4^+ oxidation in the Ross and Scotia Seas also
898 report low rates, of 6-8.9 nM d^{-1} and 0.4-5.8 nM d^{-1} , respectively (Olson, 1981). We conclude that, as expected,
899 the high-light and generally low- NH_4^+ conditions of the summertime Weddell Sea inhibited euphotic zone
900 nitrification, and that the slow growing-nitrifiers were probably also outcompeted by phytoplankton for NH_4^+

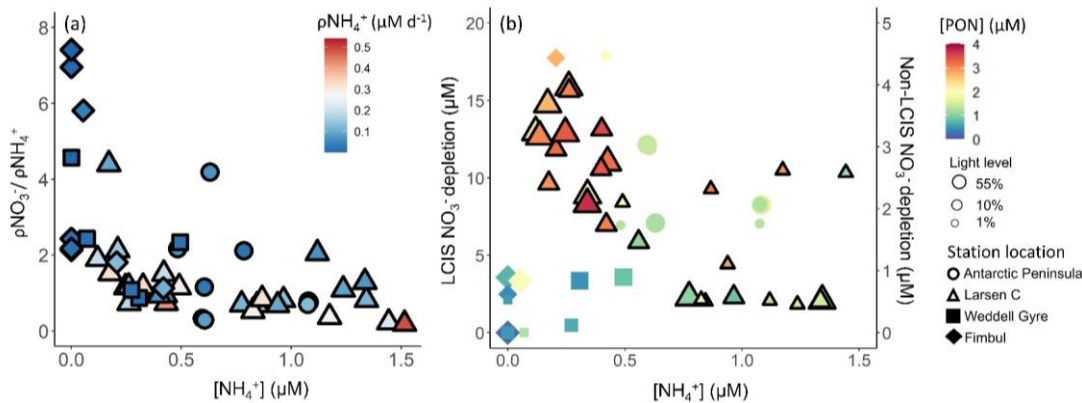
901 (Ward 1985; 2005; Smith et al. 2014; Zakem et al. 2018). Classifying NO_3^- uptake as new production and equating
902 it to carbon export [potential](#) is thus reasonable for the summertime Weddell Sea.

903
904 Although the highest f -ratios were estimated for the FIS stations, the highest rates of ρNO_3^- were observed at LCIS
905 and along the AP (Figure 8; Table 2). FIS was thus characterised by the highest carbon export potential relative
906 to NPP, while the N cycle data imply that the absolute [potential](#) carbon export flux was highest at LCIS and the
907 AP. The maximum extent of nutrient depletion was also observed at LCIS (NO_3^- depletion of 57-428 mmol m^{-2}
908 and PO_4^{3-} depletion of 5.8-18.7 mmol m^{-2}). Assuming Redfield C:N and C:P stoichiometry of 6.63:1 and 106:1,
909 respectively, the seasonal NO_3^- depletion equates to a carbon export flux of 0.4-2.8 mol C m^{-2} and the PO_4^{3-}
910 depletion to 0.6-2.0 mol C m^{-2} . Alternately, multiplying ρNO_3^- by the length of time that the coastal polynya had
911 been open (30 November until the date of sampling; Table 1) yields an estimate for net seasonal NO_3^- uptake of
912 59-428 mmol m^{-2} and carbon export flux of 0.4-2.8 mol C m^{-2} at LCIS, remarkably similar to the estimates derived
913 from seasonal NO_3^- depletion. Our estimates of carbon export potential are, however, on the low end of those
914 reported previously for the CCSZ and MIZ of the Weddell Sea (e.g., estimates for January/February range from
915 2.4-4.9 mol C m^{-2} ; R nner et al. 1983; Hoppema et al. 2000; 2007). Given the high-light and nutrient- and iron-
916 replete conditions encountered at LCIS, one might thus have expected higher f -ratios and estimates of carbon
917 export potential (i.e., NO_3^- depletion), raising the question of the possible limitations thereon.

918
919 Throughout the Weddell Sea, NH_4^+ and urea uptake were coupled with substrate availability, while NO_3^- uptake
920 was not. Instead, NO_3^- uptake appeared to vary with light (see above) and as a function of the ambient NH_4^+
921 concentration (Figure 12a). At LCIS where NH_4^+ was elevated throughout the mixed layer at all stations, NO_3^-
922 uptake and NO_3^- depletion decreased with increasing NH_4^+ (Figure 12), which we attribute to NH_4^+ inhibition of
923 NO_3^- uptake (Goeyens et al., 1995). By contrast, at the non-LCIS stations, NO_3^- depletion and ambient NH_4^+
924 concentration showed a positive relationship, consistent with NO_3^- -fuelled phytoplankton growth being followed
925 by intense remineralization and grazing, both of which can yield elevated NH_4^+ (R nner et al. 1983; El-Sayed
926 1984; Semeneh et al. 1998).

927
928 Previous studies conducted in MIZ and CCSZ of the Weddell Sea have shown that NH_4^+ concentrations $\geq 0.5 \mu\text{M}$
929 can inhibit NO_3^- uptake, particularly by diatoms, resulting in phytoplankton ([including diatoms](#)) preferentially
930 consuming NH_4^+ over NO_3^- . [For example](#), Goeyens et al. (1995) observed a Weddell Sea phytoplankton
931 community dominated by diatoms prior to NH_4^+ accumulation, but once surface waters became enriched in NH_4^+ ,
932 diatom dominance ceased. The authors concluded that diatoms were unable to bloom despite the elevated NO_3^-
933 concentrations because of the inhibitory effect of NH_4^+ , while non-siliceous, smaller phytoplankton species
934 flourished because their preferred N source is NH_4^+ . In our study, although NH_4^+ inhibition of ρNO_3^- apparently
935 occurred at LCIS (Figure 12), ρNO_3^- was on average as high as ρNH_4^+ and was never zero (Table 2) – in other
936 words, the elevated ambient NH_4^+ concentrations did not prevent NO_3^- uptake even though it appears to have
937 slowed it. We propose that the mixed community of diatoms and *P. antarctica* present at the time of our sampling
938 meant that diatoms were able to assimilate mainly NO_3^- while *P. antarctica* consumed the NH_4^+ , preventing this
939 reduced N form from accumulating to fully inhibitory concentrations. While the reliance of *P. antarctica* on NH_4^+
940 over NO_3^- represents a missed opportunity for carbon export given that these phytoplankton are known to fix up

941 to 50% more carbon than diatoms per mole of PO_4^{3-} consumed (Arrigo et al., 1999), that the diatoms were able to
 942 proliferate in the face of elevated NH_4^+ may have partly compensated for this. Earlier in the season when NH_4^+
 943 concentrations were negligible, it is likely that the f-ratios at LCIS were >0.5 and comparable to those estimated
 944 for the FIS stations, as observed at Larsen A and B in early summer (Goeyens et al., 1995; Cape et al., 2014). We
 945 conclude that elevated NH_4^+ may have weakened carbon export potential at LCIS in January/February 2019
 946 through its effect on whole-community NO_3^- uptake. Carbon export may have been further inhibited later in the
 947 season as NH_4^+ concentrations continued to increase following remineralisation of the phytoplankton bloom,
 948 coupled with the seasonal decrease in daylight that is expected to shift the phytoplankton community to
 949 proportionally higher NH_4^+ dependence (Lourey et al., 2003; Philibert et al., 2015; Glibert et al., 2016; Deary,
 950 2020; Smart et al., 2020).



951 **Figure 12.** (a) NO_3^- uptake normalised to NH_4^+ uptake as a function of NH_4^+ concentration and b) NO_3^- depletion
 952 versus NH_4^+ concentration. The symbols in panel (a) are coloured by NH_4^+ uptake rate (ρNH_4^+) and in panel (b)
 953 by PON concentration. In panel (b), the symbol size indicates the incubation light level, NO_3^- depletion at LCIS
 954 corresponds with the left y-axis, and NO_3^- depletion at all other (“non-LCIS”) stations corresponds with the right
 955 y-axis.
 956

957 4.3. Broader biogeochemical implications at LCIS

958 LCIS is a region of deep-water formation, such that the biogeochemical properties of ASW influence those of
 959 MWDW and the bottom waters. [Our data indicate significant net depletion of nutrients from ASW over the](#)
 960 [summer growing season. Over the summer growing season, there was significant net depletion of nutrients from](#)
 961 [ASW.](#) These nutrients would have been converted to organic matter that was either consumed by zooplankton or
 962 exported from the euphotic zone to be decomposed by heterotrophic bacteria, in the water column or on the shelf,
 963 [or consumed by the benthic community.](#) The subsurface remineralisation of organic matter acts to increase the
 964 CO_2 and nutrient reservoir of WW and shelf waters (ISW and HSSW; both precursors of CDW). Some portion of
 965 this CO_2 is effluxed to the atmosphere when WW upwells along the [front of the ice shelf front](#), while the remainder
 966 will be mixed into MWDW and eventually transferred to the bottom waters where it will be stored for hundreds
 967 of years (Ito et al. 2010). [Exported organic matter that escapes water-column and on-shelf remineralization settles](#)
 968 [on the seafloor where a small fraction is buried and thus removed from the ocean-atmosphere system, while the](#)
 969 [bulk of the organic matter is consumed by the benthic community and ultimately converted back to \$\text{CO}_2\$](#) (Isla et

970 al., 2006, 2011; Pineda-Metz et al., 2019). [The CO₂ and nutrients recycled by the benthos may be resupplied to](#)
971 [the surface during upwelling, whereupon remineralized CO₂ can escape to the atmosphere](#). Biological activity and
972 nutrient drawdown at LCIS, and the limitations thereon, thus affect the CO₂ and nutrient content of the bottom
973 waters, [as well as the energy supply to the benthos and the extent to which CO₂ is removed from the atmosphere](#)
974 [on climate-relevant timescales](#). The Si(OH)₄:NO₃:PO₄³⁻ ratio at depth at LCIS (average of 2:1:0.07 below 150 m)
975 implicates diatoms as the main biological driver of nutrient conditions in MWDW, and by extension the bottom
976 waters, throughout the Weddell Sea. Although the dominance of *P. antarctica* in early and mid-summer does not
977 appear to affect the nutrient properties of MWDW, it may influence its CO₂ content. *P. antarctica* consume
978 approximately twice as much carbon per mole of PO₄³⁻ as diatoms, and the colonial forms have been observed to
979 rapidly sink out of the water column, thereby transporting large quantities of carbon to depth (Arrigo et al., 2000;
980 Ditullio et al., 2000). The dominance of *P. antarctica* at LCIS may thus be important for carbon storage in MWDW
981 and the bottom waters, as well as for the transport of organic matter to the benthos.

982
983 As SSTs rise and sea-ice melts, a shift from *P. antarctica*- to diatom-dominated phytoplankton blooms is expected
984 because diatoms flourish in areas of recent sea-ice melt (Boyd and Doney 2002; Arrigo and van Dijken 2003;
985 Petrou et al. 2016; Ferreira et al. 2020). [Our results are consistent with this floristic shift hypothesis. For example,](#)
986 [at L10 where recent sea-ice melt \(Figure 2a and c\) had increased water column stratification, a different](#)
987 [phytoplankton community was observed compared to the other LCIS stations, with diatoms dominating over *P.*](#)
988 [antarctica \(Figure 9\). By contrast, at other LCIS stations, *P. antarctica* dominated the biomass due to the low](#)
989 [light conditions caused by the deep MLDs that initially characterize coastal polynyas](#). Given the anomalously high
990 carbon-to-nutrient content of *P. antarctica*, a shift to diatom-dominated phytoplankton blooms may negatively
991 affect the export and storage of carbon in MWDW and the bottom waters. However, rising SSTs will also lead to
992 increased glacial and ice shelf melt, further stratifying the adjacent water column and increasing the iron supply
993 (Petrou et al., 2016). It is projected that these conditions will favour blooms of heavily-silicified diatom species
994 [\(Deppeler and Davidson 2017\)](#) that are known to sink rapidly out of the mixed layer or, if consumed, their frustules
995 are expected to survive the gut passages of copepods, potentially resulting in increased carbon export (Assmy et
996 al., 2013). However, this increase is unlikely to be two-fold that presently contributed by *P. antarctica*.
997 [Additionally, the sinking shells of heavily-silicified diatoms have at times been observed to be devoid of organic](#)
998 [carbon \(Smetacek, 2000; Assmy et al., 2013\), which would further decrease the carbon export potential of diatoms](#)
999 [compared to colonial *P. antarctica*](#). In net, the expected floristic shift may lead to decreased carbon export at the
1000 ice shelves, subsequently decreasing the carbon content of the MWDW formed at LCIS [and/or the food supply to](#)
1001 [the benthos](#). Further investigation of the drivers of phytoplankton community composition is required to validate
1002 these hypotheses, particularly with regards to the response of Antarctic phytoplankton to warming, as well as to
1003 how changes in the surface ecosystem are transferred to and reflected in the biogeochemistry of bottom waters
1004 and benthic ecosystem functioning.

1005 5. Conclusions

1006 We investigated the summertime productivity of understudied regions of the Weddell Sea, including LCIS, along
1007 with the potential importance of different phytoplankton groups for biomass production, nutrient consumption,
1008 and carbon export potential. Our data show that mixed-layer nutrient depletion ratios are determined by the

1010 dominant phytoplankton group. The lowest Si:N and highest N:P depletion ratios were observed at LCIS where
1011 *P. antarctica* was dominant, while the highest Si:N and lowest N:P depletion ratios occurred at FIS and in the
1012 WG where diatoms dominated. The variability in phytoplankton community composition appears to have been
1013 largely driven by mechanisms controlling water column stratification. *P. antarctica* are low-light specialists and
1014 proliferated at LCIS due to the deep mixed layers that occurred early in the season, while diatoms succeeded at
1015 stations where the mixed layer was shallow, induced by sea-ice melt. Not only does the observed relationship
1016 between phytoplankton community composition and the nutrient depletion ratios have implications for the
1017 stoichiometry of the deep-water nutrient reservoir, but it likely also has consequences for carbon export and
1018 storage (Brzezinski et al. 2003; Weber and Deutsch 2010).

1019
1020 Although the waters adjacent to LCIS were characterized by the highest NO_3^- uptake rates, they also yielded the
1021 lowest f-ratios. We attribute these f-ratios to a degree of NH_4^+ inhibition of NO_3^- uptake, which translates to a
1022 missed opportunity for carbon export (Cochlan and Bronk, 2003) and potentially, decreased long-term storage in
1023 bottom waters, particularly since neither NO_3^- nor iron appeared to be limiting at the time of our sampling.
1024 Additional investigation is required to ascertain the persistence of NH_4^+ inhibition in the Antarctic CCSZ,
1025 particularly in regions of deep-water formation (e.g., at FRIS). Furthermore, given the prediction that the Weddell
1026 Sea's upper water column will become more stratified with climate change (Pörtner et al., 2014; Sallée et al.,
1027 2013; Stammerjohn et al., 2012), it is essential that we improve our understanding of the physical and chemical
1028 drivers of phytoplankton community composition and function if we are to better predict changes to ocean carbon
1029 cycling and drawdown via the biological [carbon pump](#).

1030

1031 6. Figure and table captions

1032 **Figure 1.** Maps of the Weddell Sea, Larsen C Ice Shelf (LCIS; insert a) and Fimbul Ice Shelf (FIS; insert b)
1033 showing the position of the stations where rate experiments were conducted during the Weddell Sea Expedition
1034 in January/February 2019. The symbols represent the different regions of the Weddell Sea sampled during the
1035 expedition (circle – Antarctic Peninsula (AP); diamond – FIS; triangle – LCIS; square – Weddell Gyre (WG)).
1036 The general cyclonic circulation of the Weddell Gyre (dashed blue arrow) is illustrated on the central map, with
1037 the dashed black arrows indicating the input of modified water masses from Filchner-Ronne Ice shelf (FRIS) and
1038 LCIS (Gordon et al. 1993; Schröder et al. 2002; Schodlok et al. 2002). The hypothesized circulation at LCIS
1039 (Nicholls et al. 2004; Hutchinson et al. 2020) is shown by the dashed light-blue arrow in insert (a). The 3.125 km
1040 sea-ice concentration data [from 31 January 2020](#) shown in the central panel were taken from [ftp://ftp-](ftp://ftp-projects.cen.uni-hamburg.de/seaice/AMSR2/3.125km)
1041 [projects.cen.uni-hamburg.de/seaice/AMSR2/3.125km](ftp://ftp-projects.cen.uni-hamburg.de/seaice/AMSR2/3.125km) and the bathymetry data (inserts a and b) were taken from
1042 ETOPO1 (NOAA National Geophysical Data Center 2009).

1043

1044 **Figure 2.** Depth profiles of (a) potential density (σ_θ), (b) potential temperature, (c) absolute salinity, and (d)
1045 photosynthetically active radiation (PAR) in the upper 150 [m](#) and (e) σ_θ , (f) potential temperature, and (g) absolute
1046 [salinity in the upper 1500 m](#) at all stations. The water masses present at each station, identified by their temperature
1047 and salinity characteristics, are denoted in panels (e-g) as follows: WSBW – Weddell Sea Bottom Water, WSDW
1048 – Weddell Sea Deep Water, WDW – Warm Deep Water, MWDW – Modified Warm Deep Water, ISW – Ice
1049 Shelf Water, HSSW – High Salinity Shelf Water, WW – Winter Water, ASW – Antarctic Surface Water. In panel

1050 (f), the dark yellow rectangle indicates HSSW. [The general station locations are indicated by the different marker](#)
1051 [colours: red shades – Antarctic Peninsula, green shades – Larsen C Ice Shelf, blue shade –Weddell Gyre, light](#)
1052 [purple shades – early summer Fimbul Ice Shelf, and dark purple – late summer Fimbul Ice Shelf.](#)

1053
1054 **Figure 3.** Depth profiles (0-500 m) of (a) NH_4^+ , (b) urea-N, (c) NO_2^- , (d) NO_3^- , (e) Si(OH)_4 , and (f) PO_4^{3-}
1055 concentrations. For all panels, the error bars represent ± 1 SD of replicate samples ($n = 2-3$). For NO_3^- , which was
1056 calculated as $\text{NO}_3^- + \text{NO}_2^- - \text{NO}_2^-$, error has been propagated according to standard statistical practices. Note that
1057 the x-axis scales in panels (d-f) do not start at zero.

1058
1059 **Figure 4.** Depth profiles (0-150 m) of (a) NO_3^- depletion, (b) Si(OH)_4 depletion, and (c) PO_4^{3-} depletion at each
1060 station. Also shown are scatterplots of (d) Si(OH)_4 depletion versus total N depletion (coloured symbols; see text
1061 for details) and Si(OH)_4 depletion versus NO_3^- depletion (grey symbols) and (e) PO_4^{3-} depletion versus total N
1062 depletion (coloured symbols) and PO_4^{3-} depletion versus NO_3^- depletion (grey symbols) at each station. The
1063 dashed line in panel (d) represents the 1:1 Si:N depletion ratio, expected for iron-replete diatoms (Ragueneau et
1064 al. 2000; Hutchins and Bruland 1998; Takeda 1998; Mosseri et al. 2008), while the dotted lines represent the 2:1
1065 Si:N ratio, expected for iron-limited diatoms (Arrigo et al., 1999; Franck et al., 2000; Brzezinski et al., 2003;
1066 Green and Sambrotto, 2006; Mosseri et al., 2008; Weber and Deutsch, 2010a; Martiny et al., 2013), and the 1:2
1067 Si:N ratio, indicative of enhanced activity of non-siliceous phytoplankton. The dashed line in panel (e) represents
1068 the 16:1 N:P depletion ratio (the Redfield ratio), while the dotted lines represent the 20:1 N:P ratio, expected for
1069 *P. antarctica*, and the 14:1 N:P ratio, expected for iron-replete diatoms (Hutchins and Bruland 1998; Takeda 1998;
1070 Arrigo et al. 1999; Ragueneau et al. 2000; Mosseri et al. 2008).

1071
1072 **Figure 5.** Bar plots of (a, d, g) [POC concentrations](#), (b, e, h) PON concentrations, and (c, f, i) biomass C:N ratios
1073 measured at the 55% (a-c), 10% (d-f), and 1% light levels (g-i). The stations are labelled on the x-axis, and the
1074 general stations locations are indicated by the different colours: red shades – Antarctic Peninsula, green shades –
1075 Larsen C Ice Shelf, blue shade –Weddell Gyre, light purple shades – early summer Fimbul Ice Shelf, and dark
1076 purple – late summer Fimbul Ice Shelf. The dotted black horizontal line in panels (c), (f), and (i) shows the
1077 Redfield C:N ratio of 6.63. The purple star in panel (i) indicates the anomalously high C:N ratio estimated for the
1078 1% PAR depth at station F2. The error bars represent ± 1 SD of replicate samples ($n = 2-6$). Where applicable,
1079 the error has been propagated according to standard statistical practices.

1080
1081 **Figure 6.** Daily rates of (a, e, i) NPP, (b, f, j) ρNO_3^- , (c, g, k) ρNH_4^+ , and (d, h, l) ρurea for the 55% (a-d), 10%
1082 (e-h), and 1% light levels (i-l). Where there are no bars in panels (d), (h) and (l), no data are available. The stations
1083 are labelled on the x-axis, and the general station locations are indicated by the different colours: red shades –
1084 Antarctic Peninsula, green shades – Larsen C Ice Shelf, blue shade –Weddell Gyre, light purple shades – early
1085 summer Fimbul Ice Shelf, and dark purple – late summer Fimbul Ice Shelf. The error bars represent ± 1 SE of
1086 replicate experiments ($n = 2$).

1087
1088 **Figure 7.** Depth profiles of NO_2^- oxidation rates measured at each station (a) between the surface and 500 m, and
1089 (b) within the euphotic zone.

1090
1091 **Figure 8.** Euphotic zone-integrated f-ratios estimated for each station. The black-hashed and white bars show the
1092 difference between the $f\text{-ratio}_{\text{(excluding urea)}}$ (higher value; equation 4a) and the $f\text{-ratio}_{\text{(including urea)}}$ (lower value;
1093 equation 4b), with the black-hashed bars indicating the stations where urea uptake was measured and the white
1094 bars where it was estimated (see text for details).

1095
1096 **Figure 9.** The (a, d) cell counts, (b, e) relative cell abundances, (c) log-transformed biovolume, and (f) carbon
1097 biomass of all phytoplankton groups identified from (a-c) surface flow cytometry samples and (d-f) plankton net-
1098 tow samples. The stations are labelled on the x-axis. Where there are no bars in panels (d), (e), and (f), no data are
1099 available. Carbon biomass estimates in panel (f) are shown only for the prymnesiophyte, *P. antarctica*, and the
1100 diatom species.

1101
1102 **Figure 10.** Euphotic zone-averaged rates of (a) NPP versus SST, (b) ρNO_3^- versus euphotic zone depth (Z_{eu}), (c)
1103 N uptake (left y-axis) versus PON (bottom x-axis) and NPP (right y-axis) versus POC (top x-axis), (d) ρNH_4^+
1104 versus NH_4^+ concentration, and (e) purea versus urea concentration, as well as (f) the concentrations of NH_4^+
1105 (black outlined symbols; left y-axis) and urea (grey outlined symbols; right y-axis) versus PON at each station.
1106 The symbols in panel (a) are coloured by ρNO_3^- , in panel (b) by NO_3^- concentration, and in panel (c) by NPP
1107 (pink), ρNO_3^- (black), ρNH_4^+ (blue), and purea (grey).

1108
1109 **Figure 11.** Scatterplots of (a) the Si:N depletion ratio (i.e., (i.e., Si(OH)_4 -to-total N depletion) versus the % diatom
1110 abundance, (b) N:P depletion ratio (i.e., total N-to- PO_4^{3-} depletion) versus the % *P. antarctica* abundance, (c) %
1111 of total N (i.e., $\text{NO}_3^- + \text{NH}_4^+ + \text{urea}$) assimilated as NO_3^- versus the % diatom abundance, and (d) % of total N
1112 assimilated as regenerated N (i.e., $\text{NH}_4^+ + \text{urea}$) versus the % *P. antarctica* abundance at each station.

1113
1114 **Figure 12.** (a) NO_3^- uptake normalised to NH_4^+ uptake as a function of NH_4^+ concentration and b) NO_3^- depletion
1115 versus NH_4^+ concentration. The symbols in panel (a) are coloured by NH_4^+ uptake rate (ρNH_4^+) and in panel (b)
1116 by PON concentration. In panel (b), the symbol size indicates the incubation light level, NO_3^- depletion at LCIS
1117 corresponds with the left y-axis, and NO_3^- depletion at all other (“non-LCIS”) stations corresponds with the right
1118 y-axis.

1119
1120 **Table 1.** Euphotic zone-averaged N nutrient concentrations, nutrient depletions, and nutrient depletion ratios at
1121 each station occupied in the Weddell Sea in January/February 2019. Values shown are averages ± 1 SD ($n \geq 2$),
1122 with error propagated according to standard statistical practices where appropriate. “–” indicates no available data.

1123
1124 **Table 2.** Euphotic zone-integrated and averaged rates at each station occupied in the Weddell Sea in
1125 January/February 2019. Values shown are averages ± 1 SD ($n \geq 2$), with error propagated according to standard
1126 statistical practices where appropriate. “–” indicates no available data. The values shown in italics (i.e., purea)
1127 were estimated rather than measured (see text for details).

1128
1129 **7. Author contributions**

1130 RF led the study and writing of the manuscript. SF contributed substantially to writing the manuscript, and
1131 designed the experiments with RF and TB. RF and JB carried out the experiments. JB, TB, SF, KS, and SS assisted
1132 with sampling and data generation, and contributed to writing the manuscript.

1133

1134 **8. Acknowledgements**

1135 We thank Captain Knowledge Bengu, Captain Freddie Ligthelm, and the exceptional crew of the RV *SA Agulhas*
1136 *II*, as well as the Weddell Sea Expedition 2019. We also thank R. Audh, T. Henry, K. Hutchinson, and H. Luyt
1137 for assistance at sea, R. Roman for help with nutrient analyses, the University of Cape Town (UCT) Marine
1138 Biogeochemistry Lab, the High-Resolution Transmission Electron Microscopy Unit of the Nelson Mandela
1139 University, I. Newton and J. Luyt at the UCT Stable Light Isotope Laboratory, K. Pecsok Ewert at the UC Davis
1140 Stable Isotope Facility, and T. Reid and L. Haraguchi for assistance with flow cytometry analyses. This research
1141 was supported by the Flotilla Foundation through a grant to S.E.F. and T.B.; the South African National Antarctic
1142 Program through grants 105539, 117035, and 129232 to S.E.F.; the South African National Research Foundation
1143 through postgraduate fellowships to R.F.F., J.M.B., S.S. and K.A.M.S.; UCT through a Science Faculty
1144 Fellowship to R.F.F., Vice-Chancellor Doctoral Research Scholarships and Postgraduate Merit Awards to R.F.F.,
1145 J.M.B. and S.S., and a Vice-Chancellor Future Leaders 2030 award to S.E.F.; and the African Academy of
1146 Sciences/Royal Society through a FLAIR Fellowship to S.E.F. The authors also acknowledge the South African
1147 Department of Science and Innovation's Biogeochemistry Research Infrastructure Platform (BIOGRIP) and
1148 Shallow Marine and Coastal Research Infrastructure (SMCRI). The data discussed in this manuscript are available
1149 in the Zenodo database and can be found at [10.5281/zenodo.4737280](https://doi.org/10.5281/zenodo.4737280).

1150

1151 **9. References**

1152 Alderkamp, A.-C., Kulk, G., Buma, A. G. J., Visser, R. J. W., Dijken, G. L. Van, Mills, M. M., and Arrigo, K.
1153 R.: The effect of iron limitation on the photophysiology of *Phaeocystis Antarctica* (Prymnesiophyceae) and
1154 *Fragilariopsis cylindrus* (Bacillariophyceae) under dynamic irradiance, *J. Phycol.*, 48, 45–59,
1155 <https://doi.org/10.1111/J.1529-8817.2011.01098.X>, 2012.

1156 Altabet, M. A. and Francois, R.: Nitrogen isotope biogeochemistry of the Antarctic polar frontal zone at 170°W,
1157 *Deep. Res. Part II Top. Stud. Oceanogr.*, 48, 4247–4273, [https://doi.org/10.1016/S0967-0645\(01\)00088-1](https://doi.org/10.1016/S0967-0645(01)00088-1), 2001.

1158 Arrigo, K. R. and van Dijken, G. L.: Phytoplankton dynamics within 37 Antarctic coastal polynya systems, *J.*
1159 *Geophys. Res. Ocean.*, 108, <https://doi.org/10.1029/2002jc001739>, 2003.

1160 Arrigo, K. R., Robinson, D. H., Worthen, D. L., Dunbar, R. B., DiTullio, G. R., VanWoert, M., and Lizotte, M.
1161 P.: Phytoplankton community structure and the drawdown of nutrients and CO₂ in the Southern Ocean, *Science*
1162 (80-.), 283, 365–367, <https://doi.org/10.1126/science.283.5400.365>, 1999.

1163 Arrigo, K. R., DiTullio, G. R., Dunbar, R. B., Robinson, D. H., VanWoert, M., Worthen, D. L., and Lizotte, M.
1164 P.: Phytoplankton taxonomic variability in nutrient utilization and primary production in the Ross Sea, *J.*
1165 *Geophys. Res. Ocean.*, 105, 8827–8846, <https://doi.org/10.1029/1998jc000289>, 2000.

1166 Arrigo, K. R., van Dijken, G., and Long, M.: Coastal Southern Ocean: A strong anthropogenic CO₂ sink,
1167 *Geophys. Res. Lett.*, 35, 1–6, <https://doi.org/10.1029/2008GL035624>, 2008.

1168 Arteaga, L. A., Boss, E., Behrenfeld, M. J., Westberry, T. K., and Sarmiento, J. L.: Seasonal modulation of
1169 phytoplankton biomass in the Southern Ocean, *Nat. Commun.* 2020 111, 11, 1–10,

1170 <https://doi.org/10.1038/s41467-020-19157-2>, 2020.

1171 Assmy, P., Smetacek, V., Montresor, M., Klaas, C., Henjes, J., Strass, V. H., Arrieta, J. M., Bathmann, U., Berg,
1172 G. M., Breitbarth, E., Cisewski, B., Friedrichs, L., Fuchs, N., Herndl, G. J., Jansen, S., Krägelnsky, S., Latasa,
1173 M., Peeken, I., Röttgers, R., Scharek, R., Schüller, S. E., Steigenberger, S., Webb, A., and Wolf-Gladrow, D.:
1174 Thick-shelled, grazer-protected diatoms decouple ocean carbon and silicon cycles in the iron-limited Antarctic
1175 Circumpolar Current., *Proc. Natl. Acad. Sci. U. S. A.*, 110, 20633–8, <https://doi.org/10.1073/pnas.1309345110>,
1176 2013.

1177 Bendschneider, K., Robinson, R. J., Margeson, J. H., Suggs, J. C., Midgett, M. R., Method, C. R., Dussin, R.,
1178 Curchitser, E. N., Stock, C. A., Van Oostende, N., Galán, A., Zirbel, M. J., Saldías, G. S., Chan, F., Letelier, R.,
1179 Najjar, G., Sarmiento, J. L., Xi, S., Scientific, T., Berelson, W. M., McManus, J., Coale, K. H., Johnson, K. S.,
1180 Kilgore, T., Burdige, D., Pilskaln, C., Flohr, A., Van Der Plas, A. K., Emeis, K. C., Mohrholz, V., and Rixen,
1181 T.: A New Spectrophotometric Method for the Determination of Nitrite in Sea Water, *J. Mar. Res.*, 11, 0–1,
1182 <https://doi.org/10.1357/0022240963213673>, 2020.

1183 Berges, J. A. and Mulholland, M. R.: Enzymes and Nitrogen Cycling, 1385–1444 pp.,
1184 <https://doi.org/10.1016/B978-0-12-372522-6.00032-3>, 2008.

1185 Böhlke, J. K. and Coplen, T. B.: Interlaboratory comparison of reference materials for nitrogenisotope- ratio
1186 measurements, 1995.

1187 Böhlke, J. K., Mroczkowski, S. J., and Coplen, T. B.: Oxygen isotopes in nitrate: New reference materials for
1188 18O: 17O: 16O measurements and observations on nitrate-water equilibration., *Rapid Commun. Mass*
1189 *Spectrom.*, 17, 1835–1846, 2003.

1190 Boyd, P. W. and Doney, S. C.: Modelling regional responses by marine pelagic ecosystems to global climate
1191 change, *Geophys. Res. Lett.*, 29, 53-1-53-4, <https://doi.org/10.1029/2001gl014130>, 2002.

1192 Boyd, P. W.: Ironing out algal issues in the Southern Ocean, *Nature*, 304, 396–397, 2004.

1193 Boyd, P. W., Jickells, T., Law, C. S., Blain, S., Boyle, E. A., Buesseler, K. O., Coale, K. H., Cullen, J. J., De
1194 Baar, H. J. W., Follows, M., Harvey, M., Lancelot, C., Levasseur, M., Owens, N. P. J., Pollard, R., Rivkin, R.
1195 B., Sarmiento, J., Schoemann, V., Smetacek, V., Takeda, S., Tsuda, A., Turner, S., and Watson, A. J.:
1196 Mesoscale iron enrichment experiments 1993-2005: Synthesis and future directions, *Science (80-.)*, 315, 612–
1197 617, <https://doi.org/10.1126/science.1131669>, 2007.

1198 Boyd, P. W., Doney, S. C., Strzpek, R., Dusenberry, J., Lindsay, K., and Fung, I.: Climate-mediated changes to
1199 mixed-layer properties in the Southern Ocean: assessing the phytoplankton response, 5, 847–864,
1200 <https://doi.org/10.5194/bg-5-847-2008>, 2008.

1201 Boyd, P. W. and Ellwood, M. J.: The biogeochemical cycle of iron in the ocean, *Nat. Geosci.*, 3, 675–682,
1202 <https://doi.org/10.1038/ngeo964>, 2010.

1203 Brennecke, W.: Die ozeanographischen Arbeiten der Deutschen Antarktischen Expedition 1911-12, Aus dem
1204 *Arciv der Deutchen Seewarte*, 39, 1–216, 1921.

1205 Brzezinski, M. A., Dickson, M. L., Nelson, D. M., and Sambrotto, R.: Ratios of Si, C and N uptake by
1206 microplankton in the Southern Ocean, *Deep. Res. Part II Top. Stud. Oceanogr.*, 50, 619–633,
1207 [https://doi.org/10.1016/S0967-0645\(02\)00587-8](https://doi.org/10.1016/S0967-0645(02)00587-8), 2003.

1208 Cape, M. R., Vernet, M., Kahru, M., and Spreen, G.: Polynya dynamics drive primary production in the Larsen
1209 A and B embayments following ice shelf collapse, *J. Geophys. Res. Ocean.*, 119, 572–594,

1210 <https://doi.org/10.1002/2013JC009441>, 2014.

1211 Carvalho, F., Kohut, J., Oliver, M. J., and Schofield, O.: Defining the ecologically relevant mixed-layer depth
1212 for Antarctica's coastal seas, *Geophys. Res. Lett.*, 44, 338–345, <https://doi.org/10.1002/2016GL071205>, 2017.

1213 Cochlan, W. P. and Bronk, D. A.: Effects of ammonium on nitrate utilization in the Ross Sea, Antarctica:
1214 Implications for *f*-ratio estimates, 78, 159–178, <https://doi.org/10.1029/078ars10>, 2003.

1215 Cota, G. F., Smith, W. O., Nelson, D. M., Muench, R. D., and Gordon, L. I.: Nutrient and biogenic particulate
1216 distributions, primary productivity and nitrogen uptake in the Weddell-Scotia Sea marginal ice zone during
1217 winter, *J. Mar. Res.*, 50, 155–181, <https://doi.org/10.1357/002224092784797764>, 1992.

1218 De Baar, H. J. W., Boyd, P. W., Coale, K. H., Landry, M. R., Tsuda, A., Assmy, P., Bakker, D. C. E., Bozec, Y.,
1219 Barber, R. T., Brzezinski, M. A., Buesseler, K. O., Boyé, M., Croot, P. L., Gervais, F., Gorbunov, M. Y.,
1220 Harrison, P. J., Hiscock, W. T., Laan, P., Lancelot, C., Law, C. S., Levasseur, M., Marchetti, A., Millero, F. J.,
1221 Nishioka, J., Nojiri, Y., Van Oijen, T., Riebesell, U., Rijkenberg, M. J. A., Saito, H., Takeda, S., Timmermans,
1222 K. R., Veldhuis, M. J. W., Waite, A. M., and Wong, C.-S.: Synthesis of iron fertilization experiments: From the
1223 Iron Age in the Age of Enlightenment, *J. Geophys. Res.*, 110, 9–16, <https://doi.org/10.1029/2004JC002601>,
1224 2005.

1225 De Jong, J., Schoemann, V., Lannuzel, D., Croot, P., De Baar, H., and Tison, J. L.: Natural iron fertilization of
1226 the Atlantic sector of the Southern Ocean by continental shelf sources of the Antarctic Peninsula, *J. Geophys.*
1227 *Res. Biogeosciences*, 117, <https://doi.org/10.1029/2011JG001679>, 2012.

1228 Deary, A.: A high-resolution study of the early- to late-summer progression in primary production and carbon
1229 export potential in the Atlantic Southern Ocean Supervisor : Dr Sarah Fawcett, 2020.

1230 Delmont, T. O., Hammar, K. M., Ducklow, H. W., Yager, P. L., and Post, A. F.: *Phaeocystis antarctica* blooms
1231 strongly influence bacterial community structures in the Amundsen Sea polynya, *Front. Microbiol.*, 5, 1–13,
1232 <https://doi.org/10.3389/fmicb.2014.00646>, 2014.

1233 DeVries, T.: The Oceanic Anthropogenic CO₂ Sink: Storage, Air-Sea Fluxes, and Transports over the Industrial
1234 Era, *Global Biogeochem. Cycles*, 28, 631–647, 2014.

1235 Diamond, D.: QuikChem Method 10-114-21-1-B: Silicate by flow injection analysis., 1994.

1236 Dinniman, M. S., St-Laurent, P., Arrigo, K. R., Hofmann, E. E., and Dijken, G. L. van: Analysis of Iron Sources
1237 in Antarctic Continental Shelf Waters, *J. Geophys. Res. Ocean.*, 125, e2019JC015736,
1238 <https://doi.org/10.1029/2019JC015736>, 2020.

1239 Ditullio, G. R., Grebmeier, J. M., Arrigo, K. R., and Lizotte, M. P.: Rapid and early export of *Phaeocystis*
1240 *antarctica* blooms in the Ross Sea , Antarctica, 404, 1996–1999, 2000.

1241 Dortch, Q.: The interaction between ammonium and nitrate uptake in phytoplankton, *Mar. Ecol. Prog. Ser.*, 61,
1242 183–201, <https://doi.org/10.3354/meps061183>, 1990.

1243 Dowdeswell, J., Shears, J., Batchelor, C., Christie, F., Rack, W., Montelli, A., Evans, J., Dowdeswell, E.,
1244 Ottesen, D., Fawcett, S., Bornman, T., Hutchinson, K., Audh, R., Burger, J., Flynn, R., Henry, T., Luyt, H.,
1245 Smith, S., Spence, K., Woodall, L., Taylor, M., Frinault, B., Bekker, A., Zu, L., van Zijl, C., Matthee, J., and
1246 Makgabutlane, M.: The Weddell Sea Expedition 2019: Cruise Scientific Report,
1247 <https://doi.org/https://doi.org/10.17863/CAM.58103>, 2019.

1248 Dubelaar, G. B. J. and Jonker, R. R.: Flow cytometry as a tool for the study of phytoplankton, *Sci. Mar.*, 64,
1249 135–156, <https://doi.org/10.3989/scimar.2000.64n2135>, 2000.

1250 Dugdale, R. C. and Goering, J. J.: Uptake of New and Regenerated Forms of Nitrogen in Primary Productivity,
1251 *Limnol. Oceanogr.*, 12, 196–206, <https://doi.org/10.4319/lo.1967.12.2.0196>, 1967.

1252 Dugdale, R. C. and Wilkerson, F. P.: The use of ^{15}N to measure nitrogen uptake in eutrophic experimental
1253 considerations I t2, 3, 1986.

1254 Eicken, H.: The role of sea ice in structuring Antarctic ecosystems, in: *Weddell Sea Ecology*, 3–13, 1993.

1255 El-Sayed, S.: Productivity of the Antarctic Waters — A Reappraisal, in: *Marine Phytoplankton and*
1256 *Productivity. Lecture Notes on Coastal and Estuarine Studies.*, edited by: O., H.-H., L., B., and R., G., Springer
1257 Berlin Heidelberg, 19–34, 1984.

1258 El-Sayed, S. Z. and Taguchi, S.: Primary production and standing crop of phytoplankton along the ice-edge in
1259 the Weddell Sea, *Deep Sea Res. Part A, Oceanogr. Res. Pap.*, 28, 1017–1032, <https://doi.org/10.1016/0198->
1260 [0149\(81\)90015-7](https://doi.org/10.1016/0198-0149(81)90015-7), 1981.

1261 Eppley, R. W., Peterson, B.: Particulate organic matter flux and planktonic new production in the deep ocean,
1262 *Nature*, 282, 677–680, 1979.

1263 Fahrback, E., Rohardt, G., Schröder, M., and Strass, V.: Transport and structure of the weddell gyre, *Ann.*
1264 *Geophys.*, 12, 840–855, <https://doi.org/10.1007/s00585-994-0840-7>, 1994.

1265 Fahrback, E., Rohardt, G., Scheele, N., Schroder, M., Strass, V., and Wisotzki, A.: Formation and discharge of
1266 deep and bottom water in the northwestern Weddell Sea, *J. Mar. Res.*, 53, 515–538,
1267 <https://doi.org/10.1357/0022240953213089>, 1995.

1268 Ferreira, A., Costa, R. R., Dotto, T. S., Kerr, R., Tavano, V. M., Brito, A. C., Brotas, V., Secchi, E. R., and
1269 Mendes, C. R. B.: Changes in Phytoplankton Communities Along the Northern Antarctic Peninsula: Causes,
1270 Impacts and Research Priorities, *Front. Mar. Sci.*, 7, <https://doi.org/10.3389/fmars.2020.576254>, 2020.

1271 Finkel, Z. V., Quigg, A., Raven, J. A., Reinfelder, J. R., Schofield, O. E., and Falkowski, P. G.: Irradiance and
1272 the elemental stoichiometry of marine phytoplankton, *Limnol. Oceanogr.*, 51, 2690–2701,
1273 <https://doi.org/10.4319/LO.2006.51.6.2690>, 2006.

1274 Franck, V. M., Brzezinski, M. A., Coale, K. H., and Nelson, D. M.: Iron and silicic acid concentrations regulate
1275 Si uptake north and south of the Polar Frontal Zone in the Pacific Sector of the Southern Ocean, *Deep. Res. Part*
1276 *II Top. Stud. Oceanogr.*, 47, 3315–3338, [https://doi.org/10.1016/S0967-0645\(00\)00070-9](https://doi.org/10.1016/S0967-0645(00)00070-9), 2000.

1277 Fripiat, F., Sigman, D. M., Fawcett, S. E., Rafter, P. A., Weigand, M. A., and Tison, J.-L.: New insights into sea
1278 ice nitrogen biogeochemical dynamics from the nitrogen isotopes, *Global Biogeochem. Cycles*, 28, 115–130,
1279 <https://doi.org/10.1002/2013GB004729>, 2014.

1280 Fripiat, F., Meiners, K. M., Vancoppenolle, M., Papadimitriou, S., Thomas, D. N., Ackley, S. F., Arrigo, K. R.,
1281 Carnat, G., Cozzi, S., Delille, B., Dieckmann, G. S., Dunbar, R. B., Fransson, A., Kattner, G., Kennedy, H.,
1282 Lannuzel, D., Munro, D. R., Nomura, D., Rintala, J. M., Schoemann, V., Stefels, J., Steiner, N., and Tison, J. L.:
1283 Macro-nutrient concentrations in Antarctic pack ice: Overall patterns and overlooked processes, 5,
1284 <https://doi.org/10.1525/elementa.217>, 2017.

1285 Fripiat, F., Martínez-García, A., Marconi, D., Fawcett, S., Kopf, S., Luu, V., Rafter, P., Zhang, R., Sigman, D.,
1286 and Haug, G.: Nitrogen isotopic constraints on nutrient transport to the upper ocean, *Nat. Geosci.*, 2021.

1287 Frölicher, T. L., Sarmiento, J. L., Paynter, D. J., Dunne, J. P., Krasting, J. P., and Winton, M.: Dominance of the
1288 Southern Ocean in anthropogenic carbon and heat uptake in CMIP5 models, *J. Clim.*, 28, 862–886, 2015.

1289 Garcia, N. S., Sexton, J., Riggins, T., Brown, J., Lomas, M. W., and Martiny, A. C.: High variability in cellular

1290 stoichiometry of carbon, nitrogen, and phosphorus within classes of marine eukaryotic phytoplankton under
1291 sufficient nutrient conditions, *Front. Microbiol.*, 9, 1–10, <https://doi.org/10.3389/fmicb.2018.00543>, 2018.

1292 Gill, A. E.: Circulation and bottom water production in the Weddell Sea, *Deep. Res. Oceanogr. Abstr.*, 20, 111–
1293 140, [https://doi.org/10.1016/0011-7471\(73\)90048-X](https://doi.org/10.1016/0011-7471(73)90048-X), 1973.

1294 Gleitz, M., Michiel, M. R., Thomas, D. N., Dieckmann, G. S., and Millero, F. J.: Comparison of summer and
1295 winter inorganic carbon, oxygen and nutrient concentrations in Antarctic sea ice brine, *Mar. Chem.*, 51, 81–91,
1296 [https://doi.org/10.1016/0304-4203\(95\)00053-T](https://doi.org/10.1016/0304-4203(95)00053-T), 1995.

1297 Glibert, P. M., Wilkerson, F. P., Dugdale, R. C., Raven, J. A., Dupont, C. L., Leavitt, P. R., Parker, A. E.,
1298 Burkholder, J. M., and Kana, T. M.: Pluses and minuses of ammonium and nitrate uptake and assimilation by
1299 phytoplankton and implications for productivity and community composition, with emphasis on nitrogen-
1300 enriched conditions, *Limnol. Oceanogr.*, 61, 165–197, <https://doi.org/10.1002/lno.10203>, 2016.

1301 Goeyens, L.: Ammonium regeneration in the Scotia-Weddell Confluence area during spring 1988, *Mar. Ecol.*
1302 *Prog. Ser.*, 78, 241–252, <https://doi.org/10.3354/meps078241>, 1991.

1303 Goeyens, L., Tréguer, P., Baumann, M. E. M., Baeyens, W., and Dehairs, F.: The leading role of ammonium in
1304 the nitrogen uptake regime of Southern Ocean marginal ice zones, *J. Mar. Syst.*, 6, 345–361,
1305 [https://doi.org/10.1016/0924-7963\(94\)00033-8](https://doi.org/10.1016/0924-7963(94)00033-8), 1995.

1306 Goffart, A., Catalano, G., and Hecq, J. H.: Factors controlling the distribution of diatoms and Phaeocystis in the
1307 Ross Sea, *J. Mar. Syst.*, 27, 161–175, [https://doi.org/10.1016/S0924-7963\(00\)00065-8](https://doi.org/10.1016/S0924-7963(00)00065-8), 2000.

1308 Gonfiantini, R.: Stable isotope reference samples for geochemical and hydrological investigations., Rep. Advis.
1309 Group, Vienna., 1984.

1310 Gordon, A. L., Huber, B. A., Hellmer, H. H., & Ffield, A.: Deep and bottom water of the Weddell Sea’s western
1311 rim., *Science (80-.)*, 265, 95–97, 1993.

1312 Granger, J. and Sigman, D. M.: Removal of nitrite with sulfamic acid for nitrate N and O isotope analysis with
1313 the denitrifier method, *Rapid Commun. Mass Spectrom.*, 23, 3753–3762, <https://doi.org/10.1002/rcm.4307>,
1314 2009.

1315 Grasshoff, K.: *Methods of seawater analysis*, Weinheim and New York: Verlag Chemie, 1976.

1316 Green, S. E. and Sambrotto, R. N.: Plankton community structure and export of C, N, P and Si in the Antarctic
1317 Circumpolar Current, *Deep. Res. Part II Top. Stud. Oceanogr.*, 53, 620–643,
1318 <https://doi.org/10.1016/j.dsr2.2006.01.022>, 2006.

1319 Gruber, N., Clement, D., Carter, B. R., Feely, R. A., Van Heuven, S., and Hoppema, M.: The oceanic sink for
1320 anthropogenic CO₂ from 1994 to 2007, *Science (80-.)*, 363, 1193–1199, 2019.

1321 Henley, S. F., Tuerena, R. E., Annett, A. L., Fallick, A. E., Meredith, M. P., Venables, H. J., Clarke, A., and
1322 Ganeshram, R. S.: Macronutrient supply, uptake and recycling in the coastal ocean of the west Antarctic
1323 Peninsula, *Deep. Res. Part II Top. Stud. Oceanogr.*, 139, 58–76, <https://doi.org/10.1016/j.dsr2.2016.10.003>,
1324 2017.

1325 Holmes, R. M., Aminot, A., Kerouel, R., Hooker, B. A., and Peterson, B. J.: A simple and precise method for
1326 measuring ammonium in marine and freshwater ecosystems, <https://doi.org/10.1139/cjfas-56-10-1801>, 1999.

1327 Hoppema, M. and Goeyens, L.: Redfield behavior of carbon, nitrogen, and phosphorus depletions in Antarctic
1328 surface water, *Limnol. Oceanogr.*, 44, 220–224, <https://doi.org/10.4319/lo.1999.44.1.0220>, 1999.

1329 Hoppema, M., Stoll, M. H. C., and De Baar, H. J. W.: CO₂ in the Weddell Gyre and Antarctic Circumpolar

1330 Current: Austral autumn and early winter, *Mar. Chem.*, 72, 203–220, [https://doi.org/10.1016/S0304-4203\(00\)00082-7](https://doi.org/10.1016/S0304-4203(00)00082-7), 2000a.

1331

1332 Hoppema, M., Goeyens, L., and Fahrbach, E.: Intense nutrient removal in the remote area off Larsen Ice Shelf (Weddell Sea), *Polar Biol.*, 23, 85–94, <https://doi.org/10.1007/s003000050012>, 2000b.

1333

1334 Hoppema, M.: Weddell Sea is a globally significant contributor to deep-sea sequestration of natural carbon dioxide, *Deep. Res. Part I Oceanogr. Res. Pap.*, 51, 1169–1177, <https://doi.org/10.1016/j.dsr.2004.02.011>, 2004.

1335

1336 Hoppema, M., Middag, R., de Baar, H., Fahrbach, E., van Weerlee, E., and Thomas, H.: Whole season net community production in the Weddell Sea, *Polar Biol.*, 31, 101–111, 2007.

1337

1338 Hoppema, M., Bakker, K., MAC van Heuven, S., van Ooijen, J. C., and de Baar, H. J.: Distributions, trends and inter-annual variability of nutrients along a repeat section through the Weddell Sea (1996-2011), <https://doi.org/10.1016/j.marchem.2015.08.007>, 2015.

1339

1340 Hutchins, D. A. and Bruland, K. W.: Iron-limited growth and Si:N ratios in a coastal upwelling regime, *Nature*, 393, 561–564, 1998.

1341

1342 Hutchinson, K., Deshayes, J., Sallee, J. B., Dowdeswell, J. A., de Lavergne, C., Ansoerge, I., Luyt, H., Henry, T., and Fawcett, S. E.: Water Mass Characteristics and Distribution Adjacent to Larsen C Ice Shelf, Antarctica, *J. Geophys. Res. Ocean.*, 125, 0–2, <https://doi.org/10.1029/2019JC015855>, 2020.

1343

1344 Isla, E., Rossi, S., Palanques, A., Gili, J. M., Gerdes, D., and Arntz, W.: Biochemical composition of marine sediment from the eastern Weddell Sea (Antarctica): High nutritive value in a high benthic-biomass environment, *J. Mar. Syst.*, 60, 255–267, <https://doi.org/10.1016/J.JMARSYS.2006.01.006>, 2006.

1345

1346 Isla, E., Gerdes, D., Rossi, S., Fiorillo, I., Sañé, E., Gili, J.-M., and Arntz, W. E.: Biochemical characteristics of surface sediments on the eastern Weddell Sea continental shelf, Antarctica: is there any evidence of seasonal patterns?, *Polar Biol.* 2011 348, 34, 1125–1133, <https://doi.org/10.1007/S00300-011-0973-6>, 2011.

1347

1348 Ito, T., Woloszyn, M., and Mazloff, & M.: Anthropogenic carbon dioxide transport in the Southern Ocean driven by Ekman flow, 463, <https://doi.org/10.1038/nature08687>, 2010.

1349

1350 Jacobs, S. S.: The Antarctic slope front, *Antarct. JUS*, 21, 123–124, 1986.

1351

1352 Jacobs, S. S.: On the nature and significance of the Antarctic Slope Front, *Mar. Chem.*, 35, 9–24, [https://doi.org/10.1016/S0304-4203\(09\)90005-6](https://doi.org/10.1016/S0304-4203(09)90005-6), 1991.

1353

1354 Jacques, G.: Is the concept of new production—regenerated production valid for the Southern Ocean?, *Mar. Chem.*, 35, 273–286, [https://doi.org/10.1016/S0304-4203\(09\)90022-6](https://doi.org/10.1016/S0304-4203(09)90022-6), 1991.

1355

1356 Jennings, J. C., Gordon, L. I., and Nelson, D. M.: Nutrient depletion indicates high primary productivity in the Weddell Sea, *Nature*, 309, 51–54, <https://doi.org/10.1038/309051a0>, 1984.

1357

1358 Kana, T. M. and Glibert, P. M.: Effect of irradiances up to 2000 $\mu\text{E m}^{-2} \text{s}^{-1}$ on marine *Synechococcus* WH7803-I. Growth, pigmentation, and cell composition, *Deep Sea Res. Part A, Oceanogr. Res. Pap.*, 34, 479–495, [https://doi.org/10.1016/0198-0149\(87\)90001-X](https://doi.org/10.1016/0198-0149(87)90001-X), 1987.

1359

1360 Kaprelyants, A. S. and Kell, D. B.: Dormancy in stationary-phase cultures of *Micrococcus luteus*: flow cytometric analysis of starvation and resuscitation, *Applied Environ. Microbiol.*, 59, 3187–3196, 1993.

1361

1362 Karsh, K. L., Trull, T. W., Lourey, M. J., and Sigman, D. M.: Relationship of nitrogen isotope fractionation to phytoplankton size and iron availability during the Southern Ocean Iron RElease Experiment (SOIREE), *Limnol. Oceanogr.*, 48, 1058–1068, <https://doi.org/10.4319/lo.2003.48.3.1058>, 2003.

1363

1364 Keffer, T. and Holloway, G.: Estimating Southern Ocean eddy flux of heat and salt from satellite altimetry,

1365

1366

1367

1368

1369

1370 Nature, 332, 624–626, <https://doi.org/10.1038/332624a0>, 1988.

1371 Keller, D. P., Kriest, L., Koeve, W., and Oeschles, A.: Southern Ocean biological impacts on global ocean
1372 oxygen, *Geophys. Res. Lett.*, 43, 6469–6477, 2016.

1373 Kerr, R., Mata, M. M., Mendes, C. R. B., and Secchi, E. R.: Northern Antarctic Peninsula: a marine climate
1374 hotspot of rapid changes on ecosystems and ocean dynamics, *Deep. Res. Part II Top. Stud. Oceanogr.*, 149, 4–9,
1375 <https://doi.org/10.1016/j.dsr2.2018.05.006>, 2018.

1376 Klunder, M. B., Laan, P., Middag, R., De Baar, H. J. W., and van Ooijen, J. C.: Dissolved iron in the Southern
1377 Ocean (Atlantic sector), *Deep. Res. Part II Top. Stud. Oceanogr.*, 58, 2678–2694,
1378 <https://doi.org/10.1016/j.dsr2.2010.10.042>, 2011.

1379 Klunder, M. B., Laan, P., De Baar, H. J. W., Middag, R., Neven, I., and Van Ooijen, J.: Dissolved Fe across the
1380 Weddell Sea and Drake Passage: impact of DFe on nutrient uptake, 11, 651–669, <https://doi.org/10.5194/bg-11-1381-651-2014>, 2014.

1382 Koike, I., Holm-Hansen, O., and Biggs, D.: Inorganic nitrogen metabolism by Antarctic phytoplankton with
1383 special reference to ammonium cycling, *Mar. Ecol. Prog. Ser.*, 30, 105–116,
1384 <https://doi.org/10.3354/meps030105>, 1986.

1385 Lannuzel, D., Schoemann, V., de Jong, J., Chou, L., Delille, B., Becquevort, S., and Tison, J. L.: Iron study
1386 during a time series in the western Weddell pack ice, *Mar. Chem.*, 108, 85–95,
1387 <https://doi.org/10.1016/j.marchem.2007.10.006>, 2008.

1388 Le Corre, P. and Minas, H.: Distributions et évolution des éléments nutritifs dans le secteur indien de l’Océan
1389 Antarctique en Wn de période estivale, *Oceanol. Acta*, 6, 365–381, 1983.

1390 Leblanc, K., Aristegui, J., Armand, L., Assmy, P., Beker, B., Bode, A., Breton, E., Cornet, V., Gibson, J.,
1391 Gosselin, M. P., Kopczynska, E., Marshall, H., Peloquin, J., Piontkovski, S., Poulton, A. J., Quéguiner, B.,
1392 Schiebel, R., Shipe, R., Stefels, J., Van Leeuwe, M. A., Varela, M., Widdicombe, C., and Yallop, M.: A global
1393 diatom database- A bundance, biovolume and biomass in the world ocean, *Earth Syst. Sci. Data*, 4, 149–165,
1394 <https://doi.org/10.5194/ESSD-4-149-2012>, 2012.

1395 Llort, J., Lévy, M., Sallée, J.-B., and Tagliabue, A.: Onset, intensification, and decline of phytoplankton blooms
1396 in the Southern Ocean, *J. Mar. Sci.*, 72, 1971–1984, <https://doi.org/10.1093/icesjms/fsv053>, n.d.

1397 Locarnini, R. A., Whitworth, T., and Nowlin, W. D.: The importance of the Scotia Sea on the outflow of
1398 Weddell Sea Deep Water, *J. Mar. Res.*, 51, 135–153, <https://doi.org/10.1357/0022240933223846>, 1993.

1399 Lomas, M. W. and Glibert, P. M.: Interactions between NH₄⁺ and NO₃⁻ uptake and assimilation: Comparison
1400 of diatoms and dinoflagellates at several growth temperatures, *Mar. Biol.*, 133, 541–551,
1401 <https://doi.org/10.1007/s002270050494>, 1999.

1402 Lourey, M. J., Trull, T. W., and Sigman, D. M.: Sensitivity of δ¹⁵N of nitrate, surface suspended and deep
1403 sinking particulate nitrogen to seasonal nitrate depletion in the Southern Ocean, *Global Biogeochem. Cycles*, 17,
1404 1–18, <https://doi.org/10.1029/2002gb001973>, 2003.

1405 Martin, J. H., Gordon, R. M., and Fitzwater, S. E.: Iron Limitation, *Limnol. Oceanogr.*, 36, 1793–1802, 1991.

1406 Martínez-García, A., Sigman, D. M., Ren, H., Anderson, R. F., Straub, M., Hodell, D. A., Jaccard, S. L.,
1407 Eglinton, T. I., and Haug, G. H.: Iron Fertilization of the Subantarctic Ocean During the Last Ice Age, 2014.

1408 Martiny, A. C., Pham, C. T. A., Primeau, F. W., Vrugt, J. A., Moore, J. K., Levin, S. A., and Lomas, M. W.:
1409 Strong latitudinal patterns in the elemental ratios of marine plankton and organic matter, *Nat. Geosci.*,

1410 <https://doi.org/10.1038/NGEO1757>, 2013.

1411 Mathot, S., Smith, W. O., Carlson, C. A., Garrison, D. L., Gowing, M. M., and Vickers, C. L.: Carbon
1412 partitioning within phaeocystis antarctica (prymnesiophyceae) colonies in the ross sea, antarctica, *J. Phycol.*, 36,
1413 1049–1056, <https://doi.org/10.1046/j.1529-8817.2000.99078.x>, 2000.

1414 McIlvin, M. R. and Casciotti, K. L.: Technical updates to the bacterial method for nitrate isotopic analyses,
1415 *Anal. Chem.*, 83, 1850–1856, <https://doi.org/10.1021/ac1028984>, 2011.

1416 Mduyana, M., Thomalla, S. J., Philibert, R., Ward, B. B., and Fawcett, S. E.: The Seasonal Cycle of Nitrogen
1417 Uptake and Nitrification in the Atlantic Sector of the Southern Ocean, *Global Biogeochem. Cycles*, 34, 1–29,
1418 <https://doi.org/10.1029/2019GB006363>, 2020.

1419 Moisan, T. A. and Mitchell, B. G.: Photophysiological acclimation of *Phaeocystis antarctica* Karsten under light
1420 limitation, *Limnol. Oceanogr.*, 44, 247–258, <https://doi.org/10.4319/LO.1999.44.2.0247>, 1999.

1421 Mosseri, J., Quéguiner, B., Armand, L., and Cornet-Barthaux, V.: Impact of iron on silicon utilization by
1422 diatoms in the Southern Ocean: A case study of Si/N cycle decoupling in a naturally iron-enriched area, *Deep.
1423 Res. Part II Top. Stud. Oceanogr.*, 55, 801–819, <https://doi.org/10.1016/j.dsr2.2007.12.003>, 2008.

1424 Muench, R. D. and Gordon, A. L.: Circulation and transport of water along the western Weddell Sea margin, *J.
1425 Geophys. Res.*, 100, 18503–18515, <https://doi.org/10.1029/95jc00965>, 1995.

1426 Nelson, M., Smith, O., Gordon, I., and Huber, A.: nutrient, 92, 7181–7190, 1987.

1427 Nicholls, K. W., Pudsey, C. J., and Morris, P.: Summertime water masses off the northern Larsen C Ice Shelf,
1428 *Antarctica, Geophys. Res. Lett.*, 31, 2–5, <https://doi.org/10.1029/2004GL019924>, 2004.

1429 Nicholls, K. W., Østerhus, S., Makinson, K., Gammelsrød, T., and Fahrbach, E.: Ice-ocean processes over the
1430 continental shelf of the Southern Weddell Sea, *Antarctica: A review, Rev. Geophys.*, 47, 1–23,
1431 <https://doi.org/10.1029/2007RG000250>, 2009.

1432 Nissen, C. and Vogt, M.: Factors controlling the competition between *Phaeocystis* and diatoms in the Southern
1433 Ocean in the Southern Ocean, *Biogeosciences Discuss.*, 1–39, <https://doi.org/10.5194/bg-2019-488>, 2021.

1434 Olson, R. J.: Differential photoinhibition of marine nitrifying bacteria: a possible mechanism for the formation
1435 of the primary nitrite maximum, *J. Mar. Res.*, 39, 227–238, 1981.

1436 Orsi, A. H., Nowlin, W. D., and Whitworth, T.: On the circulation and stratification of the Weddell Gyre, *Deep.
1437 Res. Part I*, 40, 169–203, [https://doi.org/10.1016/0967-0637\(93\)90060-G](https://doi.org/10.1016/0967-0637(93)90060-G), 1993.

1438 Orsi, A. H., Whitworth, T., and Nowlin, W. D.: On the meridional extent and fronts of the Antarctic
1439 Circumpolar Current, *Deep. Res. Part I*, 42, 641–673, [https://doi.org/10.1016/0967-0637\(95\)00021-W](https://doi.org/10.1016/0967-0637(95)00021-W), 1995.

1440 Park, M. G., Yang, S. R., Kang, S.-H., Chung, K. H., and Shim, J. H.: Phytoplankton biomass and primary
1441 production in the marginal ice zone of the northwestern Weddell Sea during austral summer, *Polar Biol.* 1999
1442 214, 21, 251–261, <https://doi.org/10.1007/S003000050360>, 1999.

1443 Parsons, T. R., Maita, Y., and Lalli, C. M.: A manual of chemical and biological methods for seawater analysis,
1444 1984.

1445 Paulsen, M. L., Riisgaard, K., Thingstad, T. F., John, M. S., and Nielsen, T. G.: Winter-spring transition in the
1446 subarctic Atlantic: Microbial response to deep mixing and pre-bloom production., *Aquat. Microb. Ecol.*, 76, 49–
1447 49, 2015.

1448 Peng, X., Fuchsman, C. A., Jayakumar, A., Oleynik, S., Martens-Habbena, W., Devol, A. H., and Ward, B. B.:
1449 Ammonia and nitrite oxidation in the eastern tropical North Pacific, *Glob. Biogeochem. Cycles* 29, 2034–

1450 2049, 2015.

1451 Petrou, K., Kranz, S. A., Trimborn, S., Hassler, C. S., Ameijeiras, S. B., Sackett, O., Ralph, P. J., and Davidson,
1452 A. T.: Southern Ocean phytoplankton physiology in a changing climate, *J. Plant Physiol.*, 203, 135–150,
1453 <https://doi.org/10.1016/j.jplph.2016.05.004>, 2016.

1454 Philibert, R., Waldron, H., and Clark, D.: A geographical and seasonal comparison of nitrogen uptake by
1455 phytoplankton in the Southern Ocean, *Ocean Sci.*, 11, 251–267, <https://doi.org/10.5194/OS-11-251-2015>, 2015.

1456 Pineda-Metz, S. E. A., Isla, E., and Gerdes, D.: Benthic communities of the Filchner Region (Weddell Sea,
1457 Antarctica), *Mar. Ecol. Prog. Ser.*, 628, 37–54, <https://doi.org/10.3354/MEPS13093>, 2019.

1458 Pörtner, H. O., Karl, D. M., Boyd, P. W., Cheung, W. W., Lluch-Cota, S. E., Nojiri, Y., and Et, A.: Ocean
1459 systems, in: *Impacts, Adaptation, and Vulnerability. Part A: Global and Sectoral Aspects. Contribution of*
1460 *Working Group II to the Fifth Assessment Report of the Intergovernmental Panel on Climate Change*, edited by:
1461 Field, C. B. and Et, A., Cambridge University Press, 411–484, 2014.

1462 Priddle, J., Boyd, I. L., Whitehouse, M. J., Murphy, E. J., and Croxall, J. P.: Estimates of Southern Ocean
1463 primary production - Constraints from predator carbon demand and nutrient drawdown, in: *Journal of Marine*
1464 *Systems*, 275–288, [https://doi.org/10.1016/S0924-7963\(98\)00043-8](https://doi.org/10.1016/S0924-7963(98)00043-8), 1998.

1465 Probyn, T. A. and Painting, S. J.: Nitrogen uptake by size-fractionated phytoplankton populations in Antarctic
1466 surface waters I, *Limnol. Oceanogr.*, 30, 1327–1332, <https://doi.org/10.4319/LO.1985.30.6.1327>, 1985.

1467 Ragueneau, O., Tréguer, P., Leynaert, A., Anderson, R. F., Brzezinski, M. A., DeMaster, D. J., Dugdale, R. C.,
1468 Dymond, J., Fischer, G., François, R., Heinze, C., Maier-Reimer, E., Martin-Jézéquel, V., Nelson, D. M., and
1469 Quéguiner, B.: A review of the Si cycle in the modern ocean: Recent progress and missing gaps in the
1470 application of biogenic opal as a paleoproductivity proxy, *Glob. Planet. Change*, 26, 317–365,
1471 [https://doi.org/10.1016/S0921-8181\(00\)00052-7](https://doi.org/10.1016/S0921-8181(00)00052-7), 2000.

1472 Revilla, M., Alexander, J., and Glibert, P. M.: Urea analysis in coastal waters: Comparison of enzymatic and
1473 direct methods, *Limnol. Oceanogr. Methods*, 3, 290–299, <https://doi.org/10.4319/lom.2005.3.290>, 2005.

1474 Rönner, U., Sörensson, F., and Holm-Hansen, O.: Nitrogen assimilation by phytoplankton in the Scotia Sea,
1475 *Polar Biol.*, 2, 137–147, <https://doi.org/10.1007/BF00448963>, 1983.

1476 Sallée, J. B., Shuckburgh, E., Bruneau, N., Meijers, A. J., Bracegirdle, T. J., and Wang, Z.: Assessment of
1477 Southern Ocean mixed-layer depths in CMIP5 models: Historical bias and forcing response, *J. Geophys. Res.*
1478 *Ocean.*, 118, 1845–1862, 2013.

1479 Santoro, A. E., Sakamoto, C. M., Smith, J. M., Plant, J. N., Gehman, A. L., Worden, A. Z., Johnson, K. S.,
1480 Francis, C. A., and Casciotti, K. L.: Measurements of nitrite production in and around the primary nitrite
1481 maximum in the central California Current, 10, 7395–7410, <https://doi.org/10.5194/bg-10-7395-2013>, 2013.

1482 Sarmiento, J., Toggweiler, J.: A new model for the role of the oceans in determining atmospheric P CO₂,
1483 *Nature*, 308, 621–624, <https://doi.org/https://doi.org/10.1038/308621a0>, 1984.

1484 Sarmiento, J. L., Gruber, N., Brzezinski, M. A., and Dunne, J. P.: High-latitude controls of thermocline nutrients
1485 and low latitude biological productivity, *Nature*, 427, 56–60, <https://doi.org/10.1038/nature10605>, 2004.

1486 Saxberg, B. E. H. and Kowalski, B. R.: Generalized Standard Addition Method, *Anal. Chem.*, 51, 1031–1038,
1487 <https://doi.org/10.1021/ac50043a059>, 1979.

1488 Scharek, R., Smetacek, V., Fahrback, E., Gordon, L. I., Rohardt, G., and Moore, S.: The transition from winter
1489 to early spring in the eastern Weddell Sea, Antarctica: Plankton biomass and composition in relation to

1490 hydrography and nutrients, *Deep. Res. Part I*, 41, 1231–1250, [https://doi.org/10.1016/0967-0637\(94\)90042-6](https://doi.org/10.1016/0967-0637(94)90042-6),
1491 1994.

1492 Schodlok, M. P., Hellmer, H. H., & Beckmann, A.: On the transport, variability and origin of dense water masses
1493 crossing the South Scotia Ridge. *Deep Sea Res. II Trop. Stud. Oceanogr.*, 49, 4807–4825, 2002.

1494 Schoemann, V., Becquevort, S., Stefels, J., Rousseau, V., and Lancelot, C.: Phaeocystis blooms in the global
1495 ocean and their controlling mechanisms: A review, *J. Sea Res.*, 53, 43–66,
1496 <https://doi.org/10.1016/j.seares.2004.01.008>, 2005.

1497 Schofield, O., Miles, T., Alderkamp, A. C., Lee, S. H., Haskins, C., Rogalsky, E., Sipler, R., Sherrell, R. M., and
1498 Yager, P. L.: In situ phytoplankton distributions in the Amundsen Sea Polynya measured by autonomous
1499 gliders, 3, 1–17, <https://doi.org/10.12952/journal.elementa.000073>, 2015.

1500 Schröder, M., Hellmer, H. H., and Absy, J. M.: On the near-bottom variability in the northwestern Weddell Sea,
1501 *Deep. Res. Part II Top. Stud. Oceanogr.*, 49, 4767–4790, [https://doi.org/10.1016/S0967-0645\(02\)00158-3](https://doi.org/10.1016/S0967-0645(02)00158-3), 2002.

1502 Sedwick, P. N., Di Tullio, G. R., and Mackey, D. J.: Iron and manganese in the Ross Sea, Seasonal iron
1503 limitation in Antarctic, *J. Geophys. Res. Ocean.*, 105, 11321–11336, <https://doi.org/10.1029/2000JC000256>,
1504 2000.

1505 Semeneh, M., Dehairs, F., Elskens, M., Baumann, M. E. M., Kopczynska, E. E., Lancelot, C., and Goeyens, L.:
1506 Nitrogen uptake regime and phytoplankton community structure in the Atlantic and Indian sectors of the
1507 Southern Ocean, *J. Mar. Syst.*, 17, 159–177, [https://doi.org/10.1016/S0924-7963\(98\)00036-0](https://doi.org/10.1016/S0924-7963(98)00036-0), 1998.

1508 SI, R., T, T., DW, C., and JG, G.: Primary productivity and nutrient utilization ratios in the Pacific sector of the
1509 Southern Ocean based on seasonal changes in seawater chemistry, *Deep Sea Res. Part I Oceanogr. Res. Pap.*,
1510 45, 1211–1234, 1998.

1511 Sigman, D. M. and Boyle², E. A.: Glacial/interglacial variations in atmospheric carbon dioxide, *NATURE*,
1512 2000.

1513 Sigman, D. M., Casciotti, K. L., Andreani, M., Barford, C., Galanter, M., and Böhlke, J. K.: A bacterial method
1514 for the nitrogen isotopic analysis of nitrate in seawater and freshwater, *Anal. Chem.*, 73, 4145–4153,
1515 <https://doi.org/10.1021/ac010088e>, 2001.

1516 Sigman, D. M., Hain, M. P., and Haug, G. H.: The polar ocean and glacial cycles in atmospheric CO₂
1517 concentration, *Nature*, 466, <https://doi.org/10.1038/nature09149>, 2010.

1518 Smart, S. M., Fawcett, S. E., Ren, H., Schiebel, R., Tompkins, E. M., Martínez-García, A., Stimmann, L.,
1519 Roychoudhury, A., Haug, G. H., and Sigman, D. M.: The Nitrogen Isotopic Composition of Tissue and Shell-
1520 Bound Organic Matter of Planktic Foraminifera in Southern Ocean Surface Waters, *Geochemistry, Geophys.*
1521 *Geosystems*, 21, 1–29, <https://doi.org/10.1029/2019GC008440>, 2020.

1522 Smetacek, V.: The giant diatom dump, *Nat.* 2000 4066796, 406, 574–575, <https://doi.org/10.1038/35020665>,
1523 2000.

1524 Smetacek, V., Assmy, P., and Henjes, J.: The role of grazing in structuring Southern Ocean pelagic ecosystems
1525 and biogeochemical cycles, *Antarct. Sci.*, 16, 541–558, <https://doi.org/10.1017/S0954102004002317>, 2004.

1526 Smith, J. M., Chavez, F. P., and Francis, C. A.: Ammonium Uptake by Phytoplankton Regulates Nitrification in
1527 the Sunlit Ocean, *PLoS One*, 9, 108173, <https://doi.org/10.1371/journal.pone.0108173>, 2014.

1528 Smith, W. O. and Nelson, D. M.: Phytoplankton growth and new production in the Weddell Sea marginal ice
1529 zone in the austral spring and autumn, *Limnol. Oceanogr.*, 35, 809–821,

1530 <https://doi.org/10.4319/lo.1990.35.4.0809>, 1990.

1531 Smith, W. O. and Asper, V. L.: The influence of phytoplankton assemblage composition on biogeochemical
1532 characteristics and cycles in the southern Ross Sea, Antarctica, *Deep. Res. Part I Oceanogr. Res. Pap.*, 48, 137–
1533 161, [https://doi.org/10.1016/S0967-0637\(00\)00045-5](https://doi.org/10.1016/S0967-0637(00)00045-5), 2001.

1534 Spiridonov, V. A., Nöthig, E. M., Schröder, M., and Wisotzki, A.: The onset of biological winter in the eastern
1535 Weddell Gyre (Antarctica) planktonic community, *J. Mar. Syst.*, 9, 211–230, [https://doi.org/10.1016/S0924-7963\(95\)00049-6](https://doi.org/10.1016/S0924-7963(95)00049-6), 1996.

1537 Stammerjohn, S., Massom, R., Rind, D., and Martinson, D.: Regions of rapid sea ice change: An inter-
1538 hemispheric seasonal comparison, *Geophys. Res. Lett.*, 39, L06501, 2012.

1539 Stefels, J. and Van Leeuwe, M. A.: Effects of iron and light stress on the biochemical composition of antarctic
1540 *Phaeocystis* sp. (Prymnesiophyceae). I. Intracellular DMSP concentrations, *J. Phycol.*, 34, 486–495,
1541 <https://doi.org/10.1046/j.1529-8817.1998.340486.x>, 1998.

1542 Strickland, J. D. H. and Parsons, T. R.: A practical handbook of seawater analysis, *Bull. Fish. Res. Board*
1543 *Canada*, 167, 81–86, 1968.

1544 Strzepek, R. F., Maldonado, M. T., Hunter, K. A., Frew, R. D., and Boyd, P. W.: Adaptive strategies by
1545 Southern Ocean phytoplankton to lessen iron limitation: Uptake of organically complexed iron and reduced
1546 cellular iron requirements, *Limnol. Oceanogr.*, 56, 1983–2002, <https://doi.org/10.4319/lo.2011.56.6.1983>, 2011.

1547 Sunda, W. G. and Huntsman, S. A.: Interrelated influence of iron, light and cell size on marine phytoplankton
1548 growth, *Nature*, 390, 389–392, <https://doi.org/10.1038/37093>, 1997.

1549 Sunda, W. G. and Huntsman, S. A.: High iron requirement for growth, photosynthesis, and low-light
1550 acclimation in the coastal cyanobacterium *Synechococcus bacillaris*, *Front. Microbiol.*, 6, 561, 2015.

1551 Takeda, S.: Influence of iron availability on nutrient consumption ratio, *Nature*, 393, 774–777, 1998.

1552 Talley, L. D., Pickard, G. L., Emery, W. J., and Swift, J. H.: Southern Ocean, *Descr. Phys. Oceanogr.*, 437–471,
1553 <https://doi.org/10.1016/b978-0-7506-4552-2.10013-7>, 2011.

1554 Taylor, B. W., Keep, C. F., Hall, R. O., Koch, B. J., Tronstad, L. M., Flecker, A. S., and Ulseth, A. J.:
1555 Improving the fluorometric ammonium method: matrix effects, background fluorescence, and standard
1556 additions, *J. North Am. Benthol. Soc.*, 26, 167–177, [https://doi.org/10.1899/0887-3593\(2007\)26\[167:ITFAMM\]2.0.CO;2](https://doi.org/10.1899/0887-3593(2007)26[167:ITFAMM]2.0.CO;2), 2007.

1558 Treguer, P. and G, J.: Review Dynamics of nutrients and phytoplankton, and fluxes of carbon, nitrogen and
1559 silicon in the Antarctic Ocean, edited by: Hempel, G., Springer Berlin Heidelberg, 1992.

1560 Tréguer, P., Bowler, C., Moriceau, B., Dutkiewicz, S., Gehlen, M., Aumont, O., Bittner, L., Dugdale, R., Finkel,
1561 Z., Iudicone, D., Jahn, O., Guidi, L., Lasbleiz, M., Leblanc, K., Levy, M., and Pondaven, P.: Influence of diatom
1562 diversity on the ocean biological carbon pump, *Nat. Geosci.*, <https://doi.org/10.1038/s41561-017-0028-x>, 2017.

1563 Vernet, M., Geibert, W., Hoppema, M., Brown, P. J., Haas, C., Hellmer, H. H., Jokat, W., Jullion, L., Mazloff,
1564 M., Bakker, D. C. E., Brearley, J. A., Croot, P., Hattermann, T., Hauck, J., Hillenbrand, C. D., Hoppe, C. J. M.,
1565 Huhn, O., Koch, B. P., Lechtenfeld, O. J., Meredith, M. P., Naveira Garabato, A. C., Nöthig, E. M., Peeken, I.,
1566 Rutgers van der Loeff, M. M., Schmidtke, S., Schröder, M., Strass, V. H., Torres-Valdés, S., and Verdy, A.: The
1567 Weddell Gyre, Southern Ocean: Present Knowledge and Future Challenges, *Rev. Geophys.*, 57, 623–708,
1568 <https://doi.org/10.1029/2018RG000604>, 2019.

1569 Vogt, M., O'Brien, C., Peloquin, J., Schoemann, V., Breton, E., Estrada, M., Gibson, J., Karentz, D., Van

1570 Leeuwe, M. A., Stefels, J., Widdicombe, C., and Peperzak, L.: Global marine plankton functional type biomass
1571 distributions: *Phaeocystis* spp., Earth Syst. Sci. Data, 4, 107–120,
1572 <https://doi.org/10.5194/essd-4-107-2012>, 2012.

1573 Volk, T. and Hoffert, M. I.: Ocean Carbon Pumps: Analysis of Relative Strengths and Efficiencies in Ocean-
1574 Driven Atmospheric CO₂ Changes, in: Geophysical Monograph Series, edited by: Sundquist, E. T. and
1575 Broecker, W. S., 1985.

1576 Ward, B. B.: Light and substrate concentration relationships with marine ammonium assimilation and oxidation
1577 rates, Mar. Chem., 16, 301–316, [https://doi.org/10.1016/0304-4203\(85\)90052-0](https://doi.org/10.1016/0304-4203(85)90052-0), 1985.

1578 Ward, B. B.: Temporal variability in nitrification rates and related biogeochemical factors in Monterey Bay,
1579 California, USA, Mar. Ecol. Prog. Ser., 292, 97–109, <https://doi.org/10.3354/meps292097>, 2005.

1580 Weber, T. S. and Deutsch, C.: Ocean nutrient ratios governed by plankton biogeography,
1581 <https://doi.org/10.1038/nature09403>, 2010a.

1582 Weber, T. S. and Deutsch, C.: Ocean nutrient ratios governed by plankton biogeography, Nature, 467, 550–554,
1583 <https://doi.org/10.1038/nature09403>, 2010b.

1584 Whitworth, T. and Nowlin, W. D.: Water Masses and Currents of the Southern Ocean at the Greenwich
1585 Meridian, JOURNAL OF GEOPHYSICAL RESEARCH, 6462–6476 pp.,
1586 <https://doi.org/10.1029/JC092iC06p06462>, 1987.

1587 Yool, A., Martin, A. P., Fernández, C., and Clark, D. R.: The significance of nitrification for oceanic new
1588 production, <https://doi.org/10.1038/nature05885>, n.d.

1589 Zakem, E. J., Al-Haj, A., Church, M. J., Van Dijken, G. L., Dutkiewicz, S., Foster, S. Q., Fulweiler, R. W.,
1590 Mills, M. M., and Follows, M. J.: Ecological control of nitrite in the upper ocean, Nat. Commun., 9,
1591 <https://doi.org/10.1038/s41467-018-03553-w>, 2018.

1592

1593